INVESTIGATION OF PHOTOLUMINESCENT PROPERTIES OF RARE-EARTHS DOPED MIXED MULTICOMPONENT STRUCTURES OF PHOSPHOVANADATES

By

Motloung Selepe Joel

(MSc)

A thesis submitted in partial fulfilment of the requirements for the degree

Doctor of Philosophy (Ph.D.)

in the

Faculty of Natural and Agricultural Sciences

Department of Physics

at the

University of the Free State

Promoter: Prof. O.M. Ntwaeaborwa

Co-Promoter: Dr. K.G Tshabalala

2017

Dedication

Dedicated to my Mom and Dad, the late

Selepe Sondie Elsie (1953–2004)

and

Motloung Joseph (1953–2013)

Declaration

I, the undersigned, hereby declare that the work contained in this thesis is my own original work except as indicated in the references. It has not been submitted before for any degree or examination in this or any other university.

Motloung Selepe Joel

Signed at _____

On the _____ day of _____ 2017

Acknowledgements

"*The fear of the **LORD** is the beginning of knowledge*"

I thank ***GOD***, the ***ALMIGHTY***; all my efforts would have been nothing without ***HIM***.

To the "*shadow*" the "*chest*", thank you very much for your mercy and guidance

To my mother and father, the late, *SE Selepe* and *J Motloung*, THANK YOU. To my brothers *Joina*, *Ben*, *Tys*, *Piet* and *Thomas* and my sisters, *Makulane* and the late *Ouma*, "*ke a leboha*".

I would like to thank my supervisor, Professor Martin O Ntwaeaborwa. Prof, I have no words, I really don't know what to say. But, "*thank you*", for your encouragement, motivation, patience, constant guidance and unlimited advice you provided throughout my **YEARS** as your student. I am so humbled and feel so blessed to have a supervisor who cares so much, who responded to my questions and queries so promptly.

To Dr. George K Tshabalala "*KayGee*", you provided much needed support both as my co-supervisor and "*BOSO*". You were always there for constructive discussions and willing to proof read and correcting countless pages, for that I thank you. I have been extremely fortunate to have you as my line manager and my co-supervisor.

I am very grateful to Prof. HC Swart for letting me work on most of his characterization techniques. I wouldn't have made it if it wasn't for his tolerance. I would like to thank Prof. RE Kroon for his endless support. I also want to extend my thanks to Dr. SKK Shaat for introducing me to this project.

Thank you "Puse" for helping me with SEM measurements, "Pulane" for helping me with DRS measurements, "S'bu" with XRD measurements. I don't know how many times I slept far from home, Ms. Lebeko, thank you for organizing transport, accommodation and food for me.

I would like to thank ***all*** my colleagues, postgraduate students and postdoctoral fellows (*Drs. Fekadu, Aheman, Nehume*) in the department (*Physics*) for their support as well as fruitful discussions and assistance about my research and my career.

Thank you to the *South African National Research Foundation* (NRF) THUTHUKA program and the *University of the Free State* (UFS) for the financial support.

Lastly, I want to direct my deepest gratitude to my *precious children,* **Motloung Maserame** and **Motloung Lebohang**, and especially to my *lovely wife,* **Motloung M Gladys**, for their constant encouragement and total support in my attainment of this goal.

ABSTRACT

INVESTIGATION OF PHOTOLUMINESCENT PROPERTIES OF RARE-EARTHS DOPED MIXED MULTICOMPONENT STRUCTURES OF PHOSPHOVANADATES

Motloung Selepe Joel

PhD Thesis, Department of Physics, University of the Free State

Multicomponent structures of lanthanide phosphovanadate doped with various rare earth ions were successfully synthesized by solution combustion method. These phosphor powders were prepared at 600±10^{o}C using urea as a fuel. Selected series of samples were annealed at different temperatures ranging from (700 –1000^{o}C) while others were annealed at 900^{o}C for 2 hours, which was found to be the optimum temperature.

The crystal structure formation, crystallite sizes, and surface morphologies of the prepared phosphor powders were identified by X-ray diffraction (XRD), high resolution transmission electron microscope (HR–TEM) and field emission scanning electron microscopy (FE–SEM). The elemental composition and the stretching modes of vibration of the samples were investigated by energy dispersive x-ray spectroscopy (EDS) and Fourier transform infrared (FTIR) spectrometer respectively. The diffuse reflectance measurements, which were used to estimate the band gap energies, were determined by ultraviolet/visible spectroscopy (UV–vis). The room temperature photoluminescence (PL) data, excitation and emission, were recorded using a HITACHI F700 fluorescence spectrophotometer.

The XRD results revealed that $GdVO_4$ and $GdPO_4$ crystallized in a tetragonal structures. The results further indicated that the XRD peaks of $GdV_{1-x}P_xO_4$ slightly shifted towards higher

values of 2θ angles when the value of *x* (P content) was increased. The X-ray diffraction peaks of $GdV_{0.5}P_{0.5}O_4$ were found to be a combination of those of bulk $GdVO_4$ and $GdPO_4$. On the other hand, the lanthanum systems, $LaV_{1-x}P_xO_4$ (x = 0, 0.25, 0.5, 0.75, 1), the XRD results confirmed the formation of monoclinic structure of $LaVO_4$ for x = 0 and hexagonal structure of $LaPO_4$ for x = 1. The results also revealed that the crystal structure changed from $LaVO_4$ to $LaPO_4$ when the value of x was increased from 0 to 1. The XRD results for the yttrium system, $YV_{0.5}P_{0.5}O_4$ in particular, showed that the peaks were a combination of those of bulk YVO_4 and YPO_4. In general, the XRD results showed that all the annealed samples were highly crystalline, free of impurities and have small crystallite sizes. Thus, the annealing temperature played a pivotal role to improve the crystallinity of the prepared powder samples. This was confirmed by the pronouncement of the distinct lattice fringes on the HR–TEM images.

FE-SEM results revealed that the particles of the prepared powder samples are agglomerated for un-annealed samples and less agglomerated for the annealed samples. Generally, the FE-SEM micrographs showed that the samples have different shapes and sizes. The incorporation of the dopants did not cause any noticeable change on the morphology of the prepared samples. The presence of all these dopants within the host materials were confirmed by EDS.

The room temperature diffuse reflectance spectra revealed that the prepared powder samples mainly absorbed in the UV region. The DRS were mostly dominated by the absorption band in the range between 200 and 350 nm peaking at ~ 275 nm. In some instances, some weak f→f bands were also observed beyond 350 nm. The band gap energies were found to be influenced by the phosphorus content within the samples as well as the dopant concentrations.

The room temperature PL data revealed that the prepared powder samples could be excited with UV radiation and emit in the visible range. The strong broad band in the UV range between

200 and 350 nm was observed in almost all the samples, although there were minor f→f bands beyond 350 nm wavelength for other samples. PL data also revealed that there was energy transfer from the host to the dopants and between the dopants for doubly doped samples. Generally, the PL intensity was influenced by the vanadium and phosphorus concentrations, the annealing temperature and the dopant concentrations.

Keywords

Multicomponent structures, terbium, samarium, thulium, X-ray diffraction, phosphovanadate, rare earths, energy transfer, quenching of luminescence, combustion synthesis.

Acronyms

CE	Counter electrode
DRS	Diffuse reflectance spectra
DSSC	Dye sensitized solar cells
EDS	Energy dispersive X-ray spectroscopy
FESEM	Field emission scanning electron microscopy
FTIR	Fourier transform infrared
HREE	Heavy group rare earth elements
HRTEM	High resolution transmission electron microscopy
HTS	High temperature synthesis
IR	Infrared
LREE	Light group rare earth elements
PL	Photoluminescence
RE	Rare earth
SC	Solution combustion
UV	Ultraviolet
UV-VIS	Ultraviolet-visible
VUV	Vacuum ultraviolet
XRD	X-ray diffraction

List of figures

Figure 2.1. *Periodic table of the elements showing the division between LREEs and HREEs* [12]

Figure 2.2. *Crystal structure of (a) $GdVO_4$ and (b) $GdPO_4$* [16]

Figure 2.3. *Crystal structure of (a) $LaVO_4$ and (b) $LaPO_4$* [17]

Figure 2.4. *Crystal structure of (a) YPO_4 and (b) YVO_4* [18]

Figure 3.1 *Schematic representation of XRD operation* [25]

Figure 3.2 *Schematic diagram of electron diffraction in the TEM* [27]

Figure 3.3 *Schematic drawing showing the electron column, the deflection system and the electron detectors* [29]

Figure 3.4. *Fundamental components of an FTIR spectrometer* [31]

Figure 3.5. *A schematic diagram showing (a) specular and (b) diffuse reflection* [32]

Figure 3.6. *Schematic diagram of integrating sphere* [32]

Figure 3.7 *Schematic diagram of UV spectroscopy* [33]

Figure 3.8 *Schematic diagram of the optical system of the F-7000 fluorescence spectrophotometer* [35]

Figure 4.1. *Schematic representation of (a) $GdVO_4$ zircon-type (b) $GdPO_4$ monazite -type crystal structure* [42]

Figure 4.2. *XRD patterns of pure $GdVO_4$ and $GdPO_4.H_2O$ and (b) $GdV_{1-x}P_xO_4$: 1 mol % Tb^{3+} with x=0, 0.25, 0.5, 0.75 and 1.0* [45]

Figure 4.3 *(a) SEM image (b) size distribution histogram of the $GdV_{0.5}P_{0.5}O_4$: 1 mol % Tb^{3+}* [46]

Figure 4.4 *EDS spectrum of the as prepared $GdV_{0.5}P_{0.5}O_4$: 1 mol % Tb^{3+} powder phosphors* [47]

Figure 4.5 *FT-IR spectrum of the as prepared $GdV_{0.5}P_{0.5}O_4$: 1 mol % Tb^{3+} powder phosphors* [48]

Figure 4.6. *(a) The diffuse reflectance spectra (b) Transformed Kubelka-Munk reflectance of $GdV_{1-x}P_xO_4$: Tb^{3+} with x=0.25, 0.5, 0.75 powder phosphors* [49]

Figure 4.7 *(a). Excitation spectra of $GdV_{1-x}P_xO_4$: 1mol % Tb^{3+} powder phosphors with x=0, 0.25, 0.5, 0.75 and 1.0* [51]

Figure 4.7*(b). Emission spectra of $GdV_{1-x}P_xO_4$: 1mol % Tb^{3+} powder phosphors with x=0, 0.25, 0.5, 0.75 and 1.0. The PL emission spectrum with x = 1 is excluded in the inset.* [52]

Figure 4.8. *The intensities of the green emission ($^5D_4 \rightarrow {}^7F_5$) of $GdV_{1-x}P_xO_4$:1mol %Tb^{3+} as a function of x values* [53]

Figure 4.9. *(a) Schematic representation of energy level diagram and proposed energy transfer mechanism (b) Schematic representation of Tb^{3+} energy level diagram and proposed mechanism* [54]

Figure 4.10 *Decay curves of $GdV_{1-x}P_xO_4$:1mol %Tb^{3+} (x = 0, 0.25, 0.5, 0.75 and 1) powder phosphors* [56]

Figure 5.1. *XRD patterns of $GdV_{0.5}P_{0.5}O_4$: 3 mol % Sm^{3+}, 2.5 mol % Tm^{3+}* [64]

Figure 5.2. *SEM images of (a) $GdV_{0.5}P_{0.5}O_4$: Sm^{3+} (b) $GdV_{0.5}P_{0.5}O_4$: Tm^{3+} (c) $GdV_{0.5}P_{0.5}O_4$: Sm^{3+}, Tm^{3+} and (d) EDS spectrum of 3 mol % Sm^{3+}, 2.5 mol % Tm^{3+}* [65]

Figure 5.3. *(a) UV-Vis reflectance spectra and (b) transformed Kubelka-Munk plot of $GdV_{0.5}P_{0.5}O_4$: Sm^{3+}, Tm^{3+}* [66]

Figure 5.4. *(a) Excitation spectra of $GdV_{0.5}P_{0.5}O_4$: x mol % Tm^{3+}* [68]

Figure 5.4. *(b) Emission spectra of $GdV_{0.5}P_{0.5}O_4$: x mol % Tm^{3+}* [68]

Figure 5.5. *(a) Excitation and (b) Emission spectra of $GdV_{0.5}P_{0.5}O_4$: x mol % Sm^{3+}* [69]

Figure 5.6. *(a) Excitation and (b) Emission spectra of $GdV_{0.5}P_{0.5}O_4$: x mol % Sm^{3+}, Tm^{3+}* [70]

Figure 5.6. *(c) a plot showing the intensity as a function Tm^{3+} concentration* [71]

Figure 6.1. *(a) XRD patterns of $YV_{0.5}P_{0.5}O_4$ host, singly doped $YV_{0.5}P_{0.5}O_4$: 1 mol% Sm^{3+}/ 1 mol% Tm^{3+} and co-doped 1 mol% Sm^{3+}; 0.5 mol % Tm^{3+}* [78]

Figure 6.1. *(b) A plot of $\beta \cos \theta$ against Sin θ of $YV_{0.5}P_{0.5}O_4$ (host).* [79]

Figure 6.2. *(a) Unannealed (b) and (c) annealed: SEM micrographs of $YV_{0.5}P_{0.5}O_4$: 3 mol % Sm^{3+}, 2.5 mol % Tm^{3+}. Low (d) and high (e) magnification TEM images of $YV_{0.5}P_{0.5}O_4$: 3 mol % Sm^{3+}, 0.25 mol % Tm^{3+}. EDS spectra of $YV_{0.5}P_{0.5}O_4$: 3 mol % Sm^{3+}, 2.5 mol % Tm^{3+} (f) annealed (g) annealed.* [81]

Figure 6.3. *UV-Vis reflectance spectra of (a) $YV_{0.5}P_{0.5}O_4$: x mol % Sm^{3+}, (b) x mol % Tm^{3+}, (c) 3 mol %Sm^{3+}; x mol % Tm^{3+} and (e) 1 mol % Tm^{3+}; x mol % Sm^{3+}. (d) Transformed Kubelka-Munk reflectance spectrum of 3 mol % Sm^{3+}; x mol % Tm^{3+}, and (f) 1 mol % Tm^{3+}; x mol % Sm^{3+}* [82]

Figure 6.4. *(a) Excitation and (b) Emission spectra of $YV_{0.5}P_{0.5}O_4$: x mol % Tm^{3+} and (c) a plot showing the intensity as a function Tm^{3+} concentration* [84]

Figure 6.5. *(a) Excitation and (b) Emission spectra of $YV_{0.5}P_{0.5}O_4$: x mol % Sm^{3+} (c) a plot showing the intensity as a function Sm^{3+} concentration* [86]

Figure 6.6. *(a) Excitation and (b) Emission spectra of $V_{0.5}P_{0.5}O_4$: 3 mol % Sm^{3+}, x mol % Tm^{3+} (c) Excitation and (d) Emission spectra of $YV_{0.5}P_{0.5}O_4$: 1 mol % Tm^{3+}, x mol % Sm^{3+} (e) a plot showing the intensity as a function Sm^{3+} and (f) Tm^{3+} concentration (g) Schematic representation energy level diagram and proposed mechanism* [88]

Figure 7.1. *XRD patterns of $LaV_{1-x}P_xO_4$ (x = 0.0, 0.25, 0.5, 0.75, and 1.0) phosphor powder* [95]

Figure 7.2. *SEM images of $LaV_{0.5}P_{0.5}O_4$ doped with (a) Dy^{3+}, (b) Sm^{3+} and (c) Tb^{3+} phosphor powder.* [96]

Figure 7.3. *TEM images of $LaV_{0.5}P_{0.5}O_4$ doped with (a) Dy^{3+}, (b) Sm^{3+} and (c) Tb^{3+} phosphor powder.* [97]

Figure 7.4. *(a) UV-Vis reflectance spectra and (b) transformed Kubelka-Munk plot of $LaV_{0.5}P_{0.5}O_4$: 1 mol % Ln^{3+} (Ln = Dy, Sm, Tb)* [98]

Figure 7.5. *(a) Excitation and (b) Emission spectra of $LaV_{1-x}P_xO_4$: Dy^{3+} (c) A plot showing the intensity as a function of x values* [100]

Figure 7.6. *(a) Excitation and (b) Emission spectra of $LaV_{1-x}P_xO_4$:Sm^{3+} (c) A plot showing the intensity as a function of x values* [101]

Figure 7.7. *(a) Excitation and (b) Emission spectra of $LaV_{1-x}P_xO_4$: Tb^{3+} (c) A plot showing the intensity as a function of x values* [102]

Figure 8.1. *XRD patterns of $LaV_{0.25}P_{0.75}O_4$: 1 mol % Tb^{3+} and JCPDS's of phosphor powder annealed at different temperatures* [109]

Figure 8.2. *SEM images and EDS spectra of (a) $LaV_{0.25}P_{0.75}O_4$: 1 mol % Dy^{3+}, (b) $LaV_{0.25}P_{0.75}O_4$: 1 mol % Tb^{3+} and (c) $LaV_{0.75}P_{0.25}O_4$: 1 mol % Sm^{3+}* [111]

Figure 8.3. *FTIR spectrum of $LaV_{0.25}P_{0.75}O_4$: 1 mol % Tb^{3+} phosphor powder* [112]

Figure 8.4. *(a) Excitation and (b) Emission spectra of $LaV_{0.25}P_{0.75}O_4$: 1 mol % Dy^{3+} (c) A plot showing the relative emission intensity as a function of annealing temperature* [113]

Figure 8.5. *(a) Excitation and (b) Emission spectra of $LaV_{0.25}P_{0.75}O_4$: 1 mol % Tb^{3+} (c) A plot showing the relative emission intensity as a function of annealing temperature* [114]

Figure 8.6. *(a) Excitation and (b) Emission spectra of $LaV_{0.75}P_{0.25}O_4$: 1 mol % Sm^{3+} (c) A plot showing the relative emission intensity as a function of annealing temperature* [115]

Figure 9.1. *XRD pattern of (a) $GdV_{0.5}P_{0.5}O_4$: Sm^{3+}, Tm^{3+} and JCPDS files of $GdVO_4$, (b) $LaV_{0.5}P_{0.5}O_4$: Sm^{3+}, Tm^{3+} and JCPDS file of $LaVO_4$ (c) $YV_{0.5}P_{0.5}O_4$: Sm^{3+}, Tm^{3+} powder and JCPDS file (d) a plot of $\beta \cos\theta$ against $\sin\theta$ of $GdV_{0.5}P_{0.5}O_4$: Sm^{3+}, Tm^{3+}* [123]

Figure 9.2. *SEM micrographs and size distribution histograms of (a and b) $GdV_{0.5}P_{0.5}O_4$: Sm^{3+}; Tm^{3+}, (c and d) $LaV_{0.5}P_{0.5}O_4$: Sm^{3+}; Tm^{3+} and (e and f) $YV_{0.5}P_{0.5}O_4$: Sm^{3+}; Tm^{3+}* [125]

Figure 9.3. *UV-Vis reflectance spectra of (a) and (b) Transformed Kubelka-Munk reflectance* $YV_{0.5}P_{0.5}O_4$*:* Sm^{3+}, Tm^{3+} .....[126]

Figure 9.4. *(a) Excitation and (b) Emission spectra of* $MV_{0.5}P_{0.5}O_4$*:* Sm^{3+}, Tm^{3+} *(M = Gd, La, Y)* .....[127]

Contents

DEDICATION ..... **II**

DECLARATION ..... **III**

ACKNOWLEDGEMENTS ..... **IV**

ABSTRACT ..... **V**

ACRONYMS ..... **VIII**

LIST OF FIGURES ..... **IX**

CHAPTER 1: INTRODUCTION **1**

1.1 OVERVIEW 1
1.2 PROBLEM STATEMENT 3
1.3 RESEARCH OBJECTIVES 4
1.4 THESIS LAYOUT 5
1.5 REFERENCES 6

CHAPTER 2 THEORETICAL OVERVIEW **8**

2.1 INTRODUCTION 8
2.2 PHOSPHORS 8
2.3 LUMINESCENCE 8
2.3.1 Photoluminescence (PL) *9*
2.4 ENERGY TRANSFER 10
2.4 QUENCHING OF LUMINESCENCE 11
2.6 PROPERTIES OF RARE EARTHS 12
2.7 LANTHANIDE ORTHOVANADATES 14
2.8 LANTHANIDE ORTHOPHOSPHATES 14
2.9 CRYSTAL STRUCTURES OF *GADOLINIUM*, *LANTHANUM*, AND *YTTRIUM* SYSTEMS 16
2.10 PHOSPHOVANADATES 19
2.11 REFERENCES 20

CHAPTER 3 EXPERIMENTAL AND RESEARCH TECHNIQUES **23**

3.1 INTRODUCTION 23
3.1.1 Method of synthesis *23*
3.1.2 X-ray diffraction (XRD) *24*
3.1.3 High resolution transmission electron microscopy (HRTEM) *26*
3.1.4 Scanning electron microscopy (SEM) *28*
3.1.5 Fourier Transform Infra-Red spectroscopy (FTIR) *30*
3.1.6 Ultraviolet-Visible spectroscopy (UV-VIS) *31*
3.1.7 Photoluminescence spectroscopy (PL) *34*
3.2 REFERENCES 36

CHAPTER 4 STRUCTURE AND PHOTOLUMINESCENT PROPERTIES OF GREEN-EMITTING TERBIUM DOPED $GdV_{1-x}P_xO_4$ PHOSPHOR PREPARED BY SOLUTION COMBUSTION METHOD **39**

4.1 INTRODUCTION 39
4.2 EXPERIMENTAL 40
4.2.1 Synthesis *40*
4.2.2 Characterization *41*
4.3 RESULTS AND DISCUSSION 41
4.3.1 Crystal Structure of $GdVO_4$ and $GdPO_4.H_2O$ *41*
4.3.2 X-ray diffraction *43*
4.3.3 Scanning electron microscopy *46*
4.3.4 Fourier transform infrared (FTIR) analysis *48*
4.3.5 UV-vis Spectroscopy *48*
4.3.6 Photoluminescence Spectroscopy *50*
4.4 CONCLUSION 57
4.5 REFERENCE 58

CHAPTER 5 DUAL EMISSION FROM Sm^{3+} AND Tm^{3+} ACTIVATED GADOLINIUM PHOSPHOVANADATE 61

5.1. INTRODUCTION 61
5.2. EXPERIMENTAL 62
5.2.1 Synthesis *62*
5.2.2 Characterization *63*
5.3. RESULTS AND DISCUSSION 63
5.3.1 X-Ray diffraction *63*
5.3.2 Scanning electron microscopy *64*
5.3.3 UV-Vis spectroscopy *66*
5.3.4 Photoluminescence spectroscopy *67*
5.4. CONCLUSION 72
5.5 REFERENCES 73

CHAPTER 6 COMBUSTION SYNTHESIS AND CHARACTERIZATION OF Sm^{3+} AND Tm^{3+} CO-ACTIVATED YTTRIUM ORTHOVANADATE PHOSPHATE 75

6.1 INTRODUCTION 75
6.2 EXPERIMENTAL 76
6.3 RESULTS AND DISCUSSION 77
6.3.1 XRD *77*
6.3.2 Surface morphology and elemental composition *80*
6.3.3 UV-Vis reflectance spectroscopy *82*
6.3.4 Photoluminescence *83*
6.4 CONCLUSION 89
6.5 REFERENCES 90

CHAPTER 7 SYNTHESIS AND CHARACTERIZATION OF Ln^{3+} (Ln = Dy, Sm, Tb) ACTIVATED LANTHANUM ORTHO-PHOSPHOVANADATE 92

7.1 INTRODUCTION 92
7.2 EXPERIMENT 93
7.2.1 Synthesis *93*
7.2.2 Characterization *94*
7.3 RESULTS AND DISCUSSION 94
7.3.1 X-ray Diffraction *94*
7.3.2 Morphology *96*

7.3.3 UV-Vis spectroscopy *98*
7.3.4 Photoluminescence *99*
7.5 CONCLUSIONS 103
7.6 REFERENCES 104

CHAPTER 8 EFFECT OF ANNEALING TEMPERATURE ON THE STRUCTURE AND OPTICAL PROPERTIES OF LANTHANUM RARE EARTH DOPED PHOSPHOVANADATE 105

8.1 INTRODUCTION 105
8.2 EXPERIMENTAL DETAILS 107
8.3 RESULTS AND DISCUSSION 108
8.3.1 X-ray diffraction (XRD) *108*
8.3.2 Scanning electron microscopy *109*
8.3.3 FTIR analysis *111*
8.3.4 Photoluminescence *112*
8.4 CONCLUSIONS 116
8.5 REFERENCES 117

CHAPTER 9 COMBUSTION SYNTHESIS AND CHARACTERIZATION OF $MV_{0.5}P_{0.5}O_4$: Sm^{3+}, Tm^{3+} (M = Gd, La, Y) 119

9.1 INTRODUCTION 119
9.2 EXPERIMENT 121
9.2.1 Materials *121*
9.2.2 Synthesis *121*
9.2.3 Characterization *122*
9.3 RESULTS AND DISCUSSION 122
9.3.1 X-ray diffraction *122*
9.3.2 Scanning electron microscopy *124*
9.3.3 UV-vis spectroscopy *126*
9.3.4 Photoluminescence spectroscopy *126*
9.4 CONCLUSION 128
9.5 REFERENCES 129

CHAPTER 10 SUMMARY, CONCLUSION AND FUTURE WORK 130

10.1 SUMMARY 130
10.2 FUTURE WORK 132
10.3 PUBLICATIONS 133
10.4 NATIONAL CONFERENCES 134
10.5 INTERNATIONAL CONFERENCE 135

Chapter 1: Introduction

1.1 Overview

The large quality of human life depends on a large degree of energy, and this is threatened unless renewable energy resources are developed in the near future [1]. Following an increasing awareness of energy crisis, climate change and environmental issues, and with the pressure exerted by this to the sustainable development of the society, people are looking for alternatives to fossil fuel that do not emit carbon dioxide [2]. Concerns about present energy policy, which relies heavily on fossil fuels that cause the above said problems, require the development of renewable energy resources [3]. One possible solution to tackle this problem is firstly to consider the use of clean energy sources and some devices which can easily save on the cost during their manufacturing.

Sunlight provides a clean, renewable and cheap energy source for people, while also serving as a primary energy source for another type of energy resources, such as water, bio-energy, wind energy and fossil fuel [4]. The conversion of solar energy (energy from the sun) directly into electricity is one of the most attractive renewable energy sources that could help replace fossil fuels and control global warming [5]. Since the first report in 1991 by O'regan and Grätzel, dye sensitized solar cells (DSSCs) have emerged as one of the most promising low-cost alternative for renewable generation of electricity [6]. They (DSSCs) are currently considered highly promising as a method for efficient and economical conversion of solar energy into electric power. Their advantages have been challenging the conventional solar cells in various aspects such as various colours, semi-transparency, low cost fabrication processes, environmentally friendly and relatively high conversion efficiency [7, 8]. Because of all these

advantages, several studies have been carried out in recent years with the aim of improving the performance of DSSCs.

A typical DSSC is composed of a mesoporous semiconductor metal oxide film, usually TiO_2, a dye sensitizer, which is responsible for light harvesting, an electrolyte and a counter electrode [9, 10, 11, 12, 13, 14]. The principle of energy conversion in DSSCs is based on the absorption of a photon by the sensitizer leading to the excited sensitizer and injects electrons into the conductions band of the TiO_2, leaving the sensitizer in the oxidised state. If the circuit is closed, the injected electrons flow over the external circuit through the TiO_2 network to arrive at the counter electrode and reduce the oxidized form of the redox mediator. The dye is regenerated by popular redox couples (usually iodine/iodide) in electrolyte [15, 15, 17, 18, 19].

Many groups have focused their efforts on improving and comprehending this sort of solar cells in different aspects. Nevertheless, DSSCs are still faced with major difficulties. Further improvement in the cost of fabrication, thermal stability and conversion efficiency is still needed. Nu H *et al* used axle-sleeve structured MWCNTs\PANI composite as a non-Pt material for counter electrode (CE) for DSSCs and they found the efficiency to be comparable to that of a DSSC consisting of expensive Pt CE [20]. Ahmad I *et al* reported another carbon nanomaterial based CE which demonstrated higher efficiency than Pt CE [9].

Again, an enormous number of studies have been focused on the dye itself to improve the light harvesting [21, 22, 23]. These studies have shown that, even the best dyes can absorb only visible light. Thus, the energy rich UV radiation and infrared (IR) from the sun are not fully used [24, 25, 26]. Another way of improving the light harvesting is by synthesizing the luminescent material that will absorb UV and IR and re-emit in visible region so that it is

reabsorbed by the dye again. However, very limited studies have been undertaken on these materials. Thus, a detailed study is needed to prepare luminescent materials that can be applied and used as down converter in DSSCs.

1.2 Problem Statement

The largest challenge for our global society is to find ways to replace the slowly but inevitably vanishing fossil fuel supplies by renewable resources and, at the same time, avoid negative effects from the current energy system on climate and environment [27]. There are many sources of energy that are renewable and considered to be environmentally friendly. These include hydropower, geothermal, biomass, solar power etc. Among these sources, solar photo-voltaic is a promising technology which has been demonstrated in renewable energy applications like solar cells, photoelectron-chemical conversion of CO_2, water splitting, and waste water treatment [28]. Another candidate of interest is dye-sensitized solar cell (DSSC), which is known as a new class of photo-voltaic devices. This class has attracted much attention in the past two decades due to their attractive qualities such as low production cost, short energy payback time and convenience for multiple application purposes [29]. Therefore, this class of technology is considered as a promising alternative to conventional solar cells.

On the other hand, the research has shown that the DSSCs have lower efficiencies output compared to Si based solar cells, and this has restricted them (DSSCs) to be a potential candidate for practical application [30]. Because of the low production cost of DSSC, our focus in this study was to synthesize down converting luminescent material which can act as a down-converting layer when it is exposed to UV radiation. For the practical use of DSSC, thermal and chemical stability are as important as the conversion efficiency [31]. On that note, studies have shown that Ultraviolet (UV) irradiation is the main parameter which affects the thermal

stability of DSSCs [32]. Hence, the UV radiation was found to be deleterious for DSSCs. Secondly, when a DSSC is exposed to UV, the dye photo-oxidises rapidly and the iodine present in the electrolyte is consumed irreversibly [33]. Furthermore, these new class of solar cells can only absorb visible light [26] and most of the solar UV and infrared (IR) wavelengths are not fully utilized. Common strategy that is mainly used to avoid UV light is to use a UV filter to absorb UV rays. However, this method wastes some part of the solar energy. This study is aimed at synthesizing and characterizing luminescent materials that can be used as down converters in DSSCs. In this work, the solution combustion method was used to synthesize $MV_{1-x}P_xO_4:Ln^{3+}$ (M= Gd, La, Y and Ln= Dy, Sm, Tb Tm) phosphor powders. The structure, surface morphology, luminescent properties and decay characteristics are reported.

1.3 Research objectives

- To synthesize $MV_{1-x}P_xO_4:Ln^{3+}$ (M= Gd, La, Y and Ln= Dy, Sm, Tb Tm) phosphor powders by solution combustion method
- To study the structure and surface morphology of $MV_{1-x}P_xO_4:Ln^{3+}$ (M= Gd, La, Y and Ln= Dy, Sm, Tb Tm) phosphor powders
- To investigate the photoluminescence properties of $MV_{1-x}P_xO_4:Ln^{3+}$ (M= Gd, La, Y and Ln= Dy, Sm, Tb Tm) phosphor powders
- To study the effect of annealing temperature on the structure and photoluminescence properties of $LaV_{1-x}P_xO_4:Ln^{3+}$ (Ln= Dy, Sm, Tb) phosphor powders
- To study the effect of Tm^{3+} co-doping on the structure and photoluminescence properties of $YV_{0.5}P_{0.5}O_4$: Sm^{3+} phosphor powders
- Conduct a comparative study on Sm^{3+} and Tm^{3+} co-activated $MV_{0.5}P_{0.5}O_4$ (M= Gd, La and Y)

1.4 Thesis Layout

Chapter 2 provides a theoretical background on concepts such as phosphors, luminescence (photoluminescence), energy transfer, quenching of luminescence, properties of rare earths, lanthanide ortho –vanadates and –phosphates and their structures. *Chapter 3* provides a brief description of the synthesis method and characterization techniques used in this study. *Chapter 4* discusses structure and photoluminescent properties of green-emitting terbium-doped $GdV_{1-x}P_xO_4$ phosphor prepared by solution combustion method. *Chapter 5* discusses dual emission from Sm^{3+} and Tm^{3+} activated gadolinium phosphovanadate. Combustion synthesis and characterization of Sm^{3+} and Tm^{3+} co-activated yttrium orthovanadate phosphate is discussed in *chapter 6*. In *chapter 7*, synthesis and characterization of Ln (Dy, Sm, Tb) activated lanthanum ortho-phosphovanadate is discussed. *Chapter 8* discusses the effect of annealing temperature on the structure and optical properties of lanthanum rare earth doped phosphovanadate. *Chapter 9* deals with the synthesis and characterization of $MV_{0.5}P_{0.5}O_4$: Sm^{3+}, Tm^{3+} (Ln = Gd, La, Y): Comparative study. Lastly, *chapter 10* provides a summary of the thesis and possible future work. The list of publications and conference attended are also included

1.5 References

1. Grätzel M, *Accounts of Chemical Research* 42 (2009) 1788–1798
2. Guo C, Li M, Xu Y, Li T, Ren Z, Bai J, *Applied Surface Science* 257 (2011) 8836–8839
3. Chou CS, Huang YH, Wu P, Kuo YT, *Applied Energy* 118 (2014) 12–21
4. Omar A, Abdullah H, *Renewable and sustainable energy reviews* 31 (2014) 149–157
5. Tigreros A, Dhas V, Ortiz A, Insuasty B, Martín N, Echegoyen L, *Solar Energy Materials and Solar Cells* 121 (2014) 61–68
6. O'Regan B and Grätzel M, *Nature* 353 (1991) 737
7. Balasingam SK, Lee M, Kang MG and Jun Y, *Chem. Commun.*, 49 (2013) 1471–1487
8. Kuo HP and Wu CT, *Solar Energy Materials and Solar Cells* 120 (2014) 81–86
9. Ahmad I, McCarthy JE, Bari M, Gunko YK, *Solar Energy* 102 (2014) 152–161
10. Bu IYY, *Ceramics International* 40 (2014) 3445–3451
11. Chen X, Jia C, Wan Z, Yao X, *Dyes and Pigments* 104 (2014) 48–56
12. Grätzel M, *Journal of Photochemistry and Photobiology C: Photochemistry Reviews* 4 (2003) 145–153
13. Hua Y, Wang H, Zhu X, Islam A, Han L, Qin C, Wong WY, Wong WK, *Dyes and Pigments* 102 (2014) 196–203
14. Jo HJ, Nam JE, Kim DH, Kim H, Kang JK, *Dyes and Pigments* 102 (2014) 285–292
15. He J, Hua J, Hu G, Yin XJ, Gong H, Li C, *Dyes and Pigments* 104 (2014) 75–82
16. Golobostanfard MR and Abdizadeh H, *Solar Energy Materials and Solar Cells* 120 (2014) 295–302
17. Neuthe K, Bittner F, Stiemke F, Ziem B, Du J, Zellner M, Wark M, Schubert T, Haag R, *Dyes and Pigments* 104 (2014) 24–33
18. Mozaffari S, Nateghi MR, Zarandi MB, *Solar Energy* 106 (2014) 63–71
19. Nazeeruddin MK, Baker RH, Grätzel M, *J. Phys. Chem. B* 107 (2003) 8981–8987

20. Niu H, Qina S, Maoa X, Zhanga S, Wanga R, Wana L, Xua J, Miaoa S, *Electrochimica Acta* 121 (2014) 285– 293
21. Lee W, Yuk SB, Choi J, Kim HJ, Kim HW, Kim SH, Kim B, Ko MJ, Kim JP, *Dyes and Pigments* 102 (2014) 13–21
22. Yu X, Ci Z, Liu T, Feng X, Wang C, Ma T, Bao M, *Dyes and Pigments* 102 (2014) 126–132
23. Wang L, Liang M, Zhang, Cheng YF, Wang X, Sun Z, Xue S, *Dyes and Pigments* 101 (2014) 270–279
24. Hafez H, Wul J, Lan Z, Li Q, Xie G, Lin J, Huang M, Huang Y, Abdel-Mottaleb M.S, *Nanotechnology* 21 (2010) 415201
25. Wu J, Wang J, Lin J, Xiao Y, Yue G, Huang M, Lan Z, Huang Y, Fan, Yin S, Sato T, *Scientific Reports* (2013) DOI: 10.1038
26. Li QB, Lin JM, Wu JH, Lan Z, Wang JL, Wang Y, Peng FG, Huang ML, Xiao YM, *Chinese Sci Bull* 56 (2011) 28–29
27. Grätzel M, *Accounts of chemical Research,* 42 (2009) 1788–1798
28. Chuen-Shii C, Huang H, Wu P, Kuo YT, *Applied Energy,* 118 (2014) 12–21
29. H Guo, He X, Hu C, Tian Y, Xi Y, Chen J, Tian L, *Electrochemica Acta,* 120 (2014) 23–29
30. Wu J, Wang J, Lin J, Xiao Y, Yue G, Huang M, Lan Z, Huang Y, Fan L, Yin S, Sato T, *Science Reports*, (2013) DOI: 10.1038/srep02058
31. Zahedifar M, Chamanzadeh Z, Mashkani H, *Journal of luminescence,* 135 (2013) 66–73
32. Chamanzader Z, Zahedifar M, Hosseinpoor SM, *Proceding of the 4th international conference on nanostructures (ICNS4)* (2012), Kish Island, I.R Iran
33. Liu J, Yao Q, Li Y, *Applied Physics Letters,* 88 (2006) 173119

Chapter 2 Theoretical overview

2.1 Introduction

This chapter discusses briefly the conceptual and a few selected theoretical background on the basic principles of phosphors, luminescence, energy transfer model, quenching of a luminescence and some crystal structures of $REVO_4$ and $REPO_4$ (RE = Gd, La and Y).

2.2 Phosphors

A phosphor is a material that exhibit light when exposed to electromagnetic radiation (e.g. ultraviolet radiation) [1] and it can be in the form of a powder or a thin film. This process of emission of light by materials is called luminescence. Phosphors are mostly inorganic solid materials consisting of a host lattice, usually intentionally doped with impurities such as rare earth ions and transition metals [2]. These impurities, which are intentionally introduced into the material, are referred to as activators [3]. Depending on the desired application(s), a phosphor can be incorporated with one, two or three activators not only for the production of different colours but also to efficiently enhance the luminescent intensity. On the other hand, if there are more than one activators incorporated into the matrix, then the second activator serves as a co-activator.

2.3 Luminescence

Luminescence is the phenomenon of emission of light from a material when it is exposed to external incident photon energy. This phenomenon can be due to the structural defects or the presence of impurities intentionally incorporated into the matrix. These imperfections within the material usually induce energy levels inside the band-gap or “forbidden band” between the valance and conduction band.

Luminescence can be classified into two main processes, namely, phosphorescence and fluorescence. The first one (*phosphorescence)* is usually a very slow process in which emission continues for few seconds, minutes or even hours after removing the source of excitation, whereas fluorescence is mainly a fast process in which emission stops abruptly after turning off the excitation source [4].

Furthermore, luminescence can be categorized based on the type of excitation used. For example, if the source of radiation is by heat, the luminescence will be termed thermoluminescence. If the source of radiation is through an electromagnetic radiation then is termed photoluminescence (PL). Cathodoluminescence is termed if the excitation source is by a beam of energetic electrons, electroluminescence occurs when the source of excitation is an electric current, triboluminescence occurs when the excitation source is by mechanical energy such as grinding. When the excitation source is by X-rays, the luminescence is termed x-ray luminescence. Chemiluminescence occurs when the material is excited by the energy of a chemical reaction and bioluminescence is generated by living organisms. In this study, the main emphasis was on the PL studies and the process will be discussed in details in the next section.

2.3.1 Photoluminescence (PL)

There are two major types of photoluminescence, namely, intrinsic and extrinsic photoluminescence. The intrinsic photoluminescence is observed in materials which contain no impurity atoms whereas extrinsic photoluminescence is caused by intentionally incorporated impurities and in most cases metallic impurities or defects [5].

2.3.1.1 Intrinsic photoluminescence

Intrinsic luminescence does not involve any foreign impurities, but it is a characteristic of the host lattice. There are numerous factors responsible for intrinsic photoluminescence. These include vacancies, structural imperfections, like, poor crystal ordering damage due to radiation and shock damage among others. Intrinsic photoluminescence can be categorized into three, namely, band to band, exciton and cross luminescence.

2.3.1.2 Extrinsic photoluminescence

Extrinsic photoluminescence is a direct consequence of the intentionally incorporated impurities present within the structure. Most of the observed types of luminescence that are practical applications belong to this category [5]. This type of luminescence in ionic and crystals and semiconductors can be classified into two types, namely, localized and unlocalized. In a delocalized luminescence the excited electrons and holes of the host lattice participate in the luminescence process, while in a case of the localized luminescence the excitation and emission processes are confined in a localized luminescence center, the host lattice does not contribute to luminescence process [5].

2.4 Energy transfer

Energy transfer is the process whereby energy is transferred from one system to another. The process of energy transfer in phosphors involves interaction between two luminescent centers referred to as the sensitizer (energy donor) and the activator (energy acceptor) and this interaction can be an exchange interaction (e.g. spectral or wave function overlap) or an electric or a magnetic multipolar interaction [4]. A luminescent center (donor) which is primarily excited by incident light and subsequently transfers the excitation energy to another luminescence center (acceptor) [6]. There are two main classes of energy transfer mechanisms,

namely, radiative and non-radiative. Each process relies on the overlap between the emission spectrum of the donor and the absorption spectrum of the acceptor.

Generally, the energy transfer can be explained by two phenomena, namely, Dexter exchange and Förster resonance. In the former, the donor and acceptor orbitals must overlap with each other, while in the later, the energy from the donor is transferred to the acceptor through a long range coloumbic interaction [7]. Energy transfer can happen between non-identical or identical luminescence centers. In the first situation, energy transfer process occurs only when the luminescence centers exhibit identical energy gaps between the ground state and the higher energy state. In the second situation, after absorbing energy by ions of the same type, ion one (donor) transfers its part of the energy to ion two through non-radiative transfer and relaxes to the ground state. Then, ion two (acceptor) is promoted to a higher energy state [8]. The process of energy transfer can also occur between the host crystal and the activator(s) leading to host excitation luminescence [7]. In this study, energy transfer was evaluated between both host to activator(s) and non-identical centers.

2.4 Quenching of luminescence

Luminescence quenching refers to the decrease in luminescence intensity in light emitting materials. There are various factors responsible for luminescence quenching including high temperatures and increased impurity concentrations. Quenching of luminescence resulting from higher temperatures is referred to as thermal quenching, while the one resulting from higher concentrations is called concentration quenching.

Thermal quenching can be defined as a reduction in luminescence intensity due to an increase in temperature. It occurs at high temperatures when thermal vibrations of atoms surrounding

the luminescent center transfer energy away from the center resulting in a non-radiative recombination, and a subsequent depletion of the excess energy as phonons in the lattice [4].

On the other hand, the intentionally incorporated impurities (activators) to the matrix can be added in small concentration, usually less than 10%. Each phosphor has an optimum activator concentration to produce maximum luminescence output. Increasing the concentration of the activator beyond this optimum concentration usually result in the decrease in the luminescence output. This phenomenon is called “concentration quenching”. The origin of this effect is thought to be the result of the excitation energy that is lost from the emitting state due to cross relaxation, which is called non-radiative energy transfer between activators [9].

2.6 Properties of rare earths

The rare earth elements (REE), also simply called rare earths (RE) or rare earth metals (REM) are a group of 17 elements. These elements are highlighted in the following periodic table (figure 2.1)

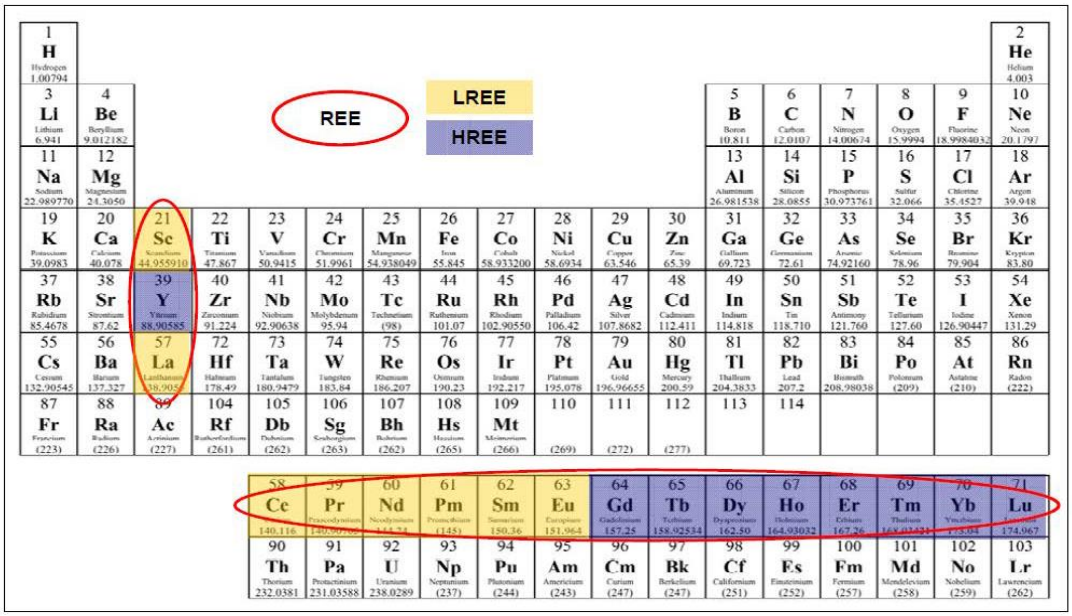

Figure 2.1. *Periodic table of the elements showing the division between LREEs and HREEs* [10].

This group consist of the elements scandium (Sc), yttrium (Y) and the 15 so called lanthanides (Ln) which are the elements lanthanum (La), cerium (Ce), praseodymium (Pr), neodymium (Nd), promethium (Pm), samarium (Sm), europium (Eu), gadolinium (Gd), terbium (Tb), dysprosium (Dy), holmium (Ho), erbium (Er), thulium (Th), ytterbium (Yb) and lutetium (Lu). The two elements, that is, scandium (Sc) and yttrium (Y), are considered rare earth elements only because they tend to occur in the same ore deposits as the lanthanides and exhibit similar chemical properties.

The rare earth elements can be categorized into two groups based on the electron configuration of each rare-earth element. The first group extends from lanthanum, atomic number 57 to gadolinium, atomic number 64 and it is called light-group rare earth elements (LREEs). The other group, extending from terbium, atomic number 65 to lutetium, atomic number 71 is called heavy-group rare earth elements HREEs.

The electronic structure of the RE atoms can be described in terms of a core of filled shells equivalent to the xenon (Xe) atom, and the following configuration: $4f^n\ 5d^{\ 0-1}\ 6s^2$. This gives a complete configuration as follows: $[Xe]^{54}\ 4f^n\ 5s^2 5p^6 5d^{0-1} 6s^2$ (n = 1, 2, ... , 14). Furthermore, after $5s^2 5p^6 5d^{0-1}\ s^2$ orbitals have been filled, the 4f shell will be filled gradually from n = 0 to 14 electrons. The 4f electrons of RE elements are well shielded by the full $5s^2 5p^6$ sub-shells and are deep-seated near the nucleus because they are “localized” and have lower energies. In the case of cerium (Ce), there is one 4f electron and the number of 4f electrons increases steadily through the group, until there is 13 ($4f^{13}$) for Ytterbium and the filled shell $4f^{14}$ for Lutetium [6].

2.7 Lanthanide orthovanadates

Phosphors (luminescent materials) absorb energy at various wavelength ranges (UV, visible light, infrared rays and so on) and emit many kinds of visible colors. Various luminescent materials are being developed currently, and their performance is improving. Among luminescent materials, rare earth orthovanadate compounds have been widely studied for their useful luminescent properties and unusual magnetic characteristics. Moreover, they show excellent thermal and chemical stability. These materials have been employed as highly efficient laser diode pumped micro-lasers, an efficient phosphor and as attractive polarizer materials [11]. Furthermore, they can be conveniently doped with trivalent lanthanide ions in order to develop luminescent materials widely used in optics and photonics [12].

Due to the similar ionic radii, electronic structures and electronegativities, yttrium, gadolinium or lutetium ions can be replaced easily with luminescence-active rare earth (RE^{3+}) ions (e.g. Eu^{3+}, Er^{3+}, Yb^{3+}, Ho^{3+}, Sm^{3+}or Tm^{3+}), in a wide range of concentrations, without strongly affecting the lattice structure [13]. It is well known that these lanthanide orthovanadates crystallize in two polymorphs, namely, monoclinic (m-) monazite-type and tetragonal (t-) zircon-type. With increasing ionic radius, lanthanides (Ln^{3+}) ions show a strong tendency towards monazite-structured orthovanadate on account of the higher oxygen coordination number of 9 compared to 8 of the zircon type [14]. Some crystal structures of $GdVO_4$, $LaVO_4$ and YVO_4 are shown in section 2.8.

2.8 Lanthanide orthophosphates

Lanthanide or rare-earth orthophosphates are very interesting class of host lattices for activator ions because of their variety of favorable properties. These properties include, among others, low water solubility, high refractive index (YPO_4 = 1.76, $LaPO_4$ = 1.85, $GdPO_4$ = 1.97), high

density (YPO_4 = 4.22, $LaPO_4$ = 5.0, $GdPO_4$ = 6 g/cc) which make them suitable candidates for a variety of applications [15]. They belong to the family of $LnPO_4$ phosphors and have received considerable attention in the past few years due to their high absorption and high luminescence efficiencies under vacuum ultra-violet (VUV) excitation. In addition, these orthophosphates possess high thermal and chemical stability properties [16].

As a lanthanide inorganic compound, lanthanide orthophosphates belong to the types of monoclinic monazite and the hexagonal xenotime [17]. If the ionic radius of the cation is smaller than that of Gd, the material will have the tetragonal (*I41/amd*, Z = 4) zircon structure [18]. Most of the other orthophosphates have the lower-symmetry monoclinic (*P21/n*, Z = 4) monazite structure. $LaPO_4$, specifically, one member of the rare earth orthophosphate family, exhibit five kinds of polymorphs: monazite (monoclinic, naturally abundant), xenotime (tetragonal, naturally abundant), rhabdophane (hexagonal), weinschenkite (monoclinic), and orthorhombic [19]. Some crystal structures of $GdPO_4$, $LaPO_4$ and YPO_4 are shown in the next section

2.9 Crystal structures of *gadolinium*, *lanthanum*, and *yttrium* systems

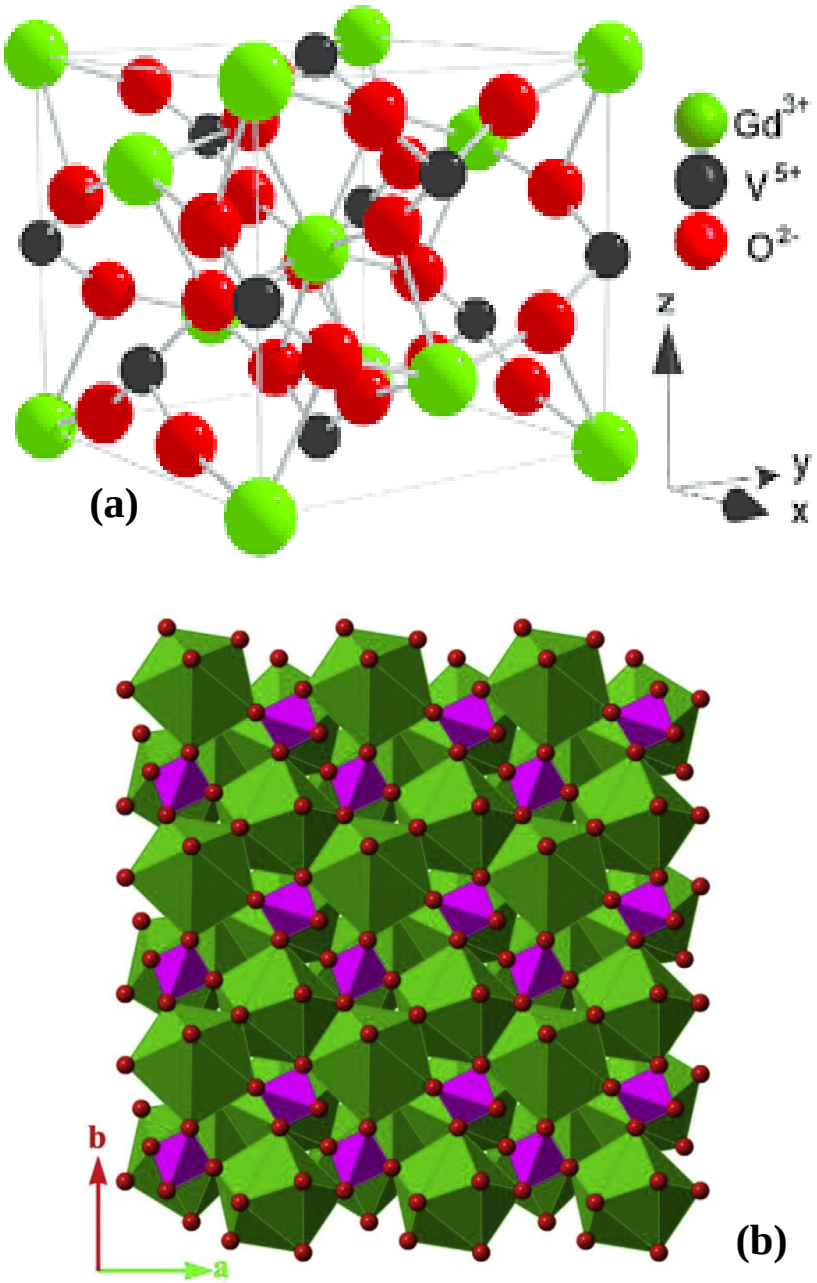

Figure 2.2. *Crystal structure of (a) $GdVO_4$* [20] *and (b) $GdPO_4$* [21].

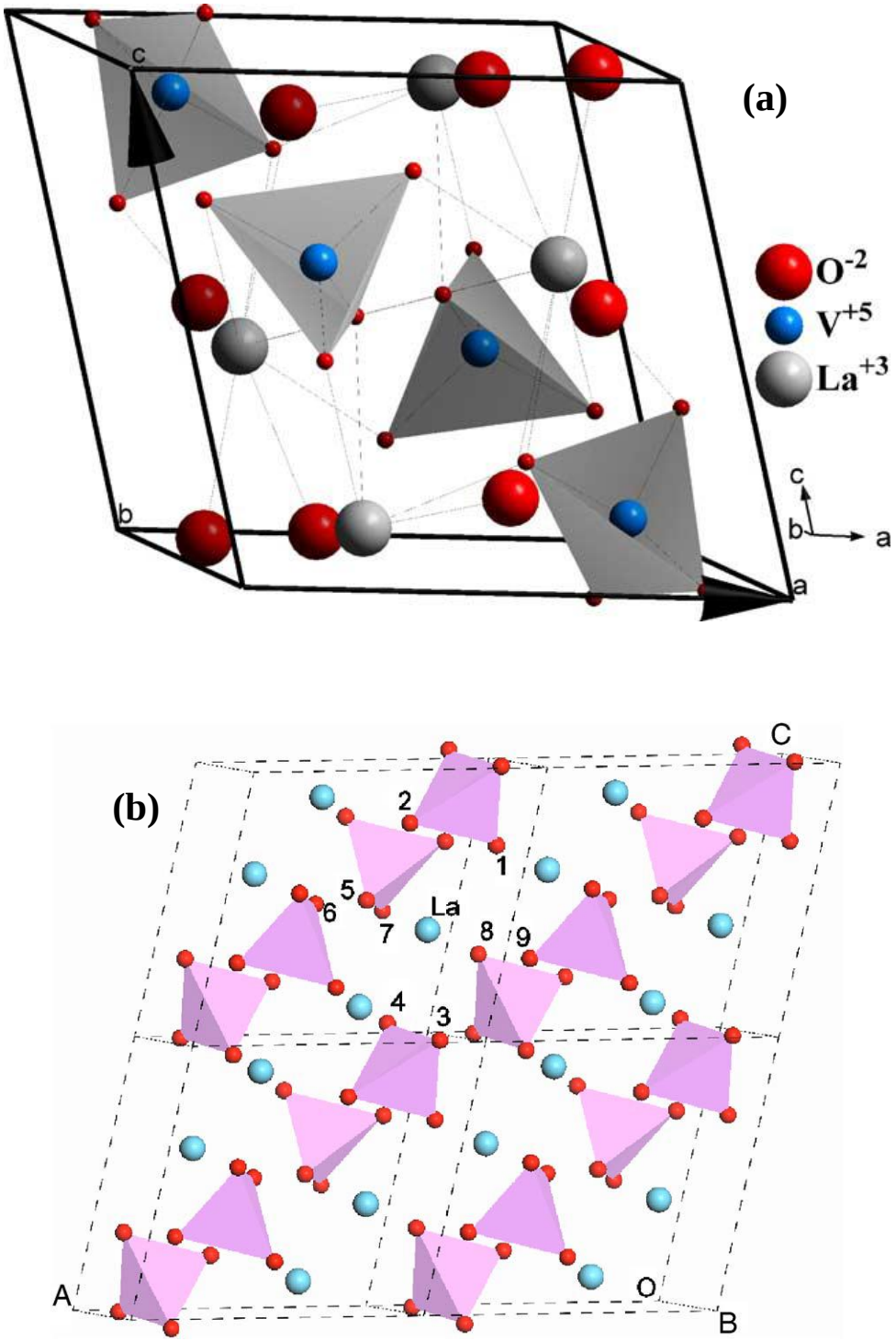

Figure 2.3. *Crystal structure of (a) $LaVO_4$* [22] *and (b) $LaPO_4$* [23].

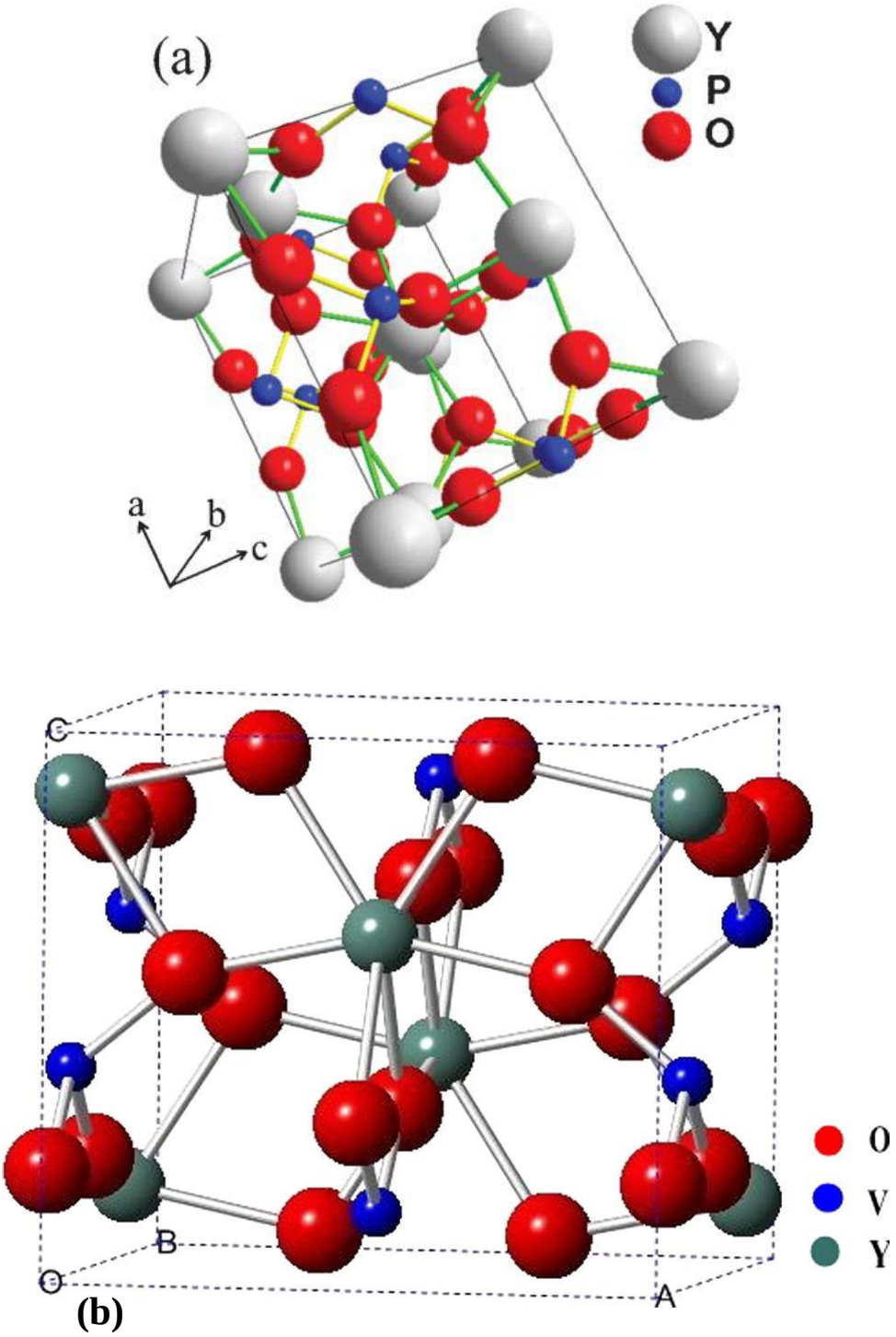

Figure 2.4. *Crystal structure of (a) YPO_4* [24] *and (b) YVO_4* [25].

The gadolinium systems ($GdVO_4$ and $GdPO_4$ crystals) are formed by GdO_8 polyhedron and V/PO_4 tetrahedron. Gd^{3+} ions located in dodecahedral coordination are linked with eight neighboring O^{2-} ions and V^{5+}/P^{5+} ions are tetrahedrally coordinated with O^{2-} ions [20, 26]. This is shown in figures 2.2 (a) and (b). In the lanthanum orthovanadate system ($LaVO_4$), each vanadium atom is at the center of distorted tetrahedron of oxygen. La exhibits an irregular coordination by nine oxygen atoms [22]. On the other hand, lanthanum orthophosphate system ($LaPO_4$) consists of PO_4 tetrahedra that are corner sharing only with LaO_9 polyhedra [27]. The crystal structures of lanthanum orthovanadate and orthophosphate are shown in figures 2.3(a) and (b) respectively. The yttrium systems (YVO_4 and YPO_4 crystals), adopt a tetragonal structure, with Y surrounded by 8 oxygens and V/P surrounded by 4 oxygens. Between YO_8 and V/PO_4 units, 2 oxygens are corner-sharing. V/PO_4 (tetrahedron) has S_4 symmetry whereas YO_8 (dodecahedron) has D_{2d} symmetry [24, 25]. This is illustrated in figures 2.4 (a) and (b) respectively.

2.10 Phosphovanadates

It was mentioned in section 2.6 and 2.7 that lanthanide orthovanadates and orthophosphate are very important hosts for rare earths and they exhibit excellent thermal and chemical properties. Since vanadium and phosphorus share almost the same properties, the two systems can be combined to form a mixture of both vanadate and phosphate group called lanthanide orthovanadate-phosphate or simply phosphovanadate. In this study, the multicomponent structures of rare earth phosphovanadates ($MV_{0.5}P_{0.5}O_4$) doped with different rare earth trivalent ions were prepared and their structure, surface morphologies and luminescent properties were investigated.

2.11 References

1. Tabaza WAI, Kroon RE, Swart HC, Synthesis and characterization of $MgAl_2O_4$ and $(Mg_xZn_{1-x})Al_2O_4$ mixed spinel phosphors, PhD thesis, University of the Free State, Bloemfontein, South Africa, 2014
2. Mothudi MB, Ntwaeborwa OM, Swart HC, Synthesis and characterization of strontium (Sr), barium (Ba) and Calcium (Ca) aluminate phosphors doped with rare earth ions, PhD thesis, University of the Free State, Bloemfontein, South Africa,, 2010
3. Dolo JJ, Dejene FB, Terblans JJ, Swart HC, Characterization of $Gd_2O_2S:Tb^{3+}$ phosphor powder and thin films, PhD thesis, University of the Free State, Bloemfontein, South Africa, 2011
4. Ntwaeaborwa OM, Kroon RE, Swart HC, Degradation of and energy transfer in oxide-based microscale and nanoscale phosphors doped with rare earth elements, PhD thesis, University of the Free State, Bloemfontein, South Africa, 2006
5. Dhlamini MS, Terblans JJ, Swart HC, Luminescent properties of synthesized PbS nanoparticle phosphors, PhD thesis, University of the Free State, Bloemfontein, South Africa, 2008
6. Tshabalala KG, Swart HC, Ntwaeaborwa OM, Synthesis and characterization of down conversion nanoparticles, PhD thesis, University of the Free State, Bloemfontein, South Africa, 2014
7. Motloung SV, Swart HC, Ntwaeaborwa OM, Dejene FB, Sol-gel synthesis and characterization of MAl_2O_4 (M = Zn or Mg) spinel doped, co-doped and triply doped nano-phosphors, PhD Thesis, University of the Free State, Phuthaditjhaba, South Africa, 2014

8. Krishnan R, Thirumalai J, Synthesis and luminescence properties of rare-earth doped molybdate micro/nanostructures for display applications, PhD thesis, B.S. Abdur Rahman University, Tamil Nadu, India, 2015
9. Han MK, Woo LK, Thiel PA, Pecharsky V, Corbett JD, Miller GJ, Rare-earth transitions-metal intermetallics:Structure-bonding-property relationships, PhD thesis, Iowa State University, Ames, United State, 2006
10. Smartdogmining.com/topics/all%20REE20not%20equal.html (accessed 16/05/2017)
11. Weiliu F, Xinyu S, Sixiu S, Xian Z, *J Solid State Chem.* 180 (2007) 284–290
12. Lisiecki R, Ryba-Romanowski W, Cavalli E, Bettinelli M, *J Lumin.* 130 (2010) 131–136
13. Jovanovic DJ, Antic Z, Krsmanovic RM, Mitric M, Dord-evic V, Bartova V, Dramicanin MD, *Opt. Mater.* 35 (2013) 1797–1804
14. Park SW, Yang HK, Chung JW, Chen Y, Moon BK, Choi BC, Jeong JH, Kim JH, *Physica B* 405 (2010) 4040–4044
15. Kumar GA, Balli RB, Kailasnathb M, Mimun LC, Dannangoda C, Martirosyan KS, Santhosh C, Sardar DK, *J. alloys and compds*. 672 (2016) 668–673
16. Kesavulu CR, Kesavulu CR, Basavapoornima CH, Viswanath CSD, Jayasankar CK, *J Lumin.* 171 (2016) 51–57
17. Zhang Z, Shi J, Wang X, Liu S, Wang X, *J Rare earths***,** 34 (2016) 1103
18. Lacomba-Perales R, Errandonea D, Meng Y, Bettinelli M, DOI: 10.1103/*Phys Rev B.* (2010) 81.064113
19. Huang X, *Opt. Mater.* 50 (2015) 81–86
20. Gavrilovic TV, Jovanovic DJ, Lojpur VM, Dordevic V, Dramićanin MD, *J Solid State Chem.* 217 (2014) 92–98

21. Meng C, Ding X, Zhao J, Li W, Ren C, Yang H, *Progress in Nuclear Energy* 89 (2016) 1–6

22. Bashir J, Khan MN, *Mater. Lett.* 60 (2006) 470–473

23. Wang J, Zhou Y, Lin Z, *App. Phys. Let.* 87 (2005) 051902

24. Zhang S, Wang L, Peng H, Li G, Chen K, *Mater. Chem. Phys.* 123 (2010) 714–718

25. Parchura AK, Ningthoujam RS, *RSC Advances.* 2 (2012) 10854–10858

26. Liu Y, Liu G, Wang J, Dong X, Yu W, *New J. Chem.* 39 (2015) 8282—8290

27. Phadke S, Nino JC, M. Islam S, *J. Mater. Chem.* 22 (2012) 25388

Chapter 3 Experimental and research techniques

3.1 Introduction

The phosphor powders reported in this thesis were synthesized by solution combustion method. Various characterization techniques including X-ray diffraction (XRD), field emission scanning electron diffraction (FESEM), energy dispersive x-ray spectroscopy, high resolution transmission electron microscopy (HRTEM), Fourier transform infrared spectrometer (FTIR), UV-Vis spectrophotometer (UV-Vis) and fluorescence spectroscopy (PL) were used to characterize these phosphor powders. XRD, HRTEM and FESEM were used for the crystal structure, phase identification and surface morphology. The stretching modes of vibration of the samples were determined by FTIR. UV-Vis was used to obtain the diffuse reflectance measurements. The photoluminescent properties were investigated by using fluorescence spectroscopy F7000. This chapter also discusses the method of synthesis (solution combustion method) and presents a brief description of each technique used for characterization of lanthanide phosphovanadate phosphors.

3.1.1 Method of synthesis

Over the past decade, extensive efforts have been devoted to the synthesis of the nanoparticles because of their unusual physical and chemical properties when compared to their bulk counter parts. To date, a considerable number of preparation methods have been reported [1]. These methods include co-precipitation [2], hydrothermal [3], solvothermal [4], sol-gel [5], combustion method [6] and solid-state reaction [7]. For this study, a solution combustion method was used to synthesize the mixed multicomponent structures of rare earth activated phosphovanadate.

A combustion synthesis (CS) or self-propagating high-temperature synthesis (SHS) is an effective energy saving method for the synthesis of a variety of advanced materials [8]. A combustion process involves a redox (reduction – oxidation) reaction between an oxidizer such as metal nitrates and an organic fuel such as urea (CH_4N_2O), carbonhydrazide (CH_4N_4O), citric acid ($C_6H_8O_7$) or glycine ($C_2H_5NO_2$) [9]. The choice of hydrate nitrates is mostly preferred compared to other salts because of their good solubility in water which allows them to maintain a highly homogeneous solution, and urea, on the other hand, is the most convenient fuel that can be used in the combustion processes because of its relatively low price, availability, commercially grade and safety [10]. The other special feature about this method is the fact that it can be conducted in two ways. Firstly, both the oxidizer and the fuel can be mixed together to form a paste. Secondly, the same primary reactants can now be mixed in an aqueous solution by using a deionized water [11]. Thus, the latter preparation route in comparison to other preparation methods, which are time consuming, expensive and sometimes complex, has distinct advantages such as low cost fast process, with energy and time saving to produce pure nano crystalline powders [12].

3.1.2 X-ray diffraction (XRD)

X-ray powder diffraction (XRD) is a non-destructive, quick analytical technique and it is mainly used for phase identification of a crystalline material. It is a technique used to characterize the crystallographic structure, crystallite size (grain size), preferred orientation in polycrystalline or powdered solid samples and it is also a common method for determining lattice strains in crystalline materials [13]. The measuring principle is based on the reflection of X-rays by matter.

The basic principle for data acquisition is based on the fact that a beam of of X-rays from the source will strike the sample. During this process, some X-rays get absorbed and others are mainly reflected. However, because of the diffraction, there will eventually be the presence of some waves overlapping which depend on the geometrical orientation which can generate constructive and destructive interference. If the Bragg Equation (3.1) is fulfilled a maximum of the reflected intensity is mainly detected.

$$n\lambda = 2d_{hkl}\sin\theta \qquad 3.1$$

where λ, d and θ are the wavelength, lattice spacing and the angle respectively. Figure 3.1 shows a schematic diagram of XRD.

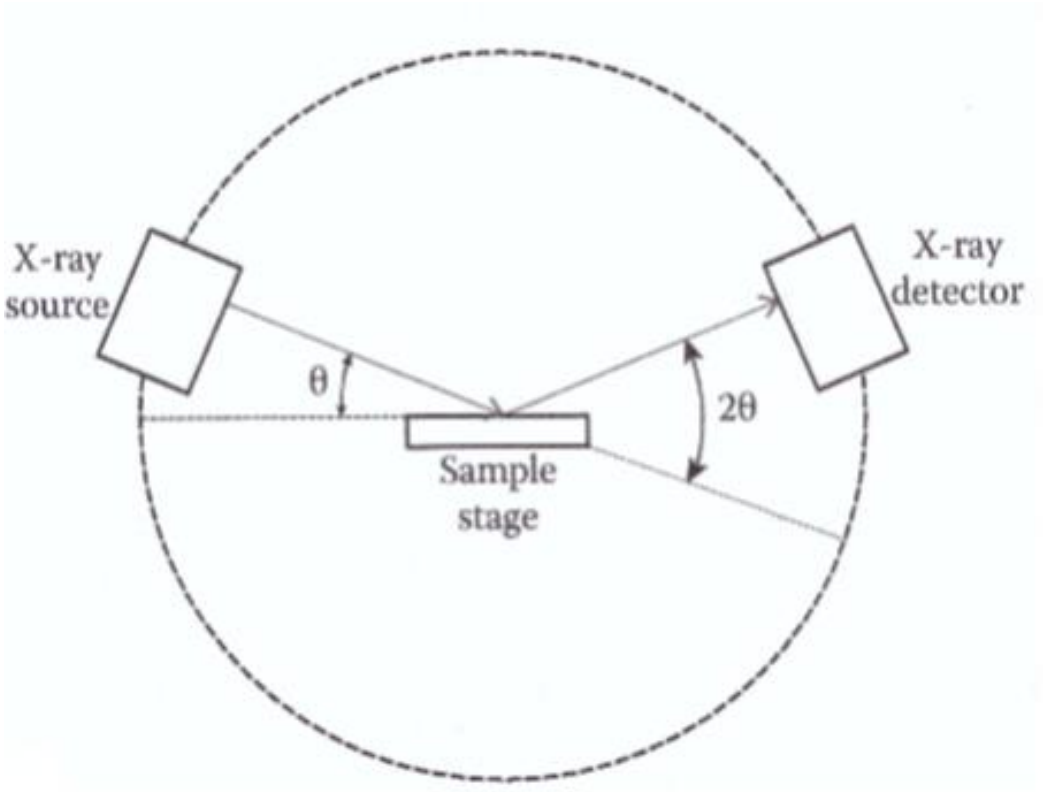

Figure 3.1 *Schematic representation of XRD operation* [14].

The X-ray hits the sample with an adjustable angle θ. The intensity of the reflected beam is then measured with a detector. The source or detector (sometimes both) moves in such a way

that the angle between them is always 2θ. X-ray-reflexes can only be detected if any lattice plane with the Miller indices (*h k l*) fulfils the equation (3.1). The value of d_{hkl} for tetragonal and monoclinic structures can be found by using equations 3.2 and 3.3 respectively.

$$d_{hkl} = \frac{ac}{\sqrt{(h^2 + k^2)c^2 + l^2a^2}} \qquad 3.2$$

$$\frac{1}{d^2{}_{hkl}} = \frac{1}{\sin^2\beta}\left(\frac{h^2}{a^2} + \frac{k^2\sin^2\beta}{b^2} + \frac{l^2}{c^2} + \frac{2hl\cos\beta}{ac}\right) \qquad 3.3$$

where *h*, *k*, *l* are the Miller indices of the diffracting planes, *a*, *b*, *c* are the axes and β is the angle. The measured spectra show maxima of intensity at certain angles due to constructive interference. The crystalline phases inside the sample can be identified and the prominent peaks can be assigned, by comparing the spectra to references from the Joint Committee on Powder Diffraction Standards (JCPDS) data. The X-ray diffractometer used in this study was Bruker D8 Advanced Powder Diffractometer.

3.1.3 High resolution transmission electron microscopy (HRTEM)

Transmission electron microscopy is an imaging technique in which a beam of electrons is focused onto a specimen causing an enlarged image to either appear on a fluorescent screen or layer of photographic film, or to be detected by a CCD camera [15]. The basic column of a transmission electron microscope is shown in figure 3.2.

The electrons are produced from the electron gun situated at the top of the system. The electron gun is usually thermionic tungsten which can be resistively heated to 2800 K in a vacuum of 0.1 mPa to give an electron sufficient energy to overcome the work function of the metal. The

anode potential is considerably higher than in an SEM and is typically 100 – 400 kV [16]. The generated beam of electrons is focused into a tight, coherent beam by system of electromagnetic lenses and apertures then focused onto a thin sample. The beam has enough energy for the electrons to be transmitted through the sample. The transmitted electron signal is greatly magnified by a series of electromagnetic lenses [15]. The magnified transmitted signal may be observed in either an electron diffraction mode or direct imaging mode. Data is accumulated from the beam after it passes through the sample. The electron diffraction mode is employed for crystalline structure analysis, while the image mode is used for investigating the microstructure, e.g. the grain size and lattice defects [15]. In this study, Jeol-Jem 2100 transmission electron microscopy was used to study the crystallinity and the surface morphology of the powder samples.

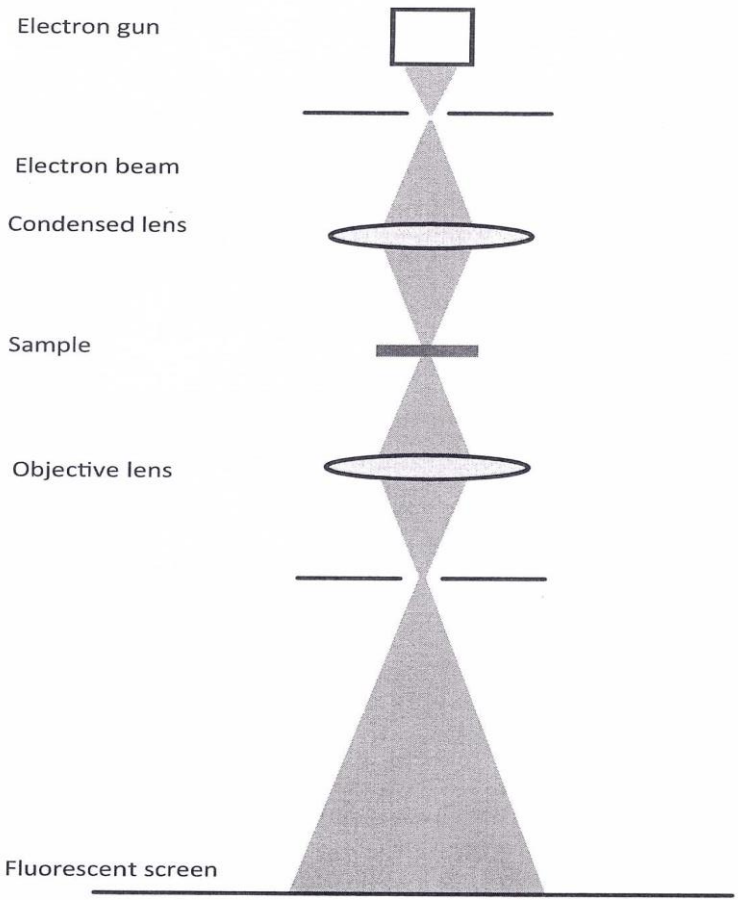

Figure 3.2 *Schematic diagram of electron diffraction in the TEM* [17].

3.1.4 Scanning electron microscopy (SEM)

Scanning electron microscopy (SEM) is a technique whereby a beam of energetically well-defined and highly focused electrons is scanned across a material (sample). The microscope uses a lanthanum hexaboride (LaB_6) source and is pumped using turbo and ion pumps to maintain the highest possible vacuum. The technique can provide information about topography, morphology and crystallography. If the system is equipped with energy dispersive x-ray spectrometer (EDS), it can also provide information about chemical composition of the material [18].

The process starts with the electrons emitted from the electron gun. The electron beam, which typically has an energy ranging from a few hundred eV to 100 keV, is attracted to the anode, condensed and focused by the condenser lens and the objective lens into a beam with a very fine focal spot. The beam passes through pairs of scanning coils or pairs of deflector plates in the electron optical column, typically in the objective lens, which deflect the beam horizontally and vertically so that it scans in a raster fashion over a rectangular area of the sample surface. During this process, the beam produces, among others, secondary and backscattered electrons from the measured sample. These electrons are collected by a secondary electron or a backscattered electron detector, converted to a voltage, and amplified. Thus, the X-ray energy will be converted into a voltage signals, and sent to a pulse processor, which measures the signals that passes onto an analyzer for data display for further analysis. As the beam continues to scan through the sample surface, the display beam will be synchronized. A schematic diagram of SEM is shown in figure 3.3.

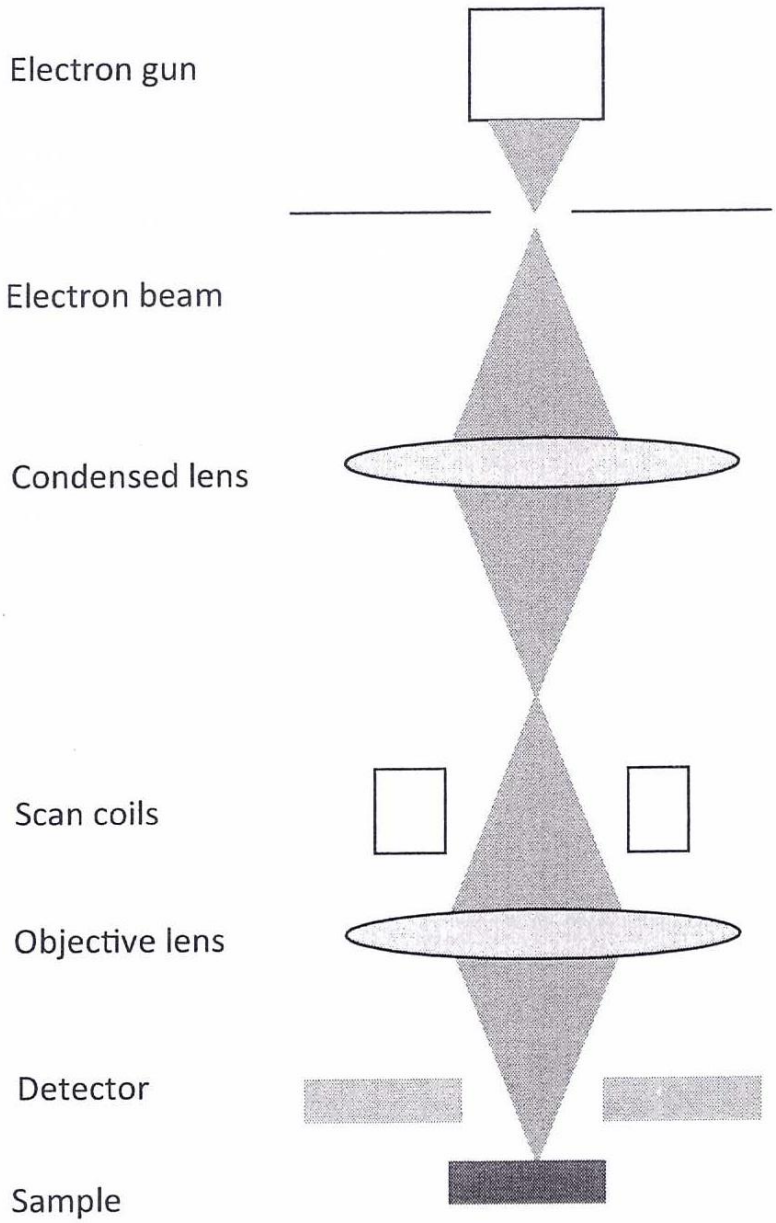

Figure 3.3 *Schematic drawing showing the electron column, the deflection system and the electron detectors* [17].

The elemental composition on the other hand, was determined using energy dispersive x-ray spectroscopy (EDS) usually fitted onto the SEM instrument. EDS analysis utilizes characteristic x-rays coming from the surface when the high-energy electrons strike the sample. The normal operating acceleration voltages, to generate the high-energy electrons, range between 20 and 30kV. The penetration depth of the electrons into the sample depends on the accelerating voltage. The generated x-ray photons enter a lithium drifted silicon detector, Si

(Li), in which electron-hole pairs are created. An electron from an outer higher-energy shell then fills the hole, and the difference in energy between the higher energy shell and the lower energy shell is released in the form of an X-ray. These x-rays are characteristic of the difference in energy between the two shells, and of the atomic structure of the element from which they were emitted. In this study, Jeol JSM-7800F field emission scanning electron microscope (FE-SEM) fitted with Oxford Aztec 350 X-Max80 energy-dispersive X-ray spectroscopy (EDS) was used to study the surface morphology and the elemental composition of the prepared powder samples.

3.1.5 Fourier Transform Infra-Red spectroscopy (FTIR)

Infrared (IR) spectroscopy is a non-destructive analytical technique used to identify organic and inorganic compounds [19]. It is a method of obtaining infrared spectra by first collecting an interferogram of a sample signal using an interferometer and then performing a Fourier Transform on the interferogram to obtain the final spectrum [20]. In the infrared spectroscopy, IR radiation is mainly passed through a sample where some radiation is absorbed by the sample and some of it is passed through (transmitted). The resulting spectrum represents the molecular absorption and transmission, creating a molecular fingerprint of the sample.

The selection rule on this fingerprint is that there are no two unique molecular structures which produce the same infrared spectrum. This makes infrared spectroscopy useful for several types of analysis such as identifying unknown materials as well as the amount of components in a given mixture [21].

FTIR system consists of three basic parts. Although an interferometer is the essential part, radiation source and a detector are also equally important. A block diagram of FTIR

spectroscopy is shown in figure 3.4. The IR beam emitted from the source enters the interferometer. The beam is split into two by a beam splitter upon entering the interferometer. One beam reflects off from a flat fixed mirror while the other beam reflects off from a flat movable mirror. These two beams later recombine to form interferogram. The incident beam to the interferometer is used for wave calibration, mirror position control and to collect data of the spectrometer. The beam enters the sample chamber where it is transmitted through the sample. Then the detector detects the beam for measurement [22].

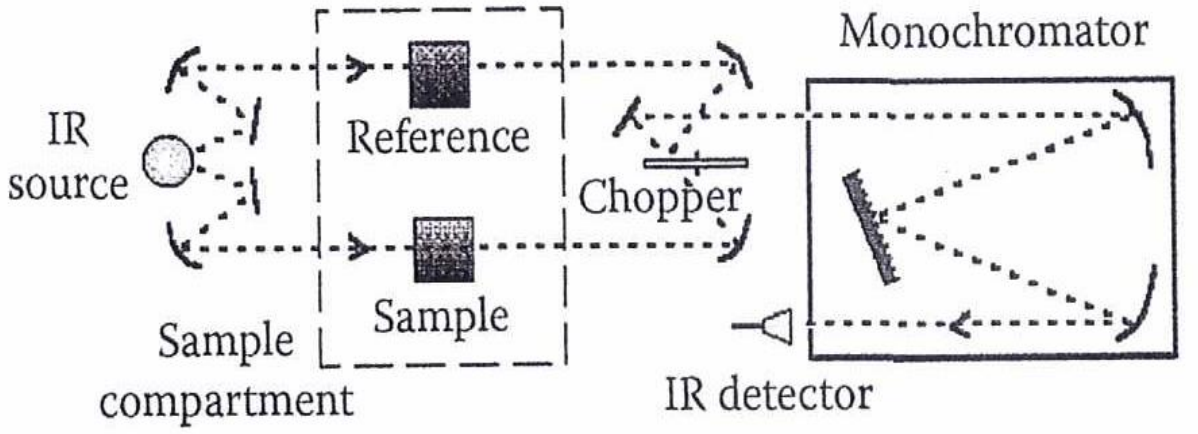

Figure 3.4. *Fundamental components of an FTIR spectrometer* [14].

3.1.6 Ultraviolet-Visible spectroscopy (UV-VIS)

When the electromagnetic radiation in a certain medium is projected towards a solid material, the light waves are reflected, absorbed or transmitted and the ability of materials to absorb and reflect is an important parameter that is used by the ultraviolet and visible (UV-Vis) spectroscopy to identify how phosphor materials respond to electromagnetic radiation [23]. UV-Vis absorption spectroscopy measures of the attenuation of a beam of light after it passes through a sample or after reflection from a sample surface [24].

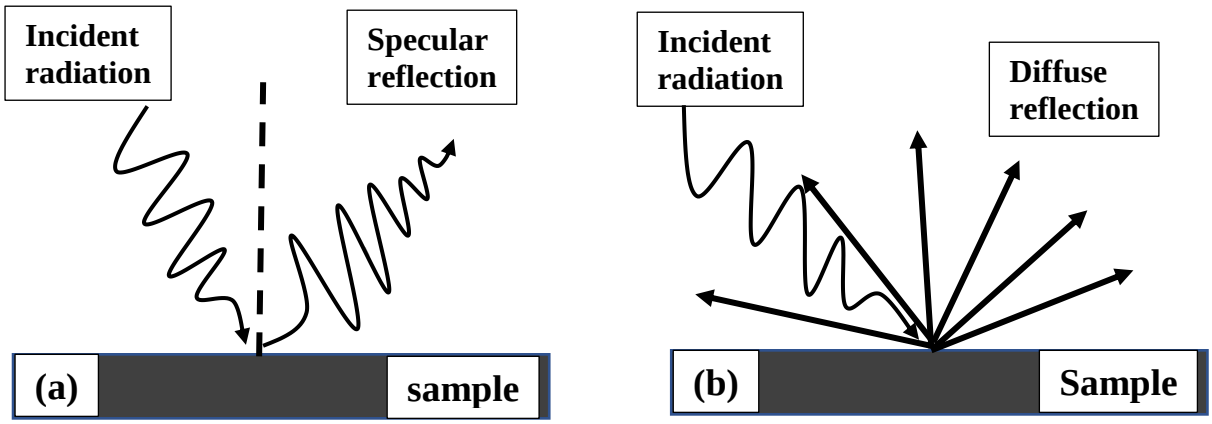

Figure 3.5. *A schematic diagram showing (a) specular and (b) diffuse reflection.*

The measurement of radiation reflected from a surface constitutes the area of spectroscopy known as diffuse reflectance spectroscopy (DRS). Diffuse reflectance spectrometry has one of the two components of the reflected radiation from an irradiated sample, namely specular reflected radiation and diffuse reflected radiation. Reflection of light or radiation from a smooth surface is called specular reflection while reflection from a rough surface is referred to as diffuse reflection and the processes are shown in figure 3.5.

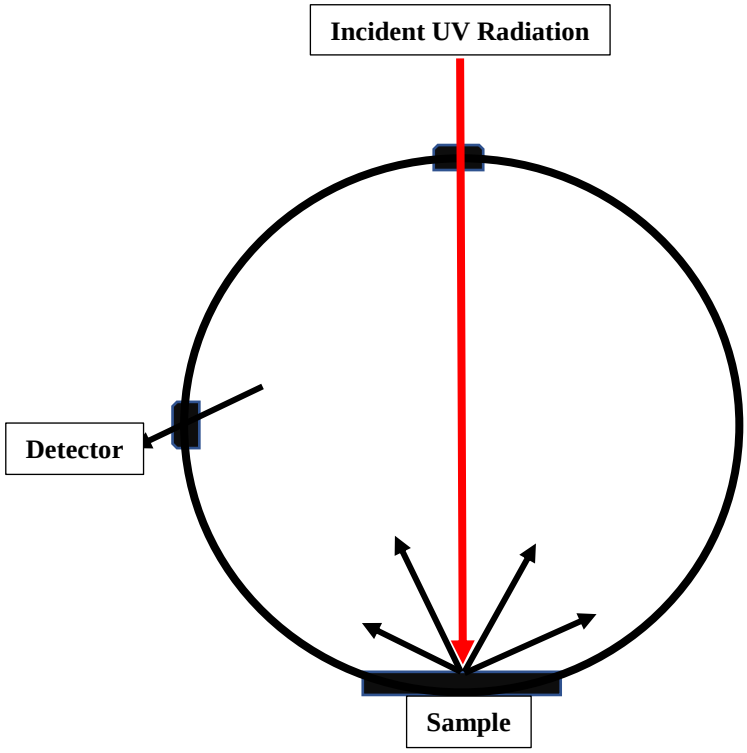

Figure 3.6. *Schematic diagram of integrating sphere.*

UV-Vis diffuse reflectance spectrophotometry consists mainly of four main components, namely light source (usually Deuterium and Tungsten lamps), integrating sphere, sample holders and detectors. An integrating sphere is an optical device used to collect and measure electromagnetic radiation. It has a hollow spherical cavity with its interior covered with a diffuse white reflective coating, with small holes for entrance and exit ports. Simplified diagram of an integrating sphere is shown in figure 3.6.

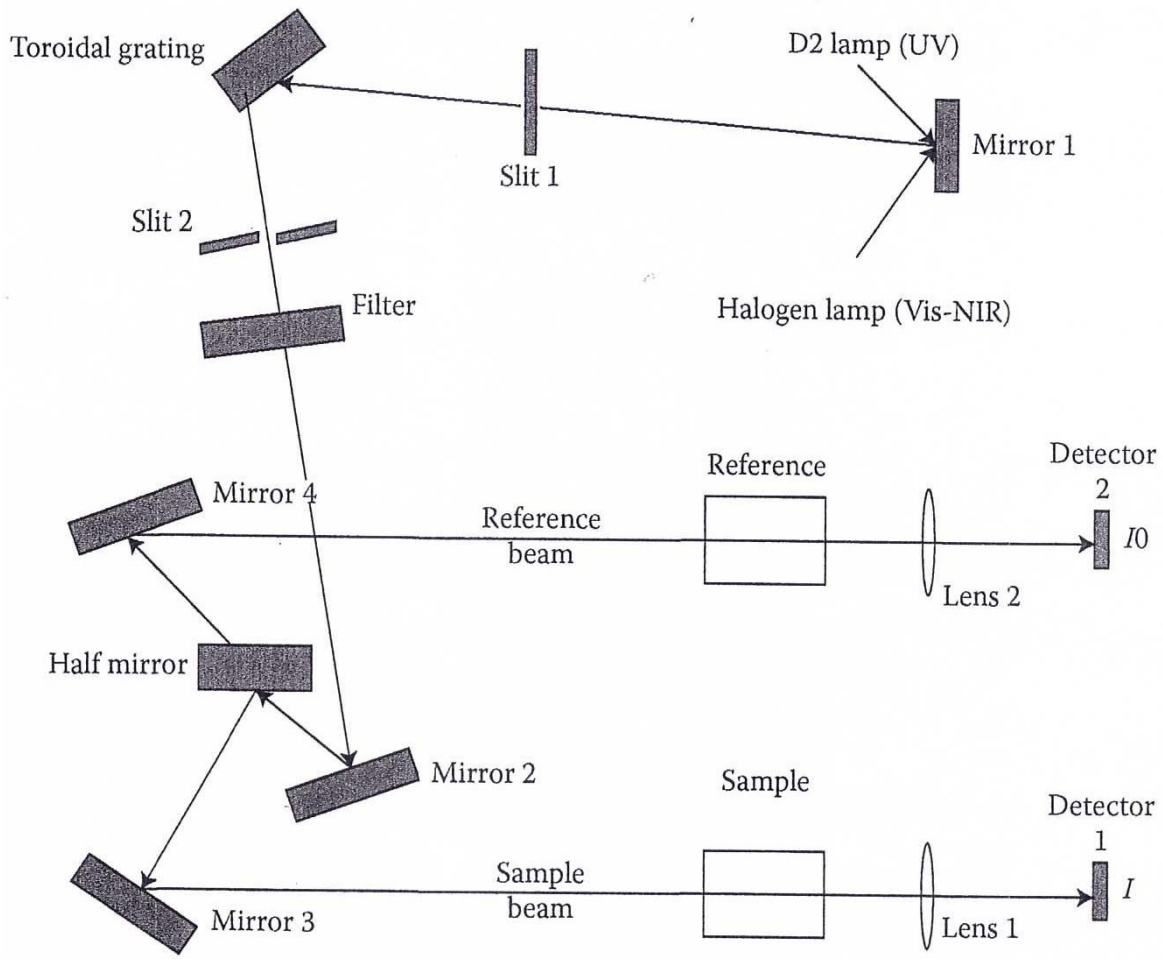

Figure 3.7 *Schematic diagram of UV spectroscopy* [14].

The sample, which is confined within an integrating sphere, is irradiated with UV and/or visible radiation. Some of the incident radiation absorbed by the sample while some is diffusely reflected. The diffuse reflected radiation is detected by the detector, which subtracts the

collected radiation from the source radiation to determine the amount that has been absorbed. The reflectance data can be converted to absorbance by Kubelka-Munk equation 3.3 [25].

$$F(R) = \frac{K}{S} = \frac{(1-R)^2}{2R} \qquad 3.3$$

Where K is the absorption, S is the scattering and R is the reflectance of the sample. This equation is very important for approximating the band gap energy. The block diagram of UV system is shown in figure 3.7. The UV spectroscopy used in this work was UV-vis spectrophotometer Lambda 950 (PerkinElmer).

3.1.7 Photoluminescence spectroscopy (PL)

Photoluminescence (PL) spectroscopy is a non-destructive, non-contact method for probing an electron structure of the materials [15]. When electromagnetic radiation is directed onto a solid material, the electrons in the ground state upon the absorption of the external photons will eventually get promoted to the excited state. Later the electrons are de-excited to their lower or ground state and, thus, releasing the absorbed radiation in a form of photons (light). This process of emission of light is called luminescence. Thus, the radiative part of the relaxation following the excitation is the essence of luminescence spectroscopy.

The photoluminescence instrument used in this study was mainly using a continuous Xenon lamp with the power of ~ 50W. This instrument is coupled with a variable wavelength ranging from 200–1000nm. There are mainly two types of luminescence spectra that can be obtained from PL instrument, namely excitation and emission spectrum respectively. The emission and excitation spectra are characteristic of the phosphor sample. The excitation spectrum gives information on the position of excited states while an emission spectrum provides information

on the spectral distribution of the light emitted by a phosphor sample. Figure 3.8 shows optical system of fluorescence spectrophotometer.

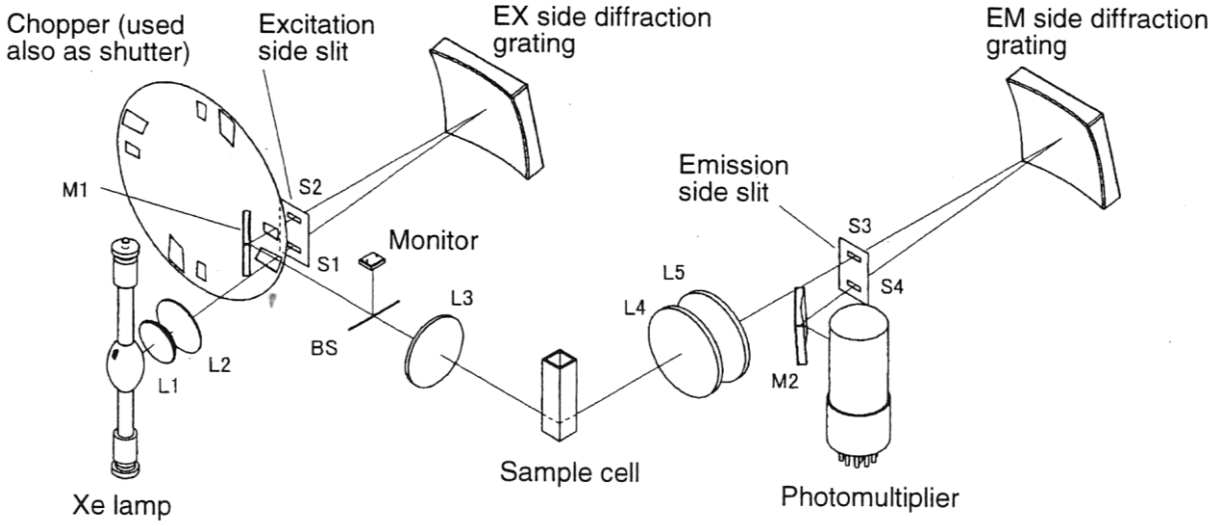

Figure 3.8 *Schematic diagram of the optical system of the F-7000 fluorescence spectrophotometer* [26].

The fluorescence of phosphors is usually visible because the excitation wavelength is usually in the UV region and the corresponding emission occurs in the visible region of the spectrum. Practically, all fluorimeters will have at least five components, which include the source, two wavelength discriminators, a sample holder and a detector. The PL system used in this work was HITACHI F-7000 fluorescence spectrophotometer.

3.2 References

1. Wang H, Odawara O, Wada H, *J Alloys Compds*. 683 (2016) 1- 6
2. Berna B, Seda B, *Mater. Chem. Phys.* 173 (2016) 200 - 204
3. Mahapatra S, Ramanan A, *J Alloys Compds.* 395 (2005) 149 –153
4. Zhu Y, Ni Y, Sheng E, *Mater. Res. Bull.* 83 (2016) 41– 47
5. Alcaraz L, Isasi J, Fernández M, Díaz-Guerra C, *Mater. Chem. Phys.* 145 (2014) 18 - 26
6. Gayathri TH, Yaremchenko AA, Zakharchuk K, James J, *J Alloy Compds.* 672 (2016) 549 - 557
7. Lin Z, Han X, Zaldo C, *J Alloy Compds.* 492 (2010) 77–82
8. Mukasyan AS, Epstein P, Dinka P, *Proceedings of the Combustion Institute* 31 (2007) 1789 –1795
9. Mothudi MB, Ntwaeborwa OM, Swart HC, Synthesis and characterization of strontium (Sr), barium (Ba) and Calcium (Ca) aluminate phosphors doped with rare earth ions, PhD thesis, University of the Free State, Bloemfontein, South Africa, 2010
10. Saket S, Rasouli S, Ghasemi E, Tahmasebi K, *J Mater. Sci. Eng.* 4 (2010) 1934 - 8959
11. Thomas ALS, Rajeshwar K, Solution combustion synthesis of oxide semiconductors, PhD Thesis, University of Texas, Texas, United States, 2015
12. Sherikar BN, Umarji AM, International Journal of Modern Physics: Conference Series, 22 (2013) 217–223
13. Koao LF, Dejene FB, Swart HC, Synthesis and characterization of Ce^{3+} doped silica (SiO_2) nanoparticles co-doped with Al^{3+} or Mg^{3+} ions, MSc Thesis, University of the Free State, Phuthaditjhaba, South Africa, 2009

14. Sunandana SC, Introduction to Solid State Ionics Phonomenology and Applications, 2016
15. Bem DB, Dejene FB, Swart HC, Luyt AS, Thermal, Structural and luminescent properties of long afterglow $MAl_xO_y:Eu^{3+}$, Dy^{3+} (M: Sr, Ba) phosphors, PhD Thesis, University of the Free State, Phuthaditjhaba, South Africa, 2010
16. Tshabalala KG, Swart HC, Ntwaeaborwa OM, Synthesis and characterization of down conversion nanoparticles, PhD thesis, University of the Free State, Bloemfontein, South Africa, 2014
17. Locharoenrat K, Optical properties of solids, 2016
18. Bikowski A, Manzke R, Ellmer K, Grundmann M, The relation between the deposition process and the structural, electronic, and transport properties of magnetron sputtered doped ZnO and $Zn_{1-x}Mg_xO$ films, PhD Thesis, University of Berlin, Berlin, Germany, 2014
19. Dhlamini MS, Terblans JJ, Swart HC, Luminescent properties of synthesized PbS nanoparticle phosphors, PhD thesis, University of the Free State, Bloemfontein, South Africa, 2008
20. Ntwaeaborwa OM, Kroon RE, Swart HC, Degradation of and energy transfer in oxide-based microscale and nanoscale phosphors doped with rare earth elements, PhD thesis, University of the Free State, Bloemfontein, South Africa, 2006
21. Baisitse TR, Engelbrecht JAA, Botha JR, Characterization of InAs-Based epilayers by FTIR spectroscopy, MSc Thesis, Nelson Mandela Metropolitan University, Port Elizabeth, South Africa, 2007
22. Motloung SV, Swart HC, Ntwaeaborwa OM, Dejene FB, Sol-gel synthesis and characterization of MAl_2O_4 (M = Zn or Mg) spinel doped, co-doped and triply doped

nano-phosphors, PhD Thesis, University of the Free State, Phuthaditjhaba, South Africa, 2014

23. Foka KE, Dejene FB, Swart HC, Synthesis and characterization of long afterglow phosphors ($SrAl_2O_4:Ce^{3+}$ $SrAl_2O_4:Tb^{3+}$, $CaAl_xO_y:Tb^{3+}$, $Y_3Al_5O_{12}:Eu^{3+}$) using solution combustion method, MSc Thesis, University of the Free State, Phuthaditjhaba, South Africa, 2011
24. Noto LL, Ntwaeaborwa OM, Swart HC, Persistent luminescence mechanism of tantalite phosphors, PhD Thesis, University of the Free State, Bloemfontein, South Africa, 2014
25. Koao LF, Dejene FB, Swart HC, Material properties of semiconducting nanostructures synthesized using the chemical bath deposition method, PhD Thesis, University of the Free State, Phuthaditjhaba, South Africa, 2013
26. Dzimbeg-Malcic V, Barbaric-Mikocevic Z, Atric K, *technical Gazette*, 18, 1(2011) 117–124
27. HITACHI F-7000 fluorescence spectrophotometer manual

Chapter 4 Structure and photoluminescent properties of green-emitting terbium doped $GdV_{1-x}P_xO_4$ phosphor prepared by solution combustion method

Luminescence 31(2016) 1069–1076

4.1 Introduction

Gadolinium orthovanadate ($GdVO_4$) and orthophosphate ($GdPO_4$) based phosphors have been extensively investigated owing to their interesting properties such as high melting point, low water solubility, high chemical and thermal stability, efficient energy absorption and transfer [1 - 4]. For these reasons, they are extensively applied as lasers, ceramics, sensors, phosphors, and heat-resistant materials [5 - 7]. $GdPO_4$ belongs to two polymorphic types, namely, the hexagonal type (for hydrated) and monoclinic monazite type (for anhydrous) [8]. GdVO4 also has two polymorphs, namely tetragonal (t-) $LnVO_4$ with zircon structure and monoclinic (m-) $LnVO_4$ with monazite structure.

The other interesting part here is the fact that the combination of both vanadate and phosphate can form a multicomponent system called orthovanadatephosphate. This system is mainly achieved by partial replacement of V^{5+} ions by P^{5+} ions (or P^{5+} by V^{5+}) in the $GdVO_4$ (or $GdPO_4$) system. However, by cautiously controlling the annealing temperature and the content of V^{5+} and P^{5+} in the system, gadolinium orthovanadatephosphate (GdV,PO_4) compound usually forms a tetragonal structure [9]. Many reports have demonstrated that this compound is an excellent host for rare earth ions to prepare light emitting materials or phosphors that can be used in different types of light emitting devices.

Very often than not, rare-earths dopant ions are incorporated in either orthophosphate ($LnPO_4$) or orthovanadates ($LnVO_4$) host lattices to prepare phosphors. The two hosts are seldom mixed together to form multicomponents structures of both vanadate and phosphate. Various methods

ranging from wet chemistry to solid state reaction used to prepare lanthanide orthovanadate-phosphate have been reported [10 - 14]. In the current study, we report a straightforward, cost effective and time saving solution combustion process for the preparation of terbium activated gadolinium orthovanadatephosphate ($GdV,P)O_4:Tb^{3+}$) phosphors. These materials have the potential to be used as down-converters in solar cells. In addition, terbium activated gadolinium orthovanadate ($GdVO_4:Tb^{3+}$) and orthophosphate ($GdPO_4:Tb^{3+}$) were also prepared and are discussed.

4.2 Experimental

4.2.1 Synthesis

Gadolinium nitrate hexahydrate ($Gd(NO_3)_3.6H_2O$), ammonium metavanadate (NH_4VO_3), ammonium phosphate ($NH_4H_2PO_4$), terbium nitrate hexahydrate ($Tb(NO_3)_3.6H_2O$) and urea (CH_4N_2O) were used as starting materials. All the chemicals were of analytical grade and were used without further purification.

The $GdV_{1-x}P_xO_4$, (where $x = 0, 0.25, 0.5, 0.75,$ and 1) powder phosphors doped with Tb^{3+} (1 mol %) were prepared by combustion method. The basic principle of combustion method is that once the reaction is initiated at a chosen ignition temperature, a self-sustaining exothermic reaction takes place in a short time interval (approximately 5 minutes). There are many important parameters such as generation of flame, ignition temperature, liberation of gas, background atmosphere, and fuel-oxidant ratio that play an important role in the combustion method. Therefore, in order to ensure reproducibility extreme care must be taken to control these parameters during the synthesis. In a typical preparation, stoichiometric amounts of $Gd(NO_3)_3.6H_2O$, NH_4VO_3, $NH_4H_2PO_4$, $Tb(NO_3)_3.6H_2O$ and urea were dissolved in deionized water. After vigorous stirring, a pale yellow homogeneous solution was obtained. The solution was then transferred into a muffle furnace set at 600 ± 10 ^oC. Due to this high temperature, the

water evaporated and the reagents decomposed and released large amount of gases. The resulting powders were cooled down in air to room temperature and were ground gently using pestle and mortar.

4.2.2 Characterization

For the structure and phase identification, the powder samples prepared were characterized by XRD (Bruker D8 Advanced Powder Diffractometer). The X-ray radiation used during the measurement was a CuKα source (λ= 1.5406 Å). Reflectance spectra were measured using UV-vis spectrophotometer Lambda 950 (PerkinElmer). The photoluminescence (both excitation and emission) data were recorded using a Hitachi F700 fluorescence spectrophotometer. Particle morphology and elemental composition of the materials were analyzed using Jeol JSM-7800F field emission scanning electron microscope (FE-SEM) fitted with Oxford Aztec 350 X-Max80 energy-dispersive X-ray spectroscopy (EDS). The stretching modes of vibration of the samples were analyzed using Nicolet 6700 Fourier transform infrared (FT-IR) spectrometer.

4.3 Results and discussion

4.3.1 Crystal Structure of $GdVO_4$ and $GdPO_4.H_2O$

Figures 4.1 (a) and (b) show the crystal structures of $GdVO_4$ and $GdPO_4.H_2O$, respectively, drawn using the diamond software [15]. These structures were drawn by comparing our measured XRD data with the standard JCPDS standard data, which we requested from the Leibniz Institute for information infrastructure based in Germany. The $GdVO_4$ crystallized in a tetragonal with zircon structure having space group of *I41/amd* (No. 141) [16 - 20]. It has got four molecular units per unit cell and high symmetry [19]. The overall structure of $GdVO_4$ is formed from an alternating edge-sharing tetrahedron groups [VO_4] and bisdisphenoids

[GdO], forming chains parallel to the c-axis [16, 20]. V^{5+} ions in tetrahedron groups $[VO_4]^{-3}$ are arranged with O^{2-} ions tetrahedrally [16, 20] in which a V-O distance is 1.710 Å [16]. Gd^{3+}

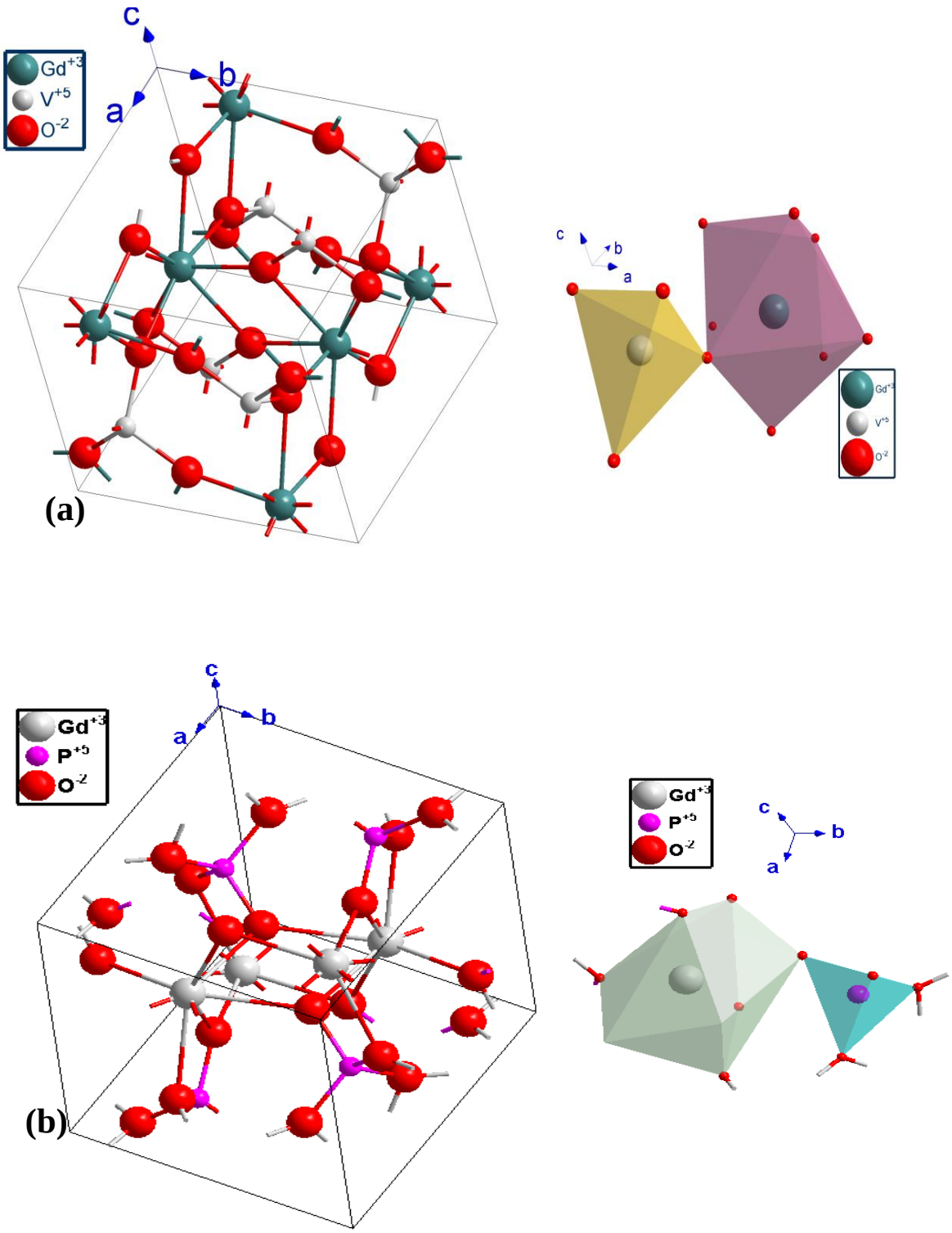

Figure 4.1. *Schematic representation of (a) $GdVO_4$ zircon-type (b) $GdPO_4$ monazite -type crystal structure.*

ions (with point symmetry D_{2d} of Gd^{3+}, without inversion symmetry) are joint within a distorted dodecahedron (eight fold) coordination of eight neighboring O^{2-} ions [16, 20]. The Gd-O bond lengths in the dodecahedra groups [GdO_8] are divided into two sets: 1- four short bonds on the x-y plane with 2.344 Å; and 2- four long distance along z-axis with 2.461 Å [16, 20]. The schematic structure of $GdVO_4$ is shown in figure 4.1(a).

$GdPO_4$ has a monoclinic lower-symmetry in space group *P21/n* (No.14) also known as monazite structure [22 - 26]. The monazite structure can be viewed as a low-symmetry derivative of the zircon structure [25, 26]. The $GdPO_4$ composed of [PO_4] tetrahedra and [GdO_9] polyhedral [20, 22]. In this structure, gadolinium is surrounded by nine atoms of oxygen to form [GdO_9] polyhedrons, and all the Gd-O bond distances are not strictly identical and as a result the GdO_9 polyhedron is highly asymmetric [21, 23, 24]. The schematic structure of $GdPO_4$ is shown in figure 4.1(b).

4.3.2 X-ray diffraction

The XRD patterns of $GdVO_4$ and $GdPO_4{\cdot}H_2O$ powder phosphors are presented in figure 4.2, and they were indexed to tetragonal phases of $GdVO_4$ and $GdPO_4{\cdot}H_2O$ referenced in the standard JCPDS files no 86-0996 and 39-0232 respectively. The lattice strains and crystallite sizes were estimated from the Williamson-Hall equation:

$$\beta \cos\theta = \eta \sin\theta + \frac{0.9\lambda}{D} \qquad 4.1$$

where D is the crystallite size, η is the lattice strain, λ is the wavelength of the x-ray radiation (1.5418Å), β is the full width at half maximum intensity and θ is the diffraction angle at the

peak position. The lattice strain and the crystallites size were found to be 0.025 and 22 nm respectively for $GdVO_4$ whereas for $GdPO_4.H_2O$ were 0.05 and 10 nm respectively.

Figure 4.2(b) shows the XRD patterns of $GdV_{1-x}P_xO_4$: 1:% Tb^{3+} with *x = 0, 0.25, 0.5, 0.75* and *1.0*. The sample with $x = 0$, the XRD spectrum exhibit the trend of $GdVO_4$ (shown in figure 4.2(a)) and the pattern showed a perfect match with the diffraction pattern of the standard tetragonal structure (JCPDS file no. 86-0996), while for $x = 1$, the pattern displays the trend of $GdPO_4.H_2O$ (the same as that shown in figure 4.2(a)) and the powder phosphors was found as hydrate and the diffraction peaks match well with that of standard tetragonal structure for $GdPO_4.H_2O$ (JCPDS file no. 39-0232). It is clear from the XRD spectra that the introduction of Tb^{3+} ions did not affect the main structure of the prepared powder phosphors. This implies that the Tb^{3+} ions (ionic radius ~ 0.092 nm) have successfully substituted the Gd^{3+} ions (ionic radius ~ 0.0938 nm) because they have approximately the same ionic radii.

Furthermore, as the value of x is increased, the XRD peaks slightly shifts from $GdVO_4$ system to $GdPO_4$ system. Similar behavior was also observed by Singh et al and they attributed this to the difference in ionic radii of P^{5+} (~ 0.17Å) and V (~0.35Å) [27]. The XRD pattern of the sample with $x = 0.25$ exhibits the trend of $GdVO_4$ and this is because the molar concentration of vanadium is more than that of phosphorus in this material. On the other hand, the sample with $x = 0.75$ favours that of $GdPO_4$ and this is due to higher concentration of phosphate in the sample. The sample with $x = 0.5$ has diffraction peaks associated with $GdVO_4$ and $GdPO_4$. Thus, it can be concluded that the multicomponent structures of $Gd(VP)O_4$ were successfully prepared.

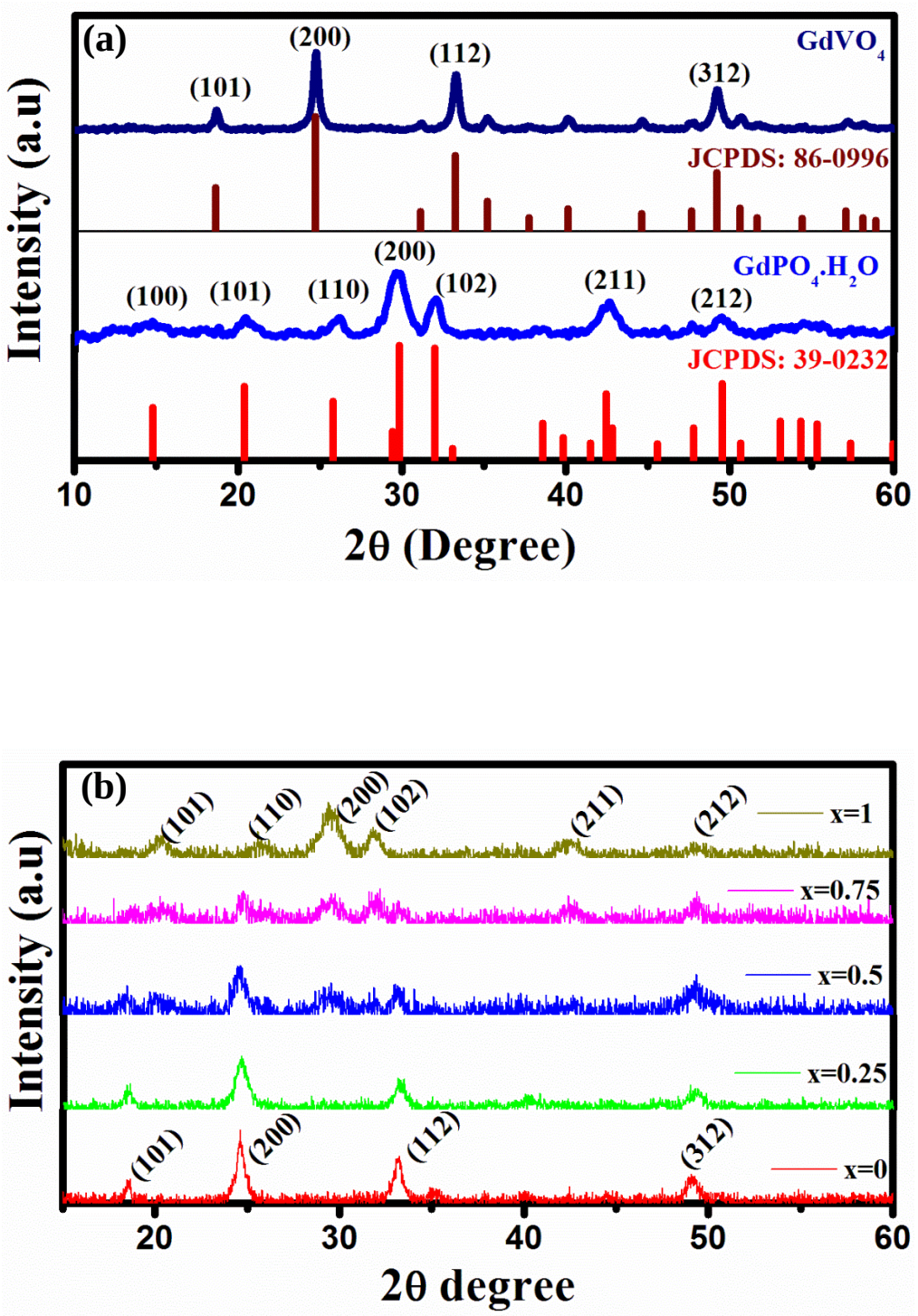

Figure 4.2. *XRD patterns of pure $GdVO_4$ and $GdPO_4.H_2O$ and (b) $GdV_{1-x}P_xO_4$: 1 mol % Tb^{3+} with x=0, 0.25, 0.5, 0.75 and 1.0.*

4.3.3 Scanning electron microscopy

Figure 4.3(a) shows the SEM image of the $GdV_{0.5}P_{0.5}O_4$: 1 mol % Tb^{3+} powder phosphor. This image shows that the powder consisted mainly of agglomerated and spherical particles. Chen attributed agglomeration to high surface energy [28]. When the size of the particles becomes smaller, the surface area increases and this leads to the high surface energy. This can be avoided by employing the capping agents (CAs). If they (CAs) are not used, often the particles try to balance or minimize their surface energy by creating aggregates. On the other hand, at high temperatures, the particles may join together, but after the combustion gases cool below the melting point of the condensed material, the liquid freezes and combination effectively stops. The particles then produce a chain of agglomerates. This agglomeration is a common feature in high-temperature systems which is the case in the present study. Figure 4.3(b) shows the size distribution histogram of $GdV_{0.5}P_{0.5}O_4$: 1 mol % Tb^{3+}. The image-J software was used to determine the particle size distribution for at least 29 particles in sample and the sizes range from 21 nm to 200 nm. The average particle sizes was approximately 48 nm.

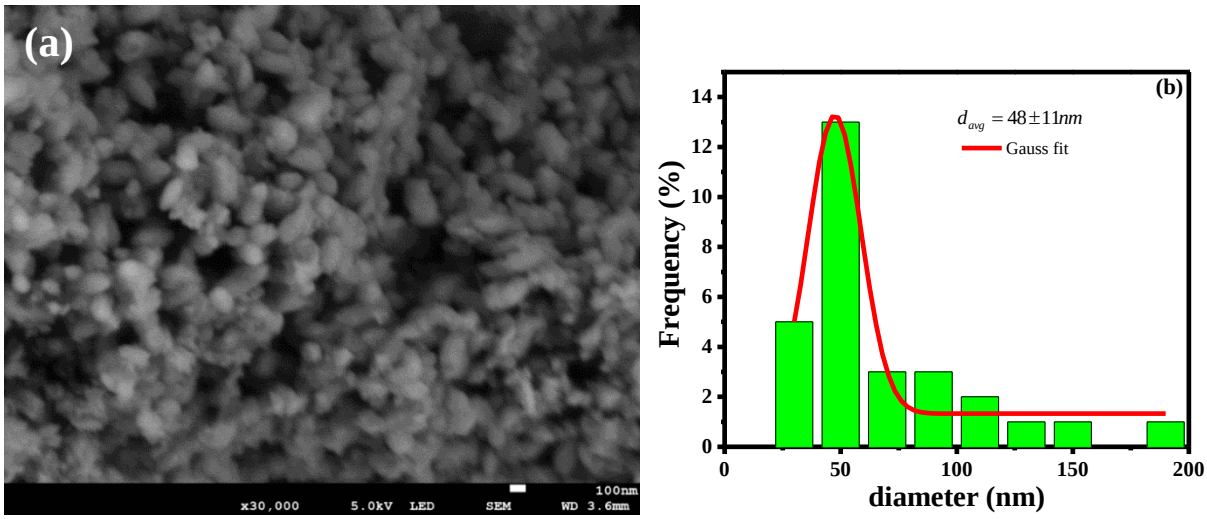

Figure 4.3 *(a) SEM image (b) size distribution histogram of the $GdV_{0.5}P_{0.5}O_4$: 1 mol % Tb^{3+}.*

Energy dispersive x-ray spectroscopy (EDS) confirmed the presence of all the main elements (i.e. Gd, V, P, O and Tb) as shown in figure 4.4. The result further confirms that Tb^{3+} ion has been successfully incorporated into the host lattice as confirmed by the photoluminescence data. The carbon element was also detected by EDS and it is believed to be coming from the carbon tape used for mounting the sample. The inset in figure 4.4 gives the weight percent of all the elements in the as prepared powder phosphors. The concentration of Gd by weight exceeds those of all other elements and the least concentration (also by weight) was recorded from Tb^{3+} as shown in the inset of figure 4.4.

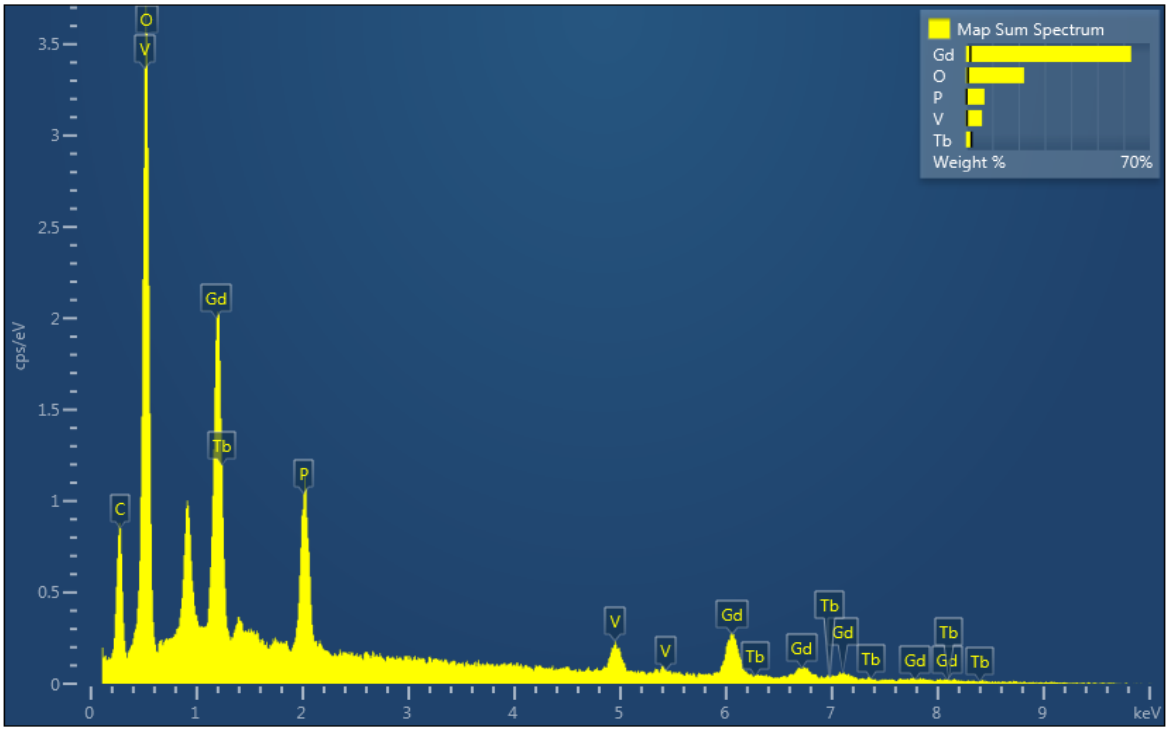

Figure 4.4 *EDS spectrum of the as prepared* $GdV_{0.5}P_{0.5}O_4$*: 1 mol %* Tb^{3+} *powder phosphors.*

4.3.4 Fourier transform infrared (FTIR) analysis

The FT-IR spectrum of the as-prepared $GdV_{0.5}P_{0.5}O_4$: 1 mol. % Tb^{3+} powder phosphor is shown in figure 4.5. The bands located at 551, 629 and 1075 cm^{-1} are attributed to O-P-O bending vibrations. The band centred at 825 cm^{-1} is due to V-O stretching while the bands located at 1380, 1638, 2365 and 3452 cm^{-1} are assigned to the H-O-H stretching vibrations. [29, 30, 31]

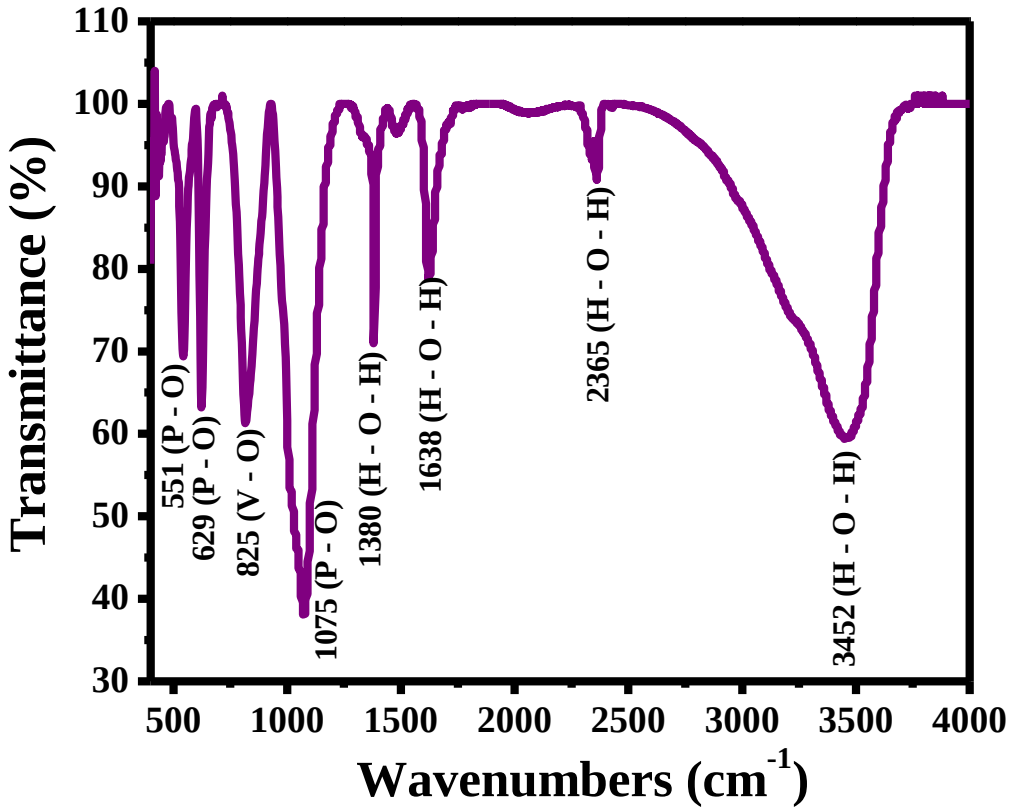

Figure 4.5 *FT-IR spectrum of the as prepared $GdV_{0.5}P_{0.5}O_4$: 1 mol % Tb^{3+} powder phosphors*.

4.3.5 UV-vis Spectroscopy

Figure 4.6 (a) shows the diffuse reflectance spectra of $GdV_{1-x}P_xO_4$: 1 mol % Tb^{3+} (*x=0.25, 0.5, 0.75*) powder phosphors samples. A gentle decrease in the reflectance starts at about 576 nm for all the samples, except for the sample with $x = 1$, due to the absorption. The absorption band in the range between 200 and 350 nm can be ascribed to the absorption of $[(V,P)O_4]^{3-}$ group

[31, 32]. A weak band at about 450 nm is attributed to f→f transitions of Tb^{3+} ions. To evaluate the band gap energy, the transformed Kubelka-Munk reflectance (figure 4.6(b)) was used. The estimated band gap energies are listed in table 4.1. These values are consistent with the once reported by [33]. It is therefore evident from the table that the bad gap energy increases with an increase in P^{5+} molar concentration.

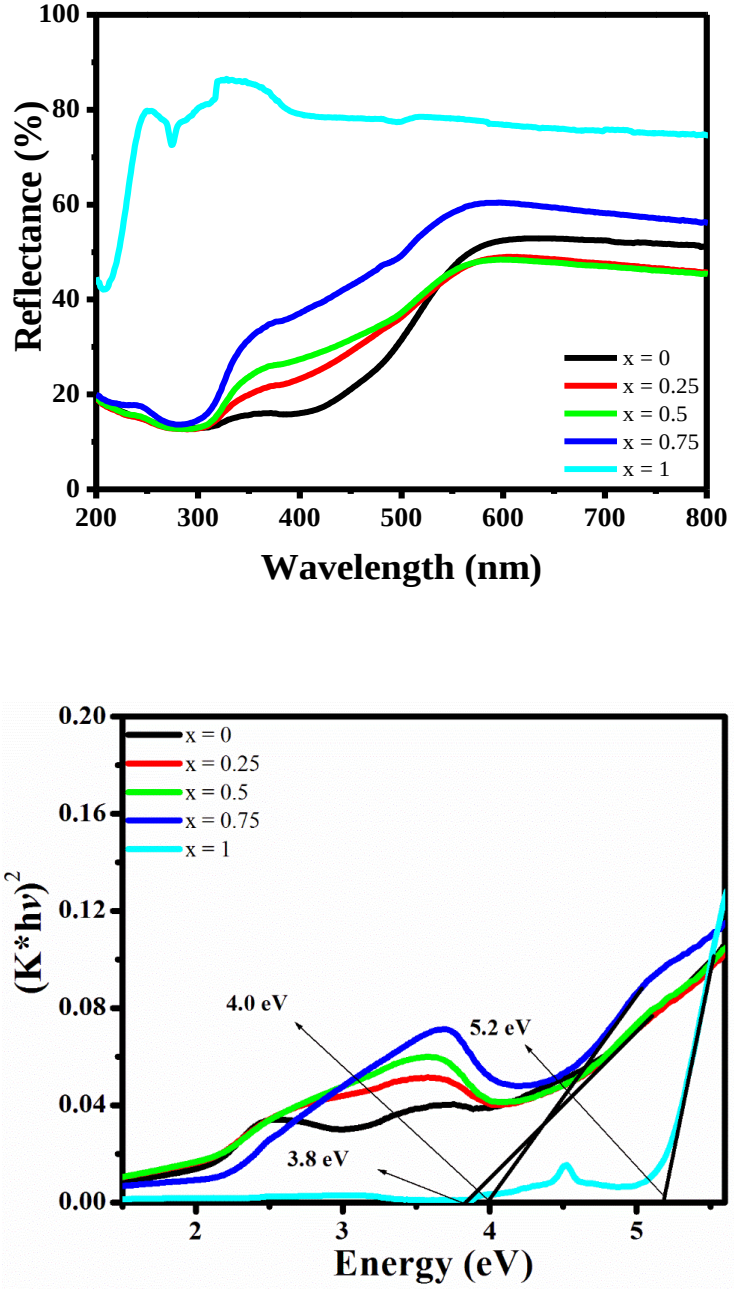

Figure 4.6. *(a) The diffuse reflectance spectra (b) Transformed Kubelka-Munk reflectance of $GdV_{1-x}P_xO_4$: Tb^{3+} with x=0.25, 0.5, 0.75 powder phosphors.*

Table 4.1. *The band gap energies of $GdV_{1-x}P_xO_4$:1mol %Tb^{3+} (x = 0.25, 0.5, 0.75) powder phosphors samples.*

Sample Name	Energy gap (eV)
$GdVO_4$: Tb^{3+}	~ 3.8
$GdV_{0.75}P_{0.25}O_4$: Tb^{3+}	~ 3.8
$GdV_{0.5}P_{0.5}O_4$: Tb^{3+}	~ 3.8
$GdV_{0.25}P_{0.75}O_4$: Tb^{3+}	~ 4.0
$GdPO_4$: Tb^{3+}	~ 5.2

4.3.6 Photoluminescence Spectroscopy

In Figure 4.7 (a) the photoluminescence excitation spectra of $GdV_{1-x}P_xO_4$: 1 mol % Tb^{3+} powder phosphors samples with x = 0, 0.25, 0.5, 0.75 and 1 measured by monitoring the emission wavelength at 545 nm at room temperature are shown. All the samples consist of a strong broad band ranging from 200 to 350nm with a maximum at 250nm; except for the sample with x = 1, which shows a weak band at a relatively longer wavelength (~384nm). The excitation spectrum for the sample with x = 1 shows two distinct relatively narrowband excitation peaks at 218 and 275nm, which protrude from a broad band at 250 nm as observed in the other samples shown in the inset, and the weak excitation bands at 311, 351 and 374nm. The strong broad band at 250nm is attributed to the charge transfer from the oxygen ligands to the central V in the $[V/PO_4]^{3-}$ group (34), whereas the weak band at 384 nm arises from f→f transitions of Tb^{3+} (35,36). The results obtained for x = 1.0 are consistent with the report by Mei et al. (37), who ascribed the peak at ~ 218 nm to the spin allowed f→d transitions of Tb^{3+} ions, while the other band at ~ 275nm is attributed to $^8S_{7/2}\rightarrow{}^6I_j$ transitions of Gd^{3+} ions. The

wavelength range at which the strong broad band extends, suggests that the prepared material may be a good candidate for the absorption of UV radiation or photons.

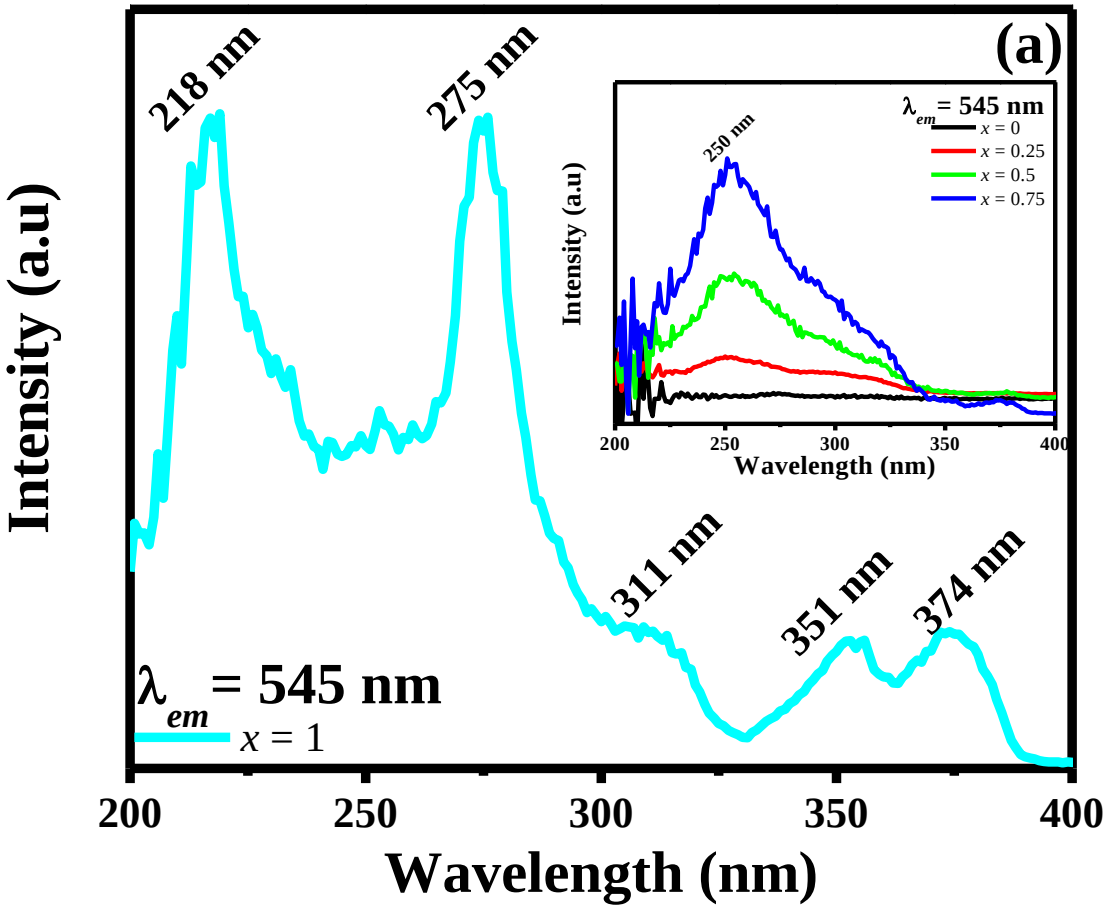

Figure 4.7 *(a). Excitation spectra of $GdV_{1-x}P_xO_4$: 1mol % Tb^{3+} powder phosphors with x=0, 0.25, 0.5, 0.75 and 1.0.*

The photoluminescence emission spectra of $GdV_{1-x}P_xO_4$: 1 mol % Tb^{3+} powder phosphors are shown in figure 4.7(b). All these spectra were obtained by monitoring the excitation wavelength at 275 nm at room temperature. The spectra consist of four emission peaks at 490, 544, 585 and 622 nm and they are attributed to the well-known $^5D_4 \rightarrow {}^7F_j$ (j = 6, 5, 4 and 3) respectively, and these are the characteristics of Tb^{3+} transitions. The peak at 544 nm is the most prominent and it is due to $^5D_4 \rightarrow {}^7F_5$ transitions of Tb^{3+} ion. Due to the fact that photoluminescence excitation and emission intensity of the sample with concentration $x = 1$

has relatively strong intensities compared to other emission spectra from different concentration of *x*, the emission peaks of these other concentrations get suppressed. Therefore, the excitation and emission spectra of the other concentrations (*x* = 0.25, 0.5 and 0.75) other than *x* = 1 were plotted as shown in the inset of figures, 4.7(a) and (b).

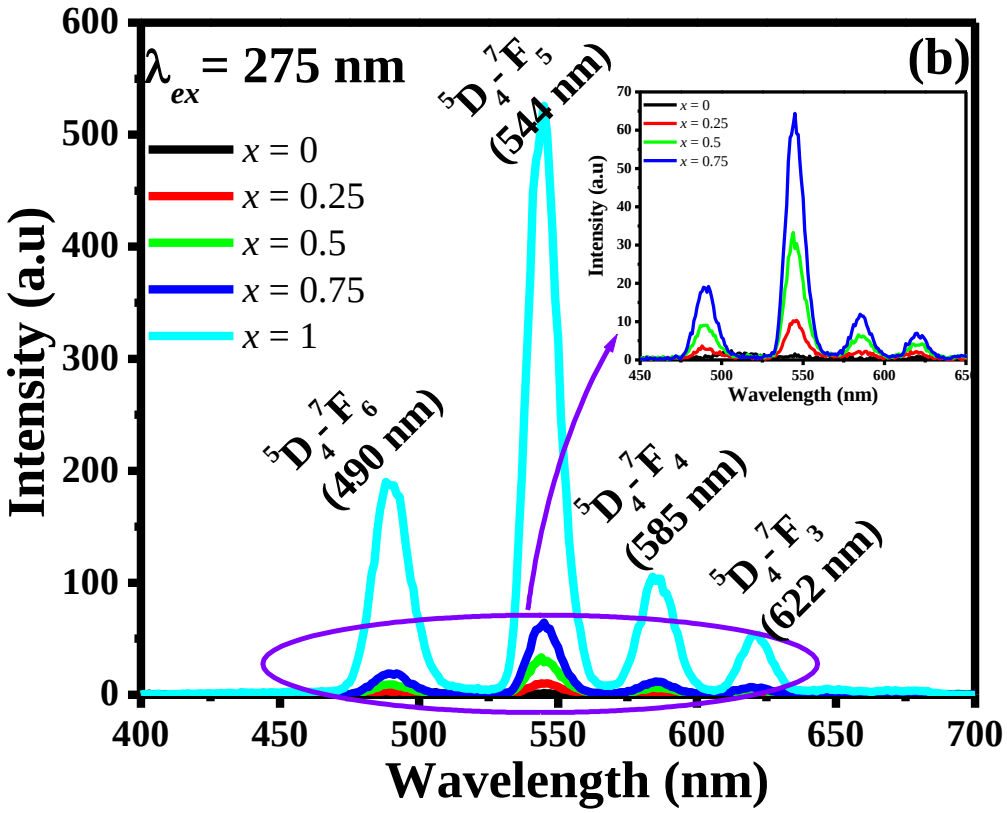

Figure 4.7*(b). Emission spectra of* $GdV_{1-x}P_xO_4$*: 1mol % Tb*$^{3+}$ *powder phosphors with x=0, 0.25, 0.5, 0.75 and 1.0. The PL emission spectrum with x = 1 is excluded in the inset.*

Figure 4.8 represents the intensities of the dominant green emission $^5D_4 \rightarrow {}^7F_5$ of $GdV_{1-x}P_xO_4$: 1 mol % Tb^{3+} as a function of increasing values of *x*. The results showed that the intensity increases with an increase in the value of *x*. For this work, the highest emission intensity is obtained from *x* = 1 and this suggest that the $GdPO_4$ is found to be the perfect matrix for the incorporation of Tb^{3+} ions.

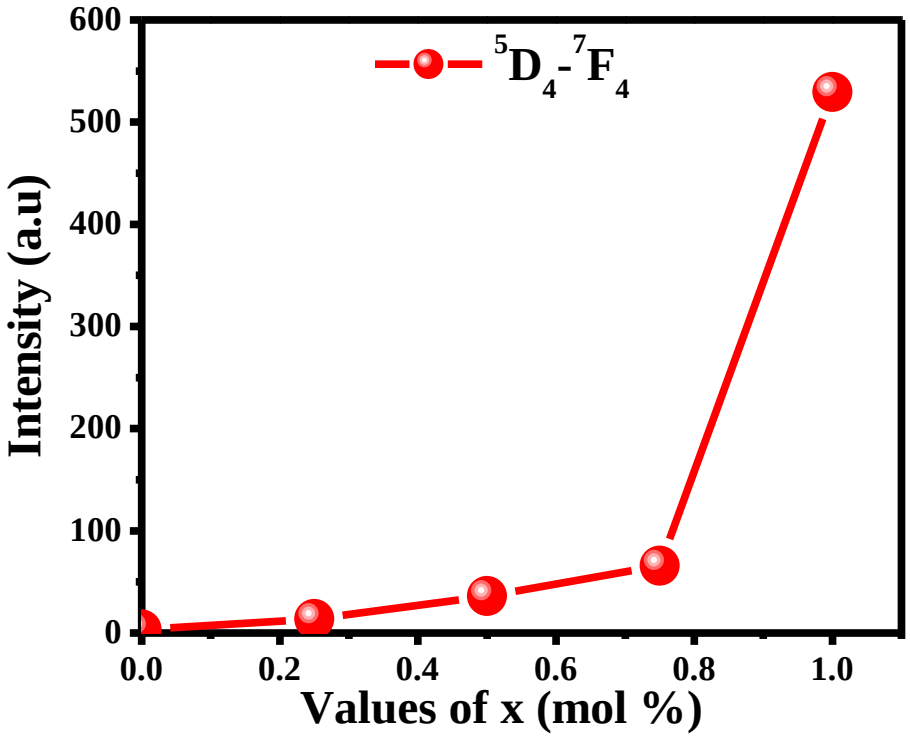

Figure 4.8. *The intensities of the green emission ($^5D_4 \rightarrow {}^7F_5$) of $GdV_{1-x}P_xO_4$:1mol %Tb^{3+} as a function of x values.*

The proposed mechanism for photoluminescence excitation, emission and the energy transfer (ET) from the host (*samples x = 0, 0.25, 0.5 and 0.75*) to the dopant in the as-prepared powder phosphors are illustrated in figure 4.9(a). The excitation and emission process involves three steps. The first step is the absorption of the UV radiation by the host. The energy from the excited carriers/ions/electrons is then transferred to $^5D_3$ state of Tb^{3+} ions followed by non-radiative (NR) process to $^5D_4$. Then the de-excitation process takes place from $^5D_4$ to ^7F_j (j = *3, 4, 5, 6*) and produces green color.

Figure 4.9(b) illustrates a proposed mechanism of the simplified Tb^{3+} energy level diagram (*sample with x = 1*) which shows the photoluminescence excitation and emission transition process. Upon excitation with wavelength of 275 nm, the Tb^{3+} ions are excited and fall into spin allowed ^7D_j (j =*5, 4, 3, 2,1)* and spin forbidden ^9D_j (j = *6, 5, 4, 3, 2*) states respectively. After successive non-radiative relaxation process, the excited ions decay to the emitting state

$^5D_3$ and $^5D_4$. This process is followed by the de-excitation of the excited Tb^{3+} ions and produces green emission.

Usually, with a low doping concentration of Tb^{3+} in the host matrix, the transitions of $^5D_3$ to ^7F_j dominate and produce blue colored emissions. However, if the Tb^{3+} concentration is increased, the cross relaxation from $^5D_3$ to $^5D_4$ occurs due to the interaction between Tb^{3+} ions, which enhances the transitions from $^5D_4$ to ^7F_j with a green emission.[38, 39]

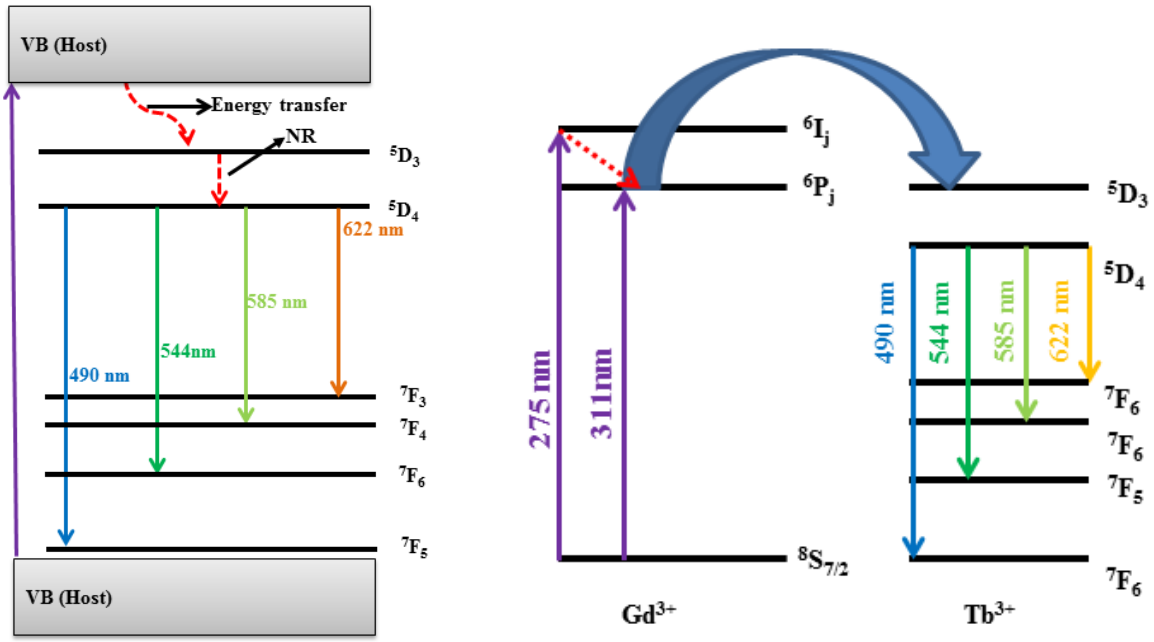

Figure 4.9. *(a) Schematic representation of energy level diagram and proposed energy transfer mechanism (b) Schematic representation of Tb^{3+} energy level diagram and proposed mechanism.*

The photoluminescence decay curves of $GdV_{1-x}P_xO_4$ activated by 1 mol % Tb^{3+} that compares the decay time when the value of *x* is increased are presented in figure 10. The decay curves were recorded when the samples were excited at 275 nm. The spectra show a similar trend

with rapid decay at first and then followed by the slower one. To find the average life time, each spectrum was fitted with the double exponential decay:

$$I = A_1 \exp(\frac{-t}{\tau_1}) + A_2 \exp(\frac{-t}{\tau_2}) \qquad 4.2$$

where I is the decay intensity, A_1 and A_2 are constants, τ_1 and τ_2 are rapid and slow lifetimes respectively and t is the time. The double exponential fit was used because the decay curve is composed of two components, namely, the rapid component at first (i.e from 0 to 50 ms) and a slow component from 50 ms to the end. The fast decay component is attributed to non-radiative recombination that involves an enhanced multiphonon decay of localized exciton states, while the slow component is attributed to the radiative decay of these localized exciton states [40,41]. In addition, Dutta et al [42] attributed multi-exponential decay to factors such as the difference in non-radiative probability for lanthanides ions at or near surface and those at the core of particles, inhomogeneous distribution of the doping ions in the host materials, and the transfer of excitation energy from the donor to lanthanides activators. The average lifetimes for each sample were calculated from equation (3) and are presented in table 2. These values are dependent on the values of x, with the highest value recorded when x = 0.25.

$$\langle \tau \rangle = \frac{A_1 \tau_1^2 + A_2 \tau_2^2}{A_1 \tau_1 + A_2 \tau_2} \qquad 4.3$$

where $\langle \tau \rangle$ is the average life time.

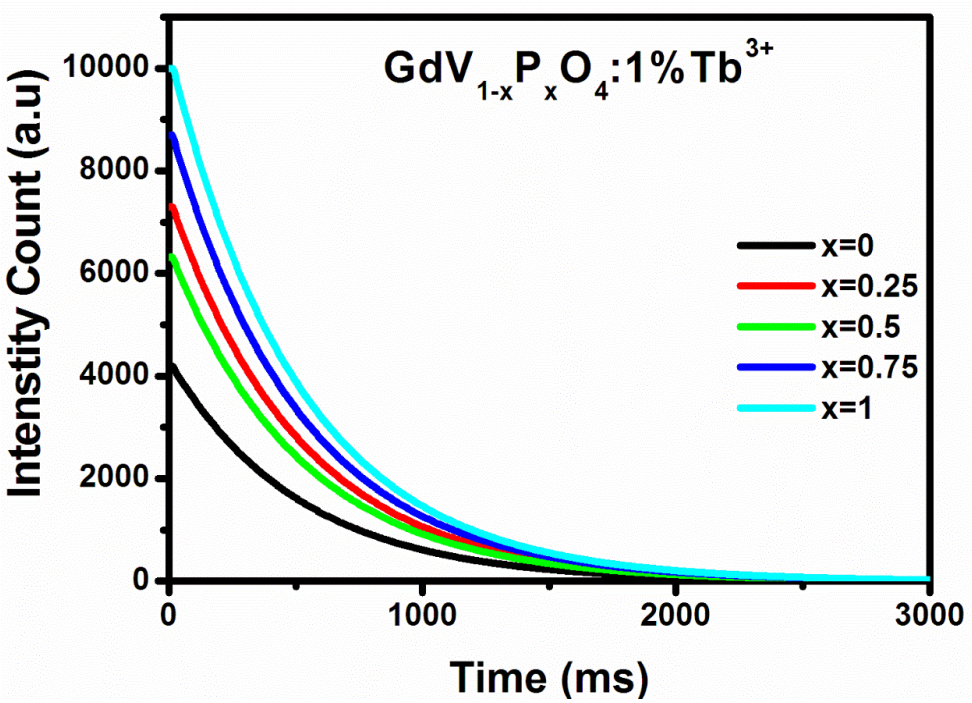

Figure 4.10 *Decay curves of $GdV_{1-x}P_xO_4$:1mol %Tb^{3+} (x = 0, 0.25, 0.5, 0.75 and 1) powder phosphors.*

Table 4.2 *A table showing the average lifetimes of $GdV_{1-x}P_xO_4$:1%Tb^{3+} (x = 0, 0.25, 0.5, 0.75 and 1) powder phosphors.*

Sample	$\langle\tau\rangle$ (s)
$GdVO_4$:1 mol% Tb^{3+}	0.408
$GdV_{0.75}P_{0.25}O_4$:1 mol% Tb^{3+}	0.429
$GdV_{0.5}P_{0.5}O_4$:1 mol% Tb^{3+}	0.457
$GdV_{0.25}P_{0.75}O_4$:1 mol% Tb^{3+}	0.477
$GdPO_4$:1 mol% Tb^{3+}	0.441

4.4 Conclusion

$GdV_{1-x}P_xO_4$: 1 mol % Tb^{3+} was successfully synthesized using solution combustion method. The XRD data showed that the prepared powder has a tetragonal structure for the sample with $x = 0$ and x = 1. Furthermore, the XRD peaks of $GdV_{0.5}P_{0.5}O_4$: 1 mol %Tb^{3+} are intermediate between that of $GdVO_4$ and $GdPO_4.H_2O$ indicating that the phosphate ions were successfully incorporated into $GdVO_4$ matrix. Our UV-Vis and PL emission data indicate that our materials absorbed UV radiation and re-emit in the visible region. That is, the primary excitation energy was absorbed by the host in the UV region and transferred to Tb^{3+} luminescent centre resulting in an enhanced green emission. Both the PL intensity and decay times were shown to be dependent on the values of *x* with the greatest PL intensity recorded from the sample with $x = 1$ while the greatest average decay time was recorded from the sample with $x = 0.25$

4.5 Reference

1. Romankov S, Komarov SV, Nahashi S, Ueno S, Kaloshkin S, Kasai E, *Surf Coat Tech.* 202 (2008) 4285–4290.

2. Yan Y,Wang J, HojamberdievM, Lu Z, Ren B, *J Alloy Compd*. 597 (2014) 282–290.

3. Zhiqiang Z, Li G, Peiyun J, *Rare Metal Mat Eng*. 43 (2014) 1588–1593.

4. Nawapong C, Kittiwichanaa S, Thongtema T, Thongtemb S, Kaowphonga S, *Ceram Int.* 40 (2014) 16337–16342.

5. Davis JB, Hay RS, Marshall DB, Morgan PED, Savir A, *J Eur Ceram Soc*. 20 (2000) 583–587.

6. Riwotzki K, Heysammy H, Schnablegger H, Kornowski A, Haase M, *J Luminesc.* 156 (2014) 91–96.

7. Nishihama S, Hirai T, Komasawa I, *J Mater Chem*. 12 (2002)1053–1057.

8. Li J, Xu X, Fan Y, Li Y, Hu L, Tang C. *Mater Chem Phys.* 124 (2010) 1172–1176.

9. Yan B, Su X, *J Alloy Compd* 431 (2007) 342–347.

10. Park K, Kim KY, Shinde KN, *Mater Chem Phys*. 138 (2013) 204–208.

11. Jin Y, Li C, Xu Z, Cheng Z, Wang W, Li G, *Mater Chem Phys.* 129 (2011) 418–423.

12. Su X-Q, Yan B, *Mater Chem Phys*. 93 (2005) 552–556.

13. YuM, Lin J, Zhou YH, PangML, Han XM,Wang SB, *Thin Solid Films*. 444 (2003)245–253.

14. Qings X, Bing Y, *Mater Chem Phys.* 93 (2005) 552–556.

15. Prasannakumar JB, Vidya YS, Anantharaju KS, Prabhakara KR, Nagaswarupa HP. *spectrochemica Acta – Part A:Molecular and Biomolecular Spectroscopy*. 151 (2015) 131–140.

16. http://shodhganga.inflibnet.ac.in/bitstream/10603/9272/7/07_chapter %203.pdf (*accessed on 16 August 2015*).

17. Reshak AH, Azam S, *Int J Electrochem Sci.* 8 (2013) 10396–10423.

18. Wierzbicka E, Malinowska A, Wieteska K, Wierzchowski, Lefeld-Sosnowska M, Swirkowicz M, *Acta Phys Pol A.* 121 (2012) 906–909.

19. Cook DC, Cashion JD, *J Phys C Solid State Phys*. 12 (1979) 605–613.

20. Gavrilović TV, Jovanovic DJ, Lojpur V, Dramicanin MD, DOI: 10.1038/srep04209.

21. http://shodhganga.inflibnet.ac.in:8080/jspui/bitstream/10603/9257/7/ 07_chapter%203.pdf (*accessed 16 August 2015*).

22. Lacomba-Perales R, Errandonea D, Meng Y, Bettinelli M, DOI: 10.1103/*Phys Rev B.* 81.064113.

23. Bregiroux D, Fabienne A, Thibault C, Dimitri S, Didier BA, *Solid State Sci*. 9 (2007):432–439.

24. Wu CC, Chen KB, Lee CS, Chen TM, Cheng BM, *Chem. Mater*. 16 (2007) 3278–3285.

25. Bregiroux D, Champion E, Audubert F, Assollant DB, *J Eur Ceram Soc*. 26 (2006) 279–287.

26. Evangelisti M, Sorop TG, Bakharev ON, Visser D, Hillier AD, Alonso JJ, DOI: 10.1103/ *Phys. Rev B*. 84.094408.

27. Singh SN, Sahu NK, Bahadur D, *J Mater Chem C*. 248 (2014) 248–255.

28. Qijun C, Dong Y, Kang M, Zhang P, *J Luminesc*. 156 (2014) 91–96.

29. Song H, Zhou L, Li L, Hong F, Luo X, *Mater Res Bull.* 48 (2013) 5013–5018.

30. Fan Y, Hu Z, Yang J, Zhang C, Zhu L, *Appl Surf Sci.* 266 (2013) 22–26.

31. Jovanovic DJ, Antic Z, Krsmanovic RM, Metric M, Dordevic V, Bartova B, *Opt Mater*. 35 (2013)1797–1804.

32. Zahedifar M, Chamanzaadeh Z, Mashkani SMH, *J Luminesc.* 135 (2013) 66–73.

33. Yang L, Li L, Zhao M, Li G, *Phys. Chem. Chem. Phys.* 14 (2012) 9956–9965.

34. Wang L, Chen L, *Mater*. *Charact.* 69 (2012) 108–114.

35. Pavitra A, Raju GSR, Ko YH, Yu JS, *Phys.Chem. Chem. Phys*. 14 (2012) 11296–11307.

36. Ganngam P, Ningthoujam RS, Singh WR, Loitongbam RS, Singh NS, Rath A, *Dalton Trans*. 40 (2011)11571–11580.

37. Mei Y, You H, Huang Y, Jia G, Song Y, Guo N, *Cryst. Eng. Commun*. 12 (2010) 2865–2870.

38. Kore BP, Dhoble NS, Dhoble SJ, *Radiat. Meas.* 67 (2014) 35–46.

39. Sekita M, Miyazawa Y, Morita S, Sekiwa H, Sato Y, *Appl Phys Lett*. 65 (1994) 2380–2382.

40. Klann R, Brandt O, Yang H, Grahn HT, Ploog KH. Recombination dynamics of near-band edge emission in cubic GaN in Ultrafast process in spectroscopy. Editors: Svelto O, De Silvestri S, Denardo G editors. Ultrafast processes in spectroscopy. Springer: New York, (1996) 259–63.

41. Gokus T, Cornet L, Duque JG, Pasquali M, Hartschuh A, Lounis B, *J Phys Chem C*. 114 (2010) 14025–14028.

42. Dutta T, Som S, Sharma SK, *RCS Adv*. 5 (2015) 7380–7387.

CHAPTER 5 Dual emission from Sm^{3+} and Tm^{3+} activated gadolinium phosphovanadate

ICCBN2015 Proceedings, 617—633

5.1. Introduction

Rare earth orthovanadates and orthophosphates with general formula RMO_4, where R = Sc, Y, La, Gd or Lu and M = V or P, are important host for rare-earths (lanthanides) ions [1] to prepare light emitting materials or phosphors. Among this orthovanadates or orthophosphates, gadolinium orthovanadates ($GdVO_4$) and orthophosphate ($GdPO_4$) have been extensively studied due to their excellent chemical stability, high thermal conductivity and high index of refraction [2]. $GdVO_4$ crystallizes in a tetragonal with zircon structure having space group of *I41/amd* (No. 141) [3-6] while $GdPO_4$ has a monoclinic lower-symmetry in space group *P21/n* (No.14) which is also called monazite structure [7-11]. The combination of both vanadate and phosphate can form a multicomponent system called orthovanadatephosphate or phosphovanadate $[VO_4]^{3-}$ [12- 16]. Depending on the molar ratio of vanadium (V^{5+}) to phosphorus (P^{5+}) in the system and annealing temperature, gadolinium phosphovanadate can crystallize in a tetragonal structure and become an excellent host for rare earth ions [17].

Many researchers have demonstrated that preparation of gadolinium phosphovanadate with specific molar concentration ratio of vanadium to phosphorus improves the photoluminescence emission intensity [2] of the dopant ions. Depending on the choice of the dopant, the emission of gadolinium phosphovanadate phosphor can be tuned such that a single emission is observed [15]. On the other hand, in a dual- or multi-emission, the phosphor usually contains more than one dopant material or a single dopant at its multiple oxidation states [18]. The incorporation of more than one dopant ions may lead to emission intensity enhancement due to energy transfer from one of the ions to the other, in which case only a single emission will be observed. One other possibility might be the reduction in the emission intensity, in which case dual-

emission will be observed. Depending on the desired application, the photoluminescence emission of these phosphors can be tuned to produce either single or dual-emission.

In this study, Sm^{3+}/Tm^{3+} single doped and Sm^{3+}-Tm^{3+} co-doped gadolinium phosphovanadate were synthesized by solution combustion process with the aim of finding the optimal molar concentration ratio of the dopants (i.e. Sm^{3+} and Tm^{3+}) for the production of dual-emission to explore its potential application as down-converters in dye-sensitized solar cells or DSSCs. The solution combustion method of preparation was chosen because of, among other things, ability to produce high purity materials with better homogeneity, and it is also cost effective and time saving.

5.2. Experimental

5.2.1 Synthesis

The multi-component systems of samarium and thulium doped gadolinium phosphovanadate ($GdV_{0.5}P_{0.5}O_4$: Sm^{3+}, Tm^{3+}) were synthesized by solution combustion method. The starting materials: AR grade 99.99% gadolinium (III) nitrate hexahydrate ($Gd(NO_3)_3.6H_2O$), ammonium metavanadate (NH_4VO_3), ammonium phosphate ($NH_4H_2PO_4$), urea (CH_4N_2O), samarium nitrate hexahydrate ($Sm(NO_3)_3.6H_2O$) and thulium nitrate hexahydrate ($Tm(NO_3)_3.6H_2O$) were dissolved together in de-ionized water in appropriate weights to form the necessary precursor solutions. The mixtures were stirred vigorously at a temperature of ~ 70 ^oC for 30 min using magnetic stirrer until homogeneous yellowish solutions were formed. The solutions were then transferred into different crucibles, that were subsequently transferred into a furnace preheated to the temperature of 600 ± 10 ^oC. As a result of exothermic reaction that took place, the final products were fluffy ashes. The resulting combustion ashes were allowed to cool down in air to room temperature and were manually ground gently using pestle

and mortar to obtain a fine powder. The synthesized powders were annealed at 900ºC for 2 hours in air.

5.2.2 Characterization

The structure and phase identification, of the powder samples were characterized by XRD (Siemens D5000 powder Diffractometer). The X-ray radiation used during the measurement was a CuKα source (λ= 1.5406 Å). Reflectance spectra were obtained by using UV-Vis spectrophotometer Lambda 950 (PerkinElmer). The photoluminescence (both excitation and emission) data were recorded using a Hitachi F700 fluorescence spectrophotometer. The morphology and elemental composition of the materials were obtained using Jeol JSM-7800F field emission scanning electron microscope (FE-SEM) fitted with Oxford Aztec 350 X-Max80 energy-dispersive X-ray spectroscopy (EDS).

.

5.3. Results and discussion

5.3.1 X-Ray diffraction

The phase structure, purity and crystallinity of the prepared powder phosphors were investigated by XRD. Figure 5.1 shows the XRD pattern of $GdV_{0.5}P_{0.5}O_4$: Sm^{3+}, Tm^{3+} powder phosphors annealed at 900ºC for 2 hours. The XRD results indicate that the powder phosphor is well crystalline and the diffraction peaks were found to be consistent with the tetragonal structure known from bulk gadolinium vanadate referenced in JCPDS 72-0277. These results are in good agreement with the data reported by Park et al [2]. The XRD pattern further revealed that all the peaks are slightly shifted towards the higher 2θ angles. This behavior is probably due to strains caused by the difference in ionic radii of vanadium (~ 0.54 Å) and phosphorus (~ 0.35 Å) [19]. The diffraction peaks marked with * at 2θ = 27.74º and 29.63º were indexed at (200) and (120) peaks of $GdPO_4$ [20].

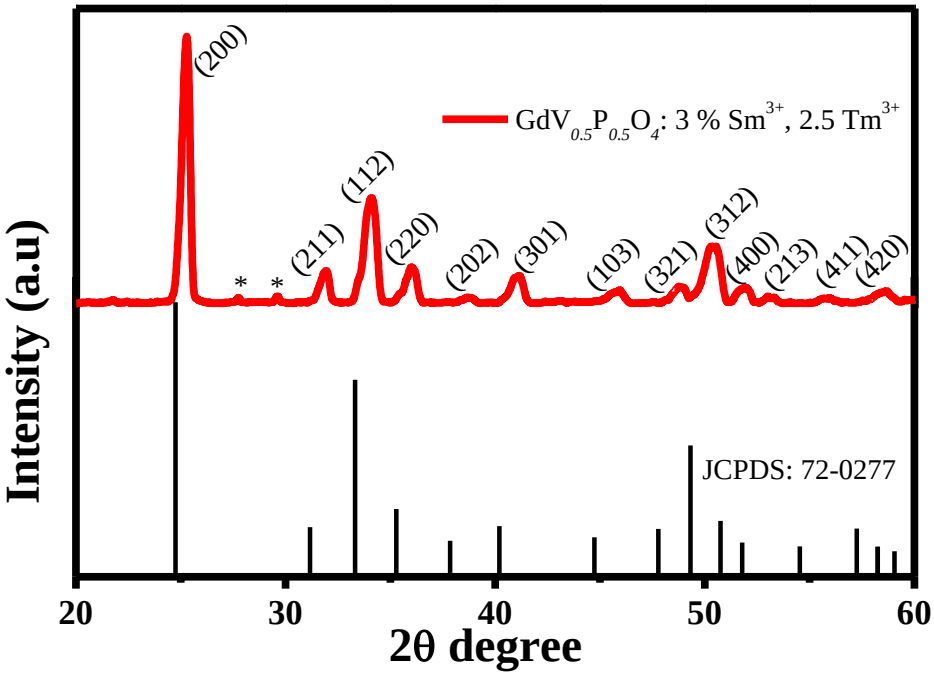

Figure 5.1. *XRD patterns of $GdV_{0.5}P_{0.5}O_4$: 3 mol % Sm^{3+}, 2.5 mol % Tm^{3+}.*

It should also be noted that the XRD peaks are broadened and this is an indication that the prepared phosphor material has small crystallite size. Both the lattice strain and the crystallite sizes were estimated from equation 4.1. The estimated lattice strain and crystallite size were found to be 0.009 and 20 nm respectively.

5.3.2 Scanning electron microscopy

The scanning electron microscopy (SEM) was used to investigate the surface morphology of the prepared samples. Typical SEM images of the selected $GdV_{0.5}P_{0.5}O_4$: Sm^{3+}, $GdV_{0.5}P_{0.5}O_4$: Tm^{3+} and $GdV_{0.5}P_{0.5}O_4$: Sm^{3+}, Tm^{3+} are shown in figure 5.2(a-c). The prepared phosphor powders showed different particle sizes and shapes. These shapes include among others, three dimension tetragonal, hexagonal and spherical particles with less agglomeration.

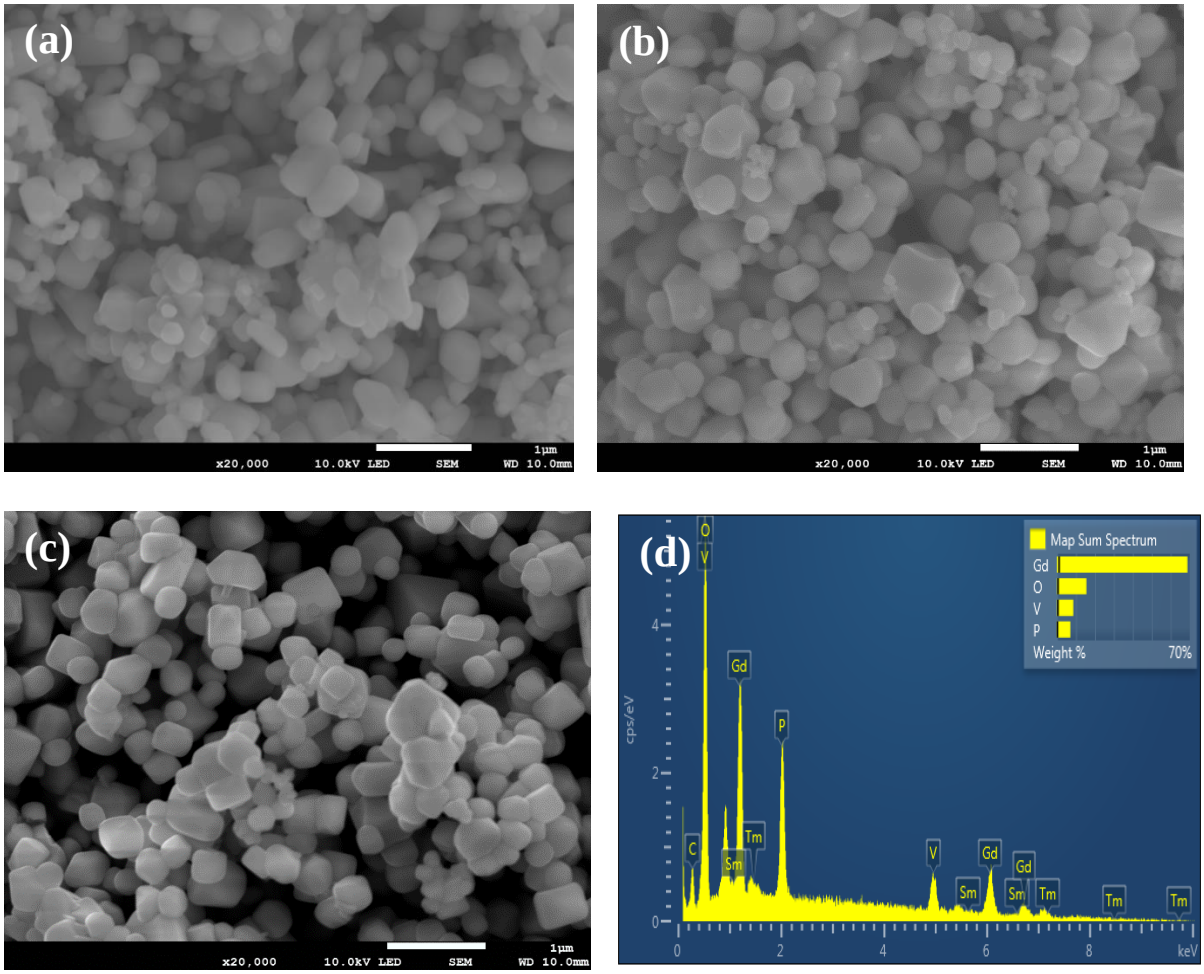

Figure 5.2. *SEM images of (a) $GdV_{0.5}P_{0.5}O_4$: Sm^{3+} (b) $GdV_{0.5}P_{0.5}O_4$: Tm^{3+} (c) $GdV_{0.5}P_{0.5}O_4$: Sm^{3+}, Tm^{3+} and (d) EDS spectrum of 3 mol % Sm^{3+}, 2.5 mol % Tm^{3+}.*

Energy dispersive x-ray spectroscopy (EDS) confirmed the presence of all the main elements (i.e. Gd, V, P, O, Sm and Tm) as shown in figure 5.2(d). The results further confirm that Sm^{3+} and Tm^{3+} ions have been successfully incorporated into the host lattice as confirmed further by photoluminescence spectroscopy data. The small percentage of carbon element was also detected by EDS and it is due to the carbon tape used for mounting the sample. The inset of figure 5.2(d) gives the weight percent of all the elements in the as prepared powder phosphor. The concentration of Gd is approximately 69 % and O_2 is about 16 %. Phosphorus and vanadium have about 8 and 6 % respectively.

5.3.3 UV-Vis spectroscopy

The optical absorption properties of the prepared phosphor powders were investigated by using UV-Vis diffuse reflectance spectroscopy. Figure 5.3(a) shows the room temperature UV-Vis diffuse reflectance spectra of the selected singly doped $GdV_{0.5}P_{0.5}O_4$: Sm^{3+}, $GdV_{0.5}P_{0.5}O_4$: Tm^{3+} and doubly doped $GdV_{0.5}P_{0.5}O_4$: Sm^{3+}, Tm^{3+} samples annealed at 900ºC for 2 hours. The spectra show a strong broad absorption band ranging from 200 to 450 nm with the maximum at ~ 340 nm. This broad band is ascribed to charge transfer from the O legands to the central (V,P) atom inside $(V,P)O_4^{3+}$ ions [21]. To evaluate the band gap energy, the transformed Kubelka-Munk reflectance (figure 5.3(b)) was used. The estimated band gap energies were found to be 2.20 eV for singly doped (Sm^{3+} and Tm^{3+}) and for doubly doped (Sm^{3+}, Tm^{3+}) it was 2.10 eV.

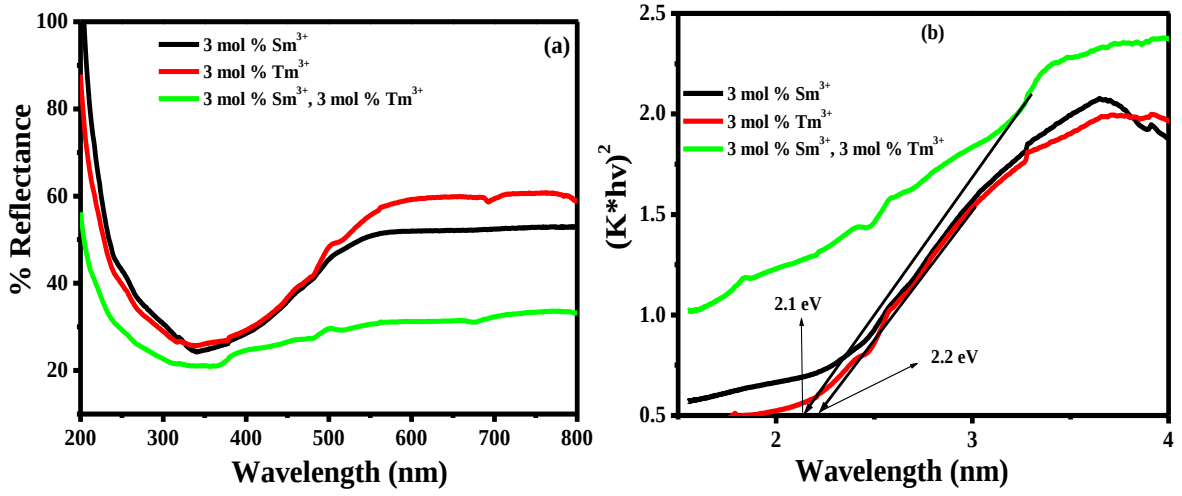

Figure 5.3. *(a) UV-Vis reflectance spectra and (b) Transformed Kubelka-Munk plot of* $GdV_{0.5}P_{0.5}O_4$: Sm^{3+}, $GdV_{0.5}P_{0.5}O_4$: Tm^{3+} *and* $GdV_{0.5}P_{0.5}O_4$: Sm^{3+}, Tm^{3+}.

5.3.4 Photoluminescence spectroscopy

Figure 5.4(a) exhibit the excitation spectra of $GdV_{0.5}P_{0.5}O_4$: *x* mol % Tm^{3+} phosphor powder samples obtained by monitoring the emission wavelength at 477 nm. The spectra show two overlapping bands. The first band range from 200 to 250 nm and is attributed to host absorption band while the other peak between 250 to 350 nm is attributed to charge transfer from oxygen ligands to the central vanadium, phosphorus atom(s) inside (V, P) O_4^{3-} ion(s) [15]. Figure 5.4(b) shows the photoluminescence emission spectra of $GdV_{0.5}P_{0.5}O_4$: *x* mol % Tm^{3+} phosphor powder samples obtained by monitoring the excitation wavelength at 275 nm. The prominent blue emission peak centered at ~ 477 nm and a weak red emission peak were observed and they are ascribed to $^1G_4 - {}^3H_6$ and $^1G_4 - {}^3F_4$ transitions of Tm^{3+} ion respectively [22].

The excitation spectra of $GdV_{0.5}P_{0.5}O_4$: *x* mol % Sm^{3+} measured at the emission wavelength of 603 nm are shown in figure 5.5(a). The spectra exhibit the strong broad band positioned in the wavelength region between 200 and 350 nm with the maximum at 268 nm, which is ascribed to the VO_4^{3-} group and it is in good agreement with the results reported by Yan et al [23]

The emission spectra (figure 5.5(b)) were measured at an excitation wavelength of 275 nm. All the powder samples display similar trend except for the intensity, with the highest when $x = 3$. The emission peaks from the transitions of Sm^{3+} were observed and these peaks were 567 nm ($^6G_{5/2} — {}^6H_{5/2}$), 604 nm ($^6G_{5/2} — {}^6H_{7/2}$) and 650 nm ($^6G_{5/2} — {}^6H_{9/2}$) respectively. The most intense emission peak was observed at the wavelength of 603 nm.

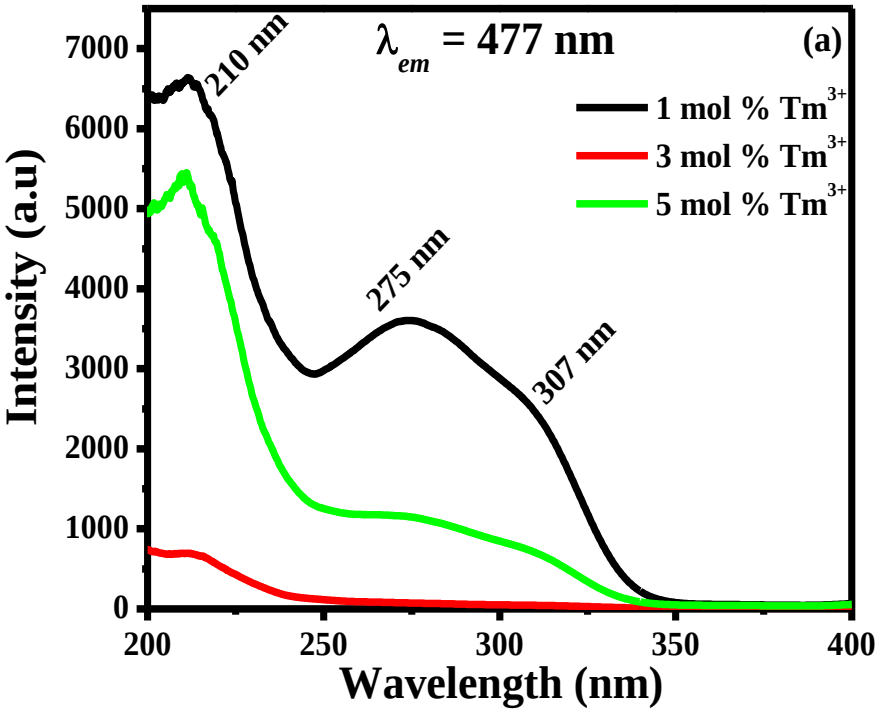

Figure 5.4. *(a) Excitation spectra of $GdV_{0.5}P_{0.5}O_4$: x mol % Tm^{3+}.*

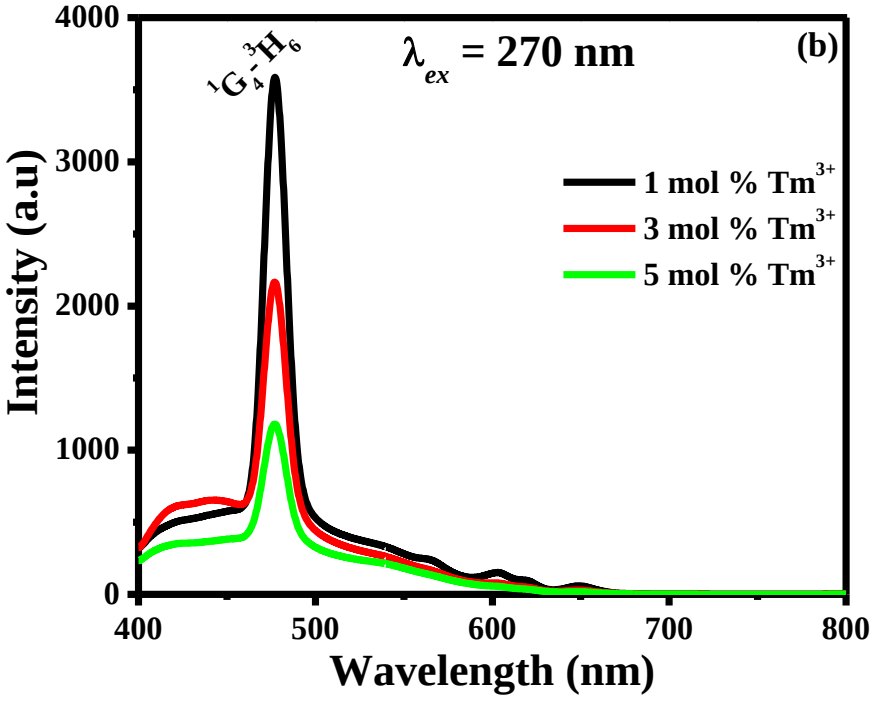

Figure 5.4. *(b) Emission spectra of $GdV_{0.5}P_{0.5}O_4$: x mol % Tm^{3+}.*

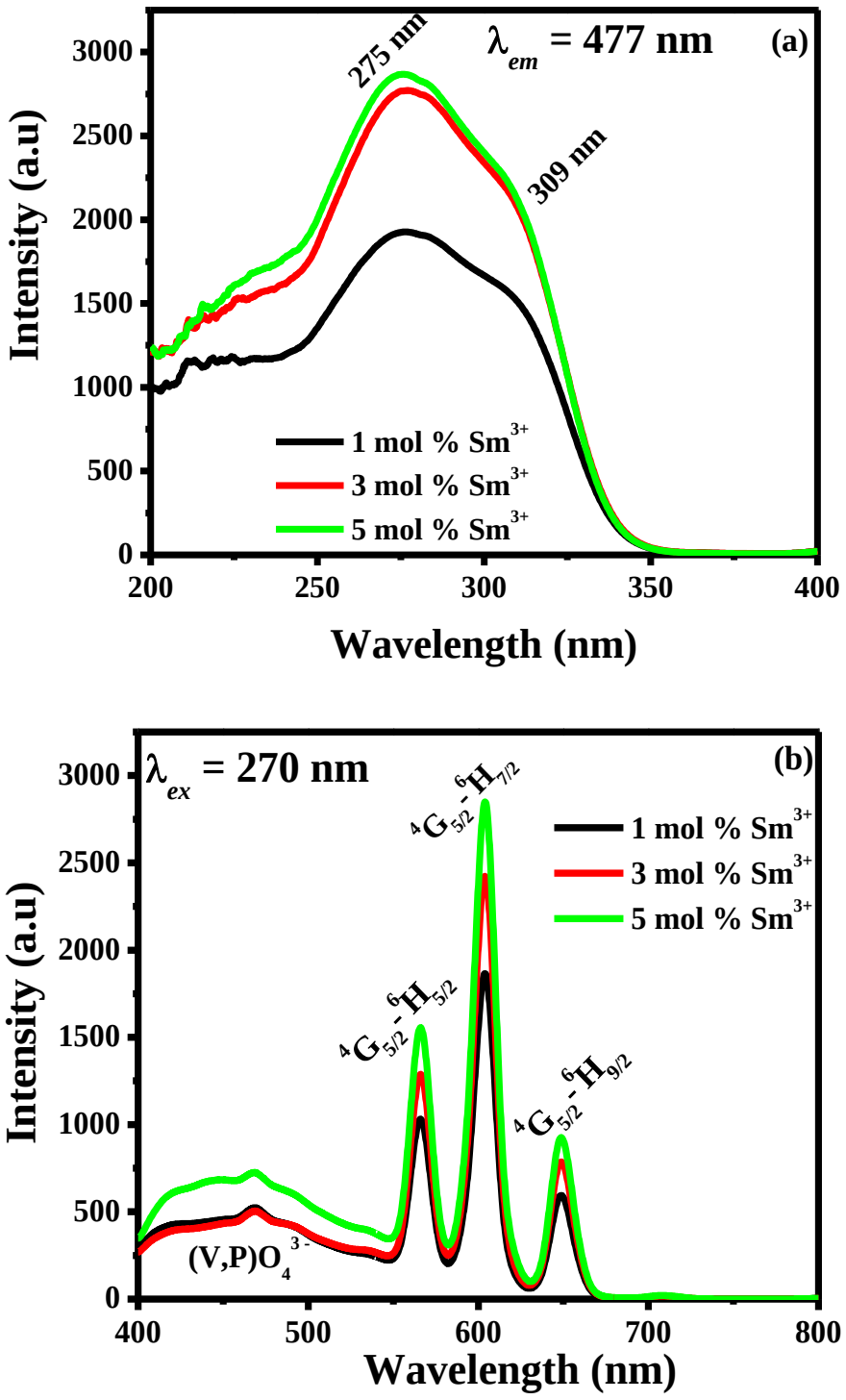

Figure 5.5. *(a) Excitation and (b) Emission spectra of $GdV_{0.5}P_{0.5}O_4$: x mol % Sm^{3+}.*

Figure 5.6(a) shows the excitation spectra of the Sm^{3+} and Tm^{3+} co-doped $GdV_{0.5}P_{0.5}O_4$ phosphor powder samples obtained by monitoring emission wavelength at 603 nm.

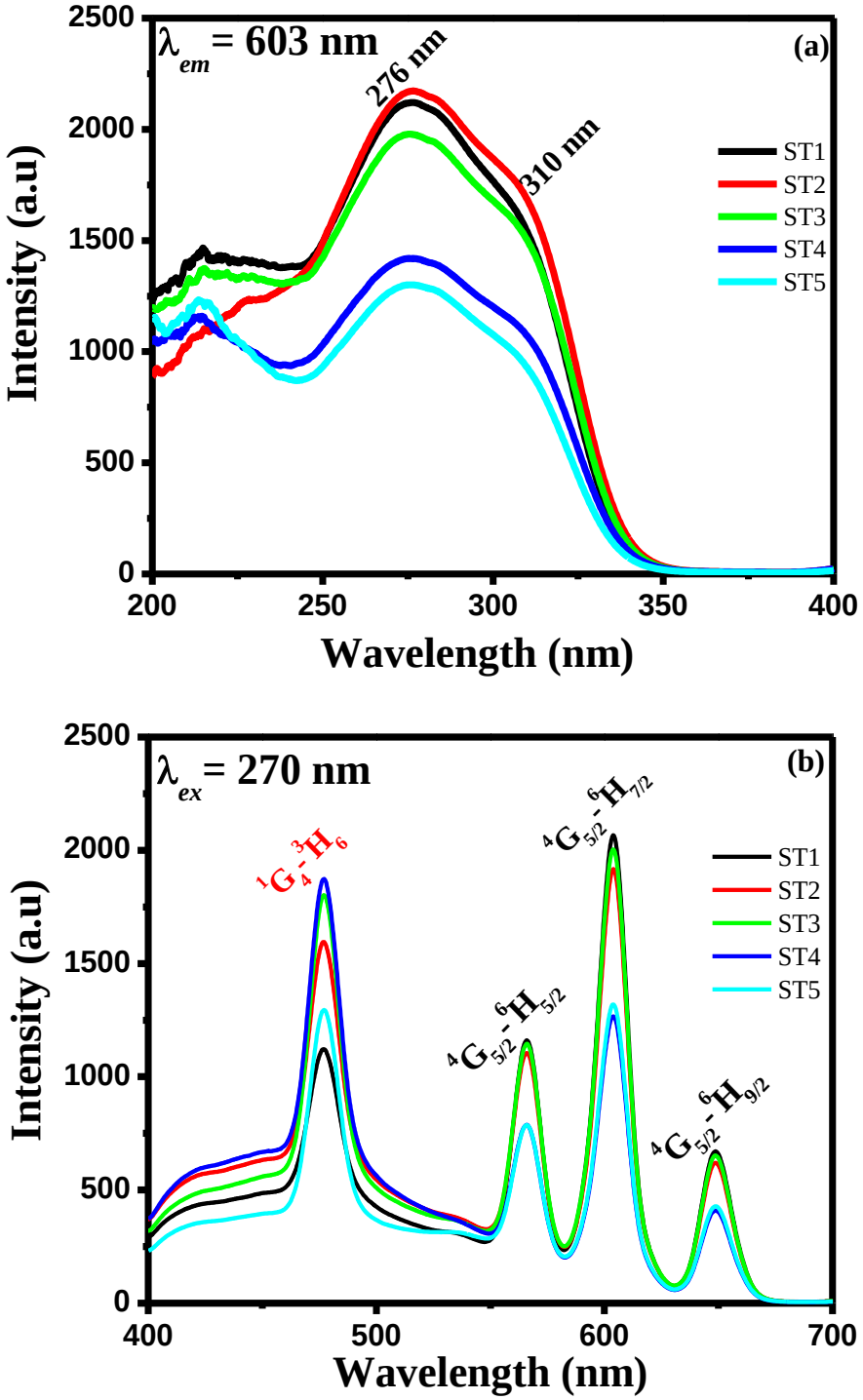

Figure 5.6. *(a) Excitation and (b) Emission spectra of* $GdV_{0.5}P_{0.5}O_4$*: x mol %* Sm^{3+}, Tm^{3+}.

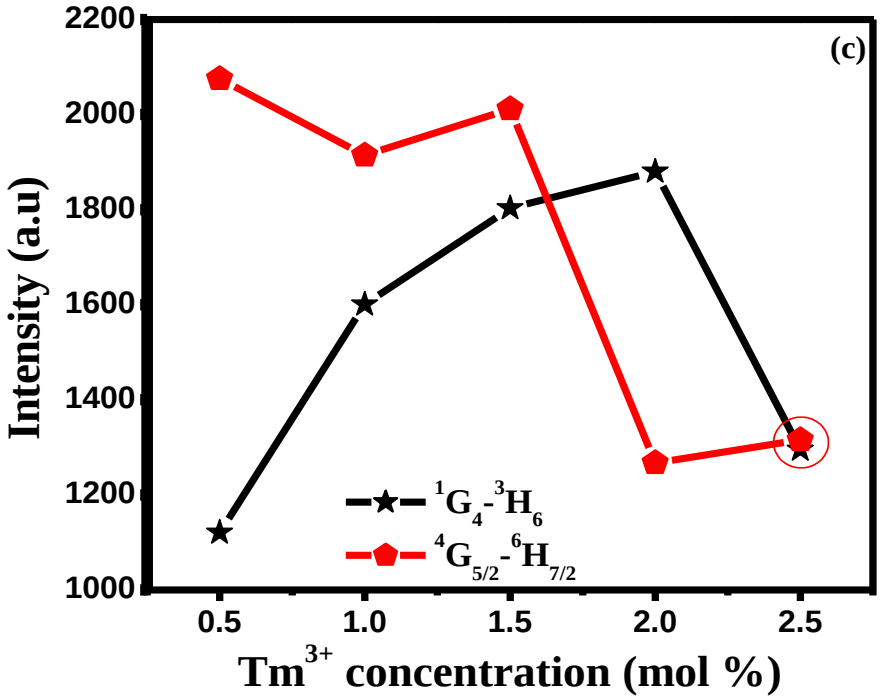

Figure 5.6. *(c) a plot showing the intensity as a function Tm^{3+} concentration.*

The measured excitation spectra displayed a strong broad band peaking at 276 nm. This band is assigned to charge transfer band. The photoluminescence emission spectra of Sm^{3+} and Tm^{3+} co-doped $GdV_{0.5}P_{0.5}O_4$ powder phosphor under 270 nm excitation is displayed in figure 5.6(b). The spectra exhibit four emission peaks. The first blue emission peak at 477 nm ($^1G_4$ — $^3H_6$) is due to transition of Tm^{3+} ion while the other three emission peaks at 567 nm ($^4G_{5/2}$ — $^6H_{5/2}$), 604 nm ($^4G_{5/2}$ — $^6H_{7/2}$) and 650 nm ($^4G_{5/2}$ — $^6H_{9/2}$) were due to Sm^{3+} ion transitions. There is no noticeable change on the emission spectra when the value of *x* is increased except for the change in the intensities. The intensity of the Tm^{3+} ($^1G_4$ — $^3H_6$) increase with an increase in the value of *x* and the maximum is reached when $x = 2$. Further increase in the value of *x* resulted in the decrease in the intensity. On the other hand, the most prominent Sm^{3+} ($^4G_{5/2}$ — $^6H_{7/2}$) emission peak was found to decrease with the increase in the value of *x*. The minimum was reached when $x = 2$ and further increase in the value of *x* resulted in the slight increase in the intensity as shown in figure 5.6(c). Thus, it can be clearly noted that the emission intensity

of Tm^{3+} increases with an increase in Tm^{3+} concentration, while the intensity of the Sm^{3+} decreases.

5.4. Conclusion

Samarium and thulium doped and co-doped gadolinium phosphovanadate was successfully synthesized by using solution combustion method. The XRD analysis confirmed the formation of both singly and doubly doped $GdV_{0.5}P_{0.5}O_4$: Sm^{3+}, Tm^{3+} compound. The XRD data further indicated that the peaks of $GdV_{0.5}P_{0.5}O_4$: Sm^{3+}, Tm^{3+} are slightly shifted towards higher angles due to the difference in ionic radius between vanadium and phosphorus. SEM has revealed that the as prepared powder consists of various shapes including tetragonal, hexagonal and spherical particles. The EDS confirmed the presence of all the elements forming $GdV_{0.5}P_{0.5}O_4$: Sm^{3+}, Tm^{3+} compound. The estimated band gaps were found to be 2.60 eV for Sm^{3+} and Tm^{3+} doped and 3.55 eV for Sm^{3+}, Tm^{3+} co-doped powders. The photoluminescence excitation spectra of the prepared samples showed a strong broad band between 200 and 350 nm with the maximum at $\lambda = 275$ nm. The emission for singly (Sm^{3+} or Tm^{3+}) doped samples showed three peaks at 566 ($^6G_{5/2} — {}^6H_{5/2}$), 603 ($^6G_{5/2} — {}^6H_{7/2}$) and 650 nm ($^6G_{5/2} — {}^6H_{9/2}$) corresponding to transitions of Sm^{3+} while only one emission peak for Tm^{3+} at 477 nm ($^1G_4 — {}^3H_6$) was observed. Dual emissions were also observed from co-doped samples.

5.5 References

1. Yu M, Lin J, Zhou YH, PangML, Han XM,Wang SB, *Thin Solid Films*. 444 (2003)245–253
2. Park K, Kim KY, Shinde KN, *Mater Chem Phys*. 138 (2013) 204–208
3. Reshak AH, Azam S, *Int J Electrochem Sci.* 8 (2013) 10396–10423
4. Wierzbicka E, Malinowska A, Wieteska K, Wierzchowski, Lefeld-Sosnowska M, Swirkowicz M, *Acta Phys Pol A.* 121 (2012) 906–909
5. Cook DC, Cashion JD, *J Phys C Solid State Phys*. 12 (1979) 605–613
6. Gavrilović TV, Jovanovic DJ, Lojpur V, Dramicanin MD, DOI: 10.1038/srep04209
7. Lacomba-Perales R, Errandonea D, Meng Y, Bettinelli M, DOI: 10.1103/*Phys Rev B.* 81.064113
8. Bregiroux D, Fabienne A, Thibault C, Dimitri S, Didier BA, *Solid State Sci*. 9 (2007):432–439
9. Wu CC, Chen KB, Lee CS, Chen TM, Cheng BM, *Chem. Mater*. 16 (2007) 3278–3285
10. Bregiroux D, Champion E, Audubert F, Assollant DB, *J Eur Ceram Soc*. 26 (2006) 279–287
11. Evangelisti M, Sorop TG, Bakharev ON, Visser D, Hillier AD, Alonso JJ, DOI: 10.1103/*Phys. Rev B.* 84.094408
12. Sun J, Xian J, Xia Z, Du H, *J Lumin.* 130 (2010) 1818–1024
13. Su X-Q, Yan B, *Mater Chem Phys*. 93 (2005) 552–556
14. Angiuli F, Mezzadri F, Cavalli E, *J Solid State Chem.* 184 (2011) 1843–1849
15. Jin Y, Li C, Xu Z, Cheng Z, Wang W, Li G, *Mater Chem Phys.* 129 (2011) 418–423
16. Jo DS, Luo YY, Senthil K, Masaki T, Yoon DH, *Opt. Mater.* 33 (2011) 1190–1194
17. Yan B, Su X, *J Alloy Compd* 431 (2007) 342–347
18. Pawar A, Jadhav A, Kim CW, Cha HG, Pal U, Kang YS, *J Lumin.* 156 (2015) 131–136

19. Park WJ, Jung MK, Masaki SJ, Yoon DH, *Mater. Sci. Eng.* B. 146 (2008) 95–98

20. Fu Z, Sheng T, Wu Z, Yu Y, Cui T, *Mater. Res. Bull.* 56 (2014) 138–142

21. Jovanovic DJ, Antic Z, Krsmanovic RM, Metric M, Dordevic V, Bartova B, *Opt Mater.* 35 (2013)1797–1804

22. Xie J, Mei L, Geng J, Lui H, Ma B, Guan M, Liao L, Guocheng LV, *J Solid State Chem.* 231 (2015) 212–216

23. Yan Y, Hojamberdiev M, Xu Y, Wang J, Luan Z, *Opt. Mater.* 139 (2013) 298–304

Chapter 6 Combustion synthesis and characterization of Sm^{3+} and Tm^{3+} co-activated yttrium orthovanadate phosphate

Advanced Materials Letters ***8****(6) (2017) 735−740*

6.1 Introduction

Yttrium orthophosphate (YPO_4) and orthovanadates (YVO_4) have been investigated for a long time because of their interesting properties such as excellent thermal and chemical stability among other things [1-3]. They are also excellent host lattices for rare earth ions to produce a variety of light emitting materials with high luminescence quantum yields and emission originating from the f–f transitions [4-7] and high absorption coefficients at pumping wavelengths. YVO_4 belongs to tetragonal crystal, and has similar structure as $ZrSiO_4$. In this structure, 4 oxygen atoms occupy every vanadium atom, 8 oxygen atoms occupy every yttrium atom and 8 oxygen atoms form 2 distorted tetrahedron [8]. YPO_4 also belongs to tetragonal system with zircon type structure, with 4 oxygen atoms occupying every phosphorus atom, 8 oxygen atoms occupying every yttrium atom, and 8 oxygen atoms forming two distorted tetrahedron [9].

Research has shown that the stability and high temperature luminescent properties of YVO_4 or YPO_4 can be improved even further by mixing the two systems [10]. Depending on the annealing temperature, this system can also crystallize in a tetragonal structure and it is an excellent host for rare earth ions. Various methods have been used before to synthesize multicomponent structures of yttrium orthovanadatephosphate [11 - 14].

In this work, solution combustion method was used to prepare samarium (Sm^{3+}) and thulium (Tm^{3+}) co-activated yttrium orthovanadatephosphate ($YV_{0.5}P_{0.5}O_4$: Sm^{3+}, Tm^{3+}) phosphor that can be used as down-converters in dye sensitized solar cells (DSSCs). With the growing requirements in global renewable energy, dye sensitized solar cells (DSSC) have been widely

studied as alternatives for the generation of electricity from sunlight due to their relatively high performance and simple production process [14]. Recently, Zhao and his group [16], have reported the conversion efficiency in DSSCs of up to 48%. These solar cells can only absorb in the visible region and other wavelengths like energy rich ultraviolet (UV) radiation are wasted. Furthermore, the degradation of the solar cells due to the incidence of UV radiation is an important detrimental factor that reduces its efficiency [17]. These drawbacks can be fixed by coating with a down-conversion or up-conversion phosphor material layer that has the potential to enhance the efficiency of the DSSCs by converting UV or near infrared radiation to visible emission [18]. That is, coating the DSSCs with these phosphor materials will increase their absorption range and make them harvest more light and therefore improve their power conversion efficiency [19]. However, we will not report on the application of $YV_{0.5}P_{0.5}O_4$: Sm^{3+}, Tm^{3+} in DSSCs.

6.2 Experimental

The starting materials: AR grade 99.99% yttrium nitrate hexahydrate ($Y(NO_3)_3.6H_2O$), ammonium metavanadate (NH_4VO_3), ammonium phosphate ($NH_4H_2PO_4$), urea (CH_4N_2O), samarium nitrate hexahydrate ($Sm(NO_3)_3.6H_2O$) and thulium nitrate hexahydrate ($Tm(NO_3)_3.6H_2O$) where purchased from sigma Aldrich and were used without further purification. Samarium and/or thulium activated yttrium vanadate-phosphate $YV_{0.5}P_{0.5}O_4$: *x* mol % Sm^{3+} (*x = 1, 2 and 3*) phosphors were synthesized by solution combustion method using urea as a fuel. In a typical procedure, stoichiometric amounts of yttrium nitrate ($Y(NO_3)_3.6H_2O$), ammonium metavanadate (NH_4VO_3), ammonium phosphate ($NH_4H_2PO_4$), Samarium nitrate ($Sm(NO_3)_3.6H_2O$) and urea (CH_4N_2O) were dissolved in 15 ml of deionized water in different glass beakers. The mixtures were stirred on a magnetic hotplate at a temperature of ± 70^oC until homogeneous solutions were obtained. The solutions were then

transferred into different crucibles and subsequently transferred into a muffle furnace preheated to a temperature of 600 ± 10 ^{o}C. As a result of exothermic reaction that took place, the final products were fluffy ashes. The resulting combustion ashes were then cooled down in air at room temperature and were manually ground gently using pestle and mortar to obtain a fine powder. The powders were then annealed in air at 900^{o}C for 2 hours. The same procedure was used for the synthesis of thulium activated yttrium vanadate-phosphate $YV_{0.5}P_{0.5}O_4$: *x* mol % Tm^{3+} (*x = 1, 2 and 3*) and samarium/thulium doubly doped yttrium vanadate-phosphate $YV_{0.5}P_{0.5}O_4$: *x* mol % Sm^{3+}, *y* mol % Tm^{3+}.

The XRD spectra were recorded using Siemens D5000 powder Diffractometer. The X-ray radiation used during the measurement was a CuKα source (λ= 1.5406 Å). Reflectance spectra were measured using UV-vis spectrophotometer Lambda 950 (PerkinElmer). The photoluminescence (both excitation and emission) data were recorded using a Hitachi F700 fluorescence spectrophotometer. The morphology and elemental composition of the materials were obtained using Jeol JSM-7800F field emission scanning electron microscope (FE-SEM) fitted with Oxford Aztec 350 X-Max80 energy-dispersive X-ray spectroscopy (EDS) and a high-resolution transmission electron microscope (HR-TEM) JEOL JEM 2100.

6.3 Results and discussion

6.3.1 XRD

Figure 6.1(a) shows the XRD patterns of $YV_{0.5}P_{0.5}O_4$: Sm^{3+}, Tm^{3+} powder phosphors annealed at 900^{o}C for 2 hours. The XRD spectra show diffraction peaks associated with YVO_4 (JCPDS file no. 17 − 0341) and YPO_4 (JCPDS file no. 11 − 0254) and this suggests that our $YV_{0.5}P_{0.5}O_4$ was an admixture of YVO_4 and YPO_4 components. Furthermore, the result indicates that the powder phosphors were crystalline and the diffraction peaks were broadened suggesting that

the average crystallite size was small. The lattice strain and the crystallite sizes were estimated from equation 4.1

A plot of $\beta \cos\theta$ versus Sin θ of un-doped $YV_{0.5}P_{0.5}O_4$ is presented in figure 6.1(b). The lattice strain was estimated from the slope of the graph while the crystallite size was estimated from the *y*-intercepts. The estimated lattice strain and crystallite size of un-doped $YV_{0.5}P_{0.5}O_4$, and of either Sm^{3+}/Tm^{3+} single doped and Sm^{3+}-Tm^{3+} co-doped $YV_{0.5}P_{0.5}O_4$ are presented in Table 6.1. As evident from the table, the host has the least crystallite size with less lattice strain while the doped and doubly doped samples have larger sizes on average with higher lattice strains. The increase in lattice strain is assumed to be a result of difference in ionic radii of Y and the dopants (i.e. Tm and Sm).

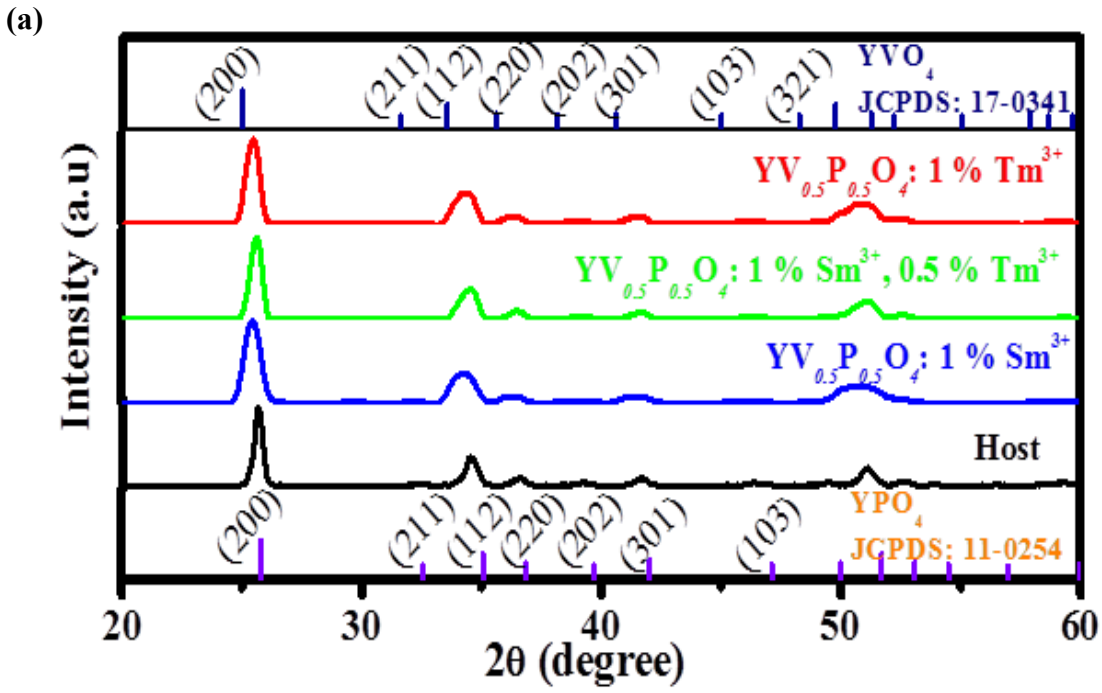

Figure 6.1. ***(a)***. *XRD patterns of $YV_{0.5}P_{0.5}O_4$ host, singly doped $YV_{0.5}P_{0.5}O_4$: 1 mol% Sm^{3+}/ 1 mol% Tm^{3+} and co-doped 1 mol% Sm^{3+}; 0.5 mol % Tm^{3+}.*

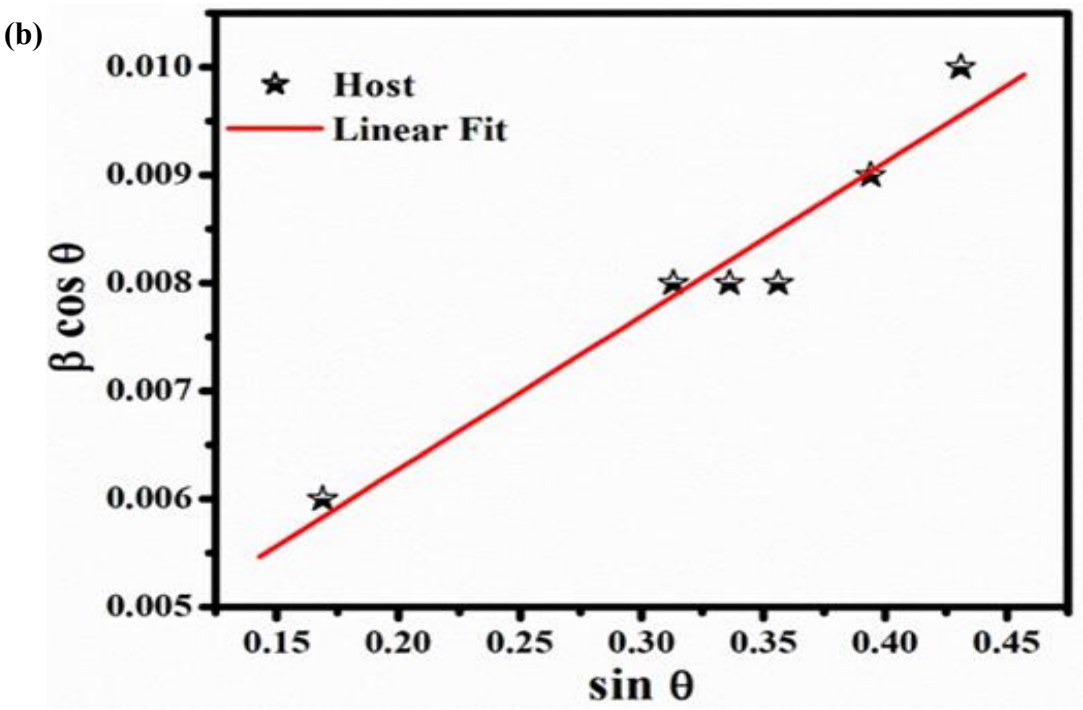

Figure 6.1 ***(b)***. *A plot of β cos θ against Sin θ of $YV_{0.5}P_{0.5}O_4$ (host).*

Table 6.1. *Estimated lattice strain and the crystallite sizes of $YV_{0.5}P_{0.5}O_4$, $YV_{0.5}P_{0.5}O_4$: 1 mol % Sm^{3+}, $YV_{0.5}P_{0.5}O_4$: 1 mol % Tm^{3+} and $YV_{0.5}P_{0.5}O_4$: 1 mol % Sm^{3+}; 0.5 mol % Tm^{3+}.*

Sample	***D*** **(nm)**	***η***
$YV_{0.5}P_{0.5}O_4$	46.10	1.694×10^{-2}
$YV_{0.5}P_{0.5}O_4$: 1 mol % Tm^{3+}	63.36	2.739×10^{-2}
$YV_{0.5}P_{0.5}O_4$: 1 mol % Sm^{3+}	95.70	4.645×10^{-2}
$YV_{0.5}P_{0.5}O_4$: 1 mol % Sm^{3+}; 0.5 mol % Tm^{3+}	73.81	3.759×10^{-2}

6.3.2 Surface morphology and elemental composition

Figure 6.2 shows the SEM images of $YV_{0.5}P_{0.5}O_4$: 3 mol % Sm^{3+}, 2.5 mol % Tm^{3+} phosphor powder prepared by solution combustion method before annealing (a) and after annealing at 900 ^oC for 2 hours (b and c). The SEM image of the un-annealed phosphor powder shows that the powder was agglomerated with 3D structures of various shapes orderly built on top of each other forming thick sheets. On the other hand, annealed phosphor powder consists of un-agglomerated 3D structures of various shapes which include among others, spheres, ovals and cuboids. Furthermore, the particles have different sizes and are less agglomerated. To further investigate the surface morphology, transmission electron microscopy (TEM) was used.

Figure 6.2 (d) and (e) shows the energy dispersive X-ray spectroscopy (EDS) spectrum of $YV_{0.5}P_{0.5}O_4$: 3 mol % Sm^{3+}, 2.5 mol % Tm^{3+}. The spectra for both annealed and un-annealed show the presence of major elements, namely, Y, V, P, O, Sm and Tm. The atomic ratio of Y, V, P, O, Sm and Tm is approximately 49:28:11:09:2. In figure 6.2(d) there are some traces of carbon, which is not associated with our sample in this case, but it is assumed to have come from the carbon tape used to mount the sample. Figure 6.2 (f and g) present the TEM images of $YV_{0.5}P_{0.5}O_4$: 3 mol % Sm^{3+}, 2.5 mol % Tm^{3+} phosphor powder. The particles are agglomerated and they have various sizes and shapes (Figure 6.2(f)). Furthermore, it can also be observed that resolved lattice fringes were formed, confirming that the powder has high level of periodicity and was therefore highly crystalline. This is evident from figure 6.2 (g) and this is consistent with the obtained XRD results.

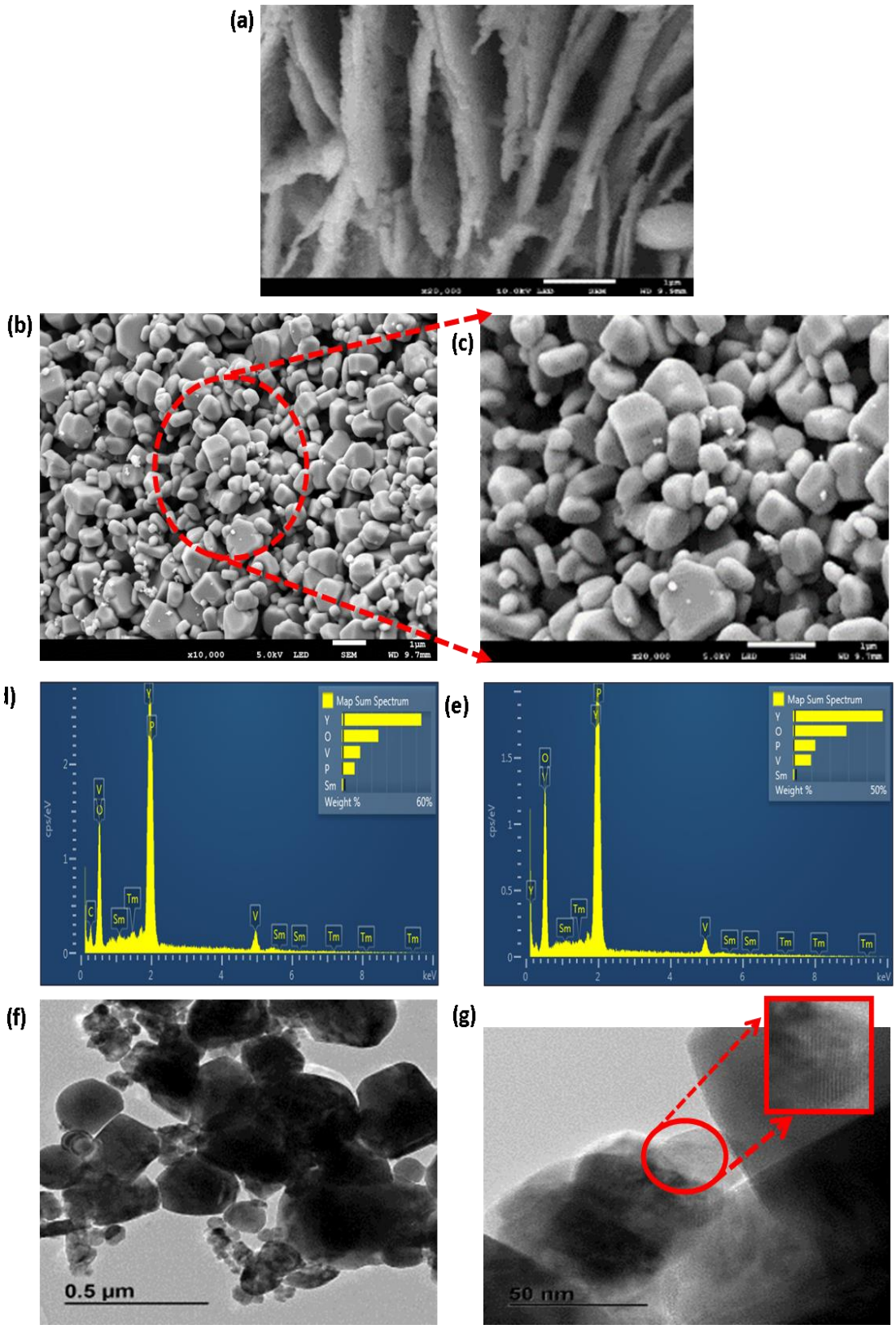

Figure 6.2. ***(a)*** *Unannealed* ***(b)*** *and* ***(c)*** *annealed: SEM micrographs of* $YV_{0.5}P_{0.5}O_4$*: 3 mol %* Sm^{3+}*, 2.5 mol %* Tm^{3+}*. Low* ***(d)*** *and high* ***(e)*** *magnification TEM images of* $YV_{0.5}P_{0.5}O_4$*: 3 mol %* Sm^{3+}*, 0.25 mol %* Tm^{3+}*. EDS spectra of* $YV_{0.5}P_{0.5}O_4$*: 3 mol %* Sm^{3+}*, 2.5 mol %* Tm^{3+} ***(f)*** *annealed (****g****) annealed.*

6.3.3 UV-Vis reflectance spectroscopy

Figure 6.3 presents the room temperature reflectance spectra of $YV_{0.5}P_{0.5}O_4$: *x* mol % Sm^{3+} (*x* = 1, 2, 3). The spectrum in figure 6.3(a) displays a plateau of high reflection in the wavelength range of 550–800 nm. The broad absorption band ranging from 200–550 nm with a maximum absorption at ~ 300 nm was observed and it is attributed to the O → V charge transfer transitions of $[VO_4]^{3-}$ [20, 21]. According to the literature [21], V atoms occupy three different sites V1, V2 and V3, all of which consists of $[VO_4]$ tetrahedral.

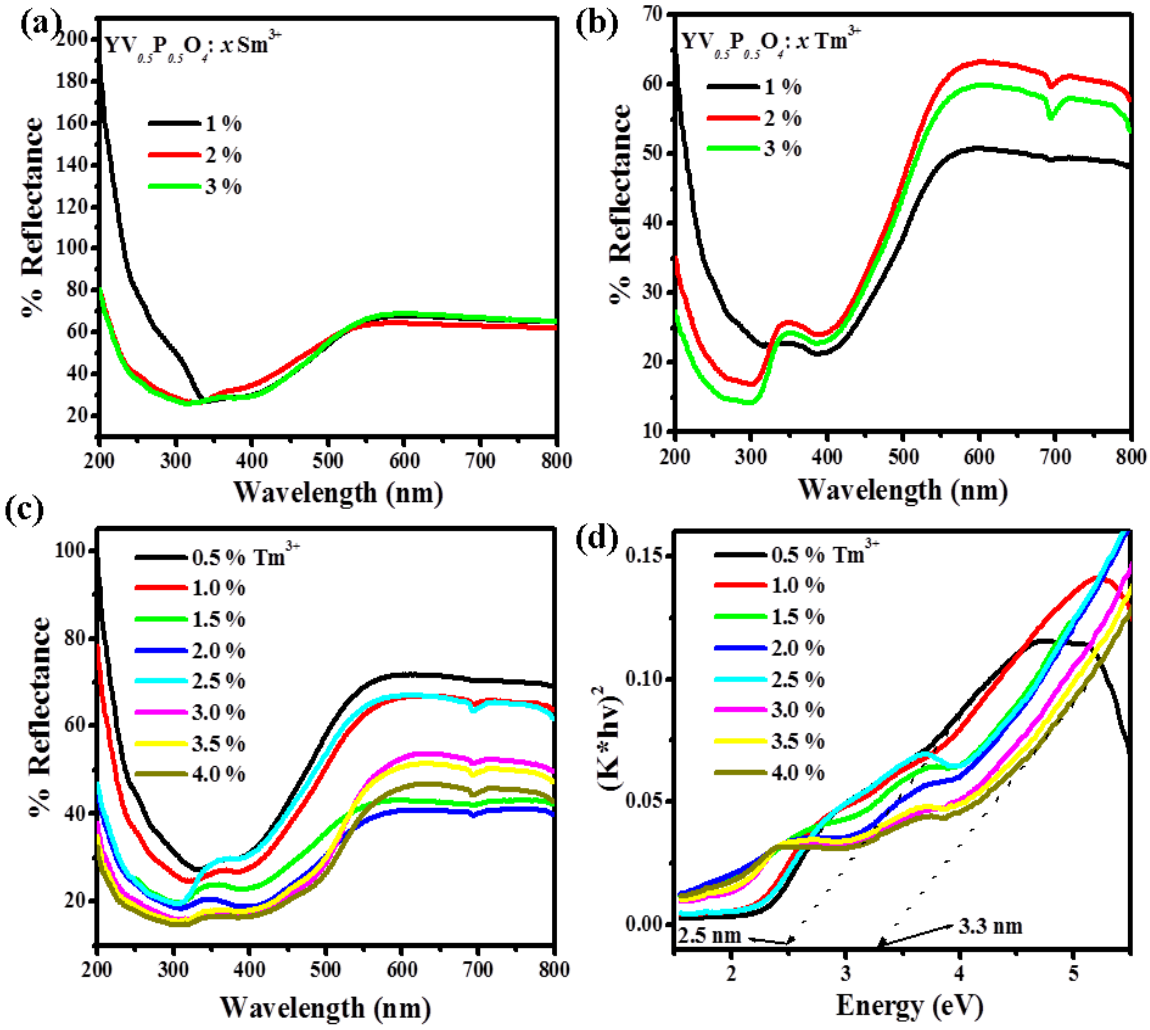

Figure 6.3. *UV-vis reflectance spectra of (a) $YV_{0.5}P_{0.5}O_4$: x mol % Sm^{3+}, (b) x mol % Tm^{3+}, (c) 3 mol %Sm^{3+}; x mol % Tm^{3+} and (e) 1 mol % Tm^{3+}; x mol % Sm^{3+}. (d) Transformed Kubelka-Munk reflectance spectrum of 3 mol % Sm^{3+}; x mol % Tm^{3+}, and (f) 1 mol % Tm^{3+}; x mol % Sm^{3+}.*

Therefore, this absorption band must come from the combination of O ─ V1, O ─ V2 and O ─ V3 charge transfer transitions [21, 22]. In figure 6.3(a), (b) and (c) respectively, a similar trend was observed except for the additional small band at ~ 692 nm in the doped samples. This small band, which increased with the concentration of Tm^{3+}, corresponds to $^3H_6 — {}^3F_3$ transition of Tm^{3+} [23]. The estimated band gaps as shown in figure 6.3 (d) range between 2.5 to 3.3 and 3.2 to 3.4 nm for 3 mol % Sm^{3+}; *x* mol % Tm^{3+} and 1 mol % Tm^{3+}; *x* mol % Sm^{3+} respectively.

6.3.4 Photoluminescence

Figure 6.4(a) shows the excitation spectra of $YV_{0.5}P_{0.5}O_4$: *x* mol % Tm^{3+} (*x* =0, 1, 2, 3) phosphors obtained by monitoring the emission wavelength at 477 nm. The excitation spectra show two strong broad bands in the UV region. The band extending from 200 to 230 nm is attributed to host absorption [13] while the one between 230 and 350 nm with a maximum at 280 nm is ascribed to $Tm^{3+} \rightarrow O^{2-}$ charge transfer bands [11,24, 25**]**. Figure 6.4(b) show the emission spectra of $YV_{0.5}P_{0.5}O_4$: *x* mol % Tm^{3+} (*x* =0, 1, 2, 3). The emission spectra were recorded when the phosphor powders were excited with a wavelength of 280 nm. The spectra exhibit similar trend with a broad band ranging from 400 to 550 nm and one dominant blue peak at around 477 nm for Tm^{3+} doped samples. These bands are ascribed to host emission peak and $^1G_4 - {}^3H_6$ transition of Tm^{3+} respectively. Figure 6.4(c) shows the intensity of blue emission ($^1G_4 - {}^3H_6$) as a function of Tm^{3+} concentration. The peak intensity decreased with increasing Tm^{3+} molar concentration due to concentration quenching effects [26]. The highest emission was found when *x* = 1.

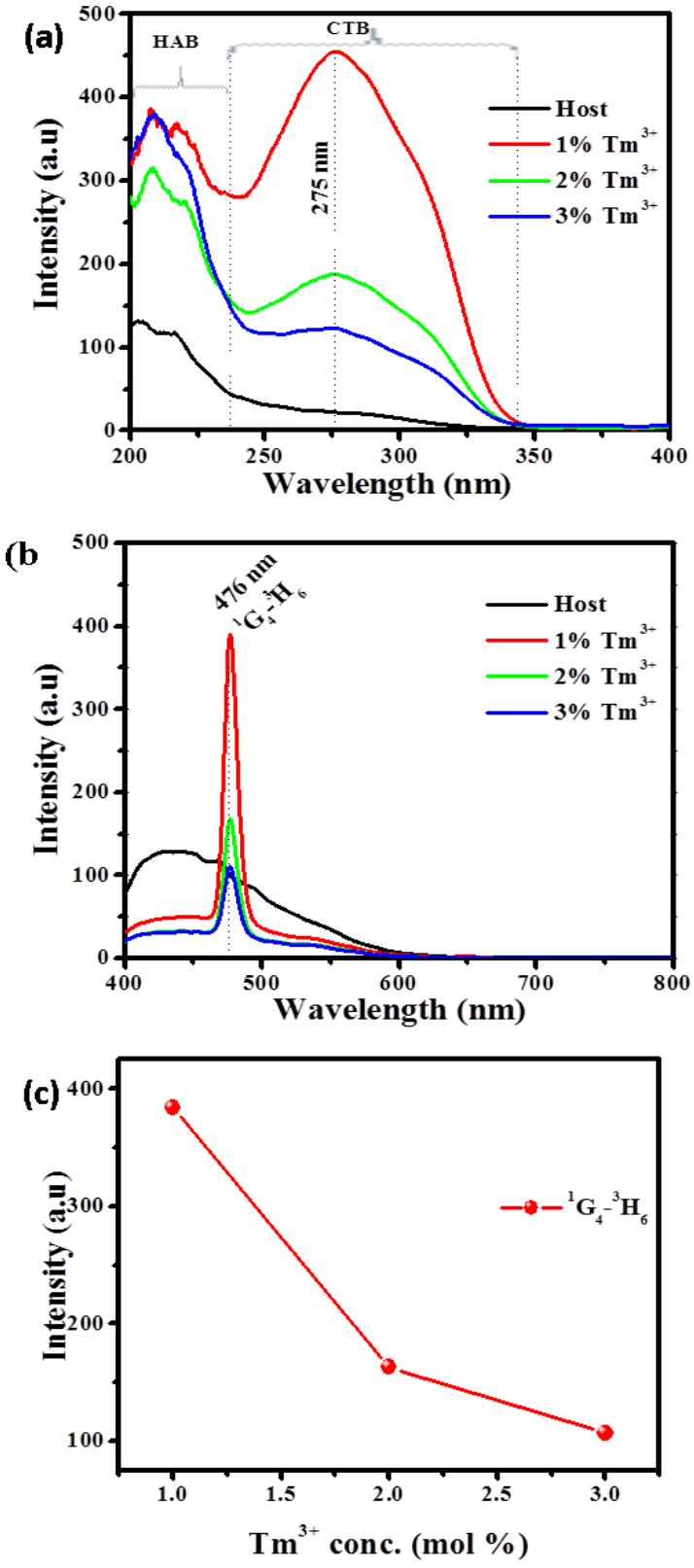

Figure 6.4. *(a) Excitation and (b) Emission spectra of $YV_{0.5}P_{0.5}O_4$: x mol % Tm^{3+} and (c) a plot showing the intensity as a function Tm^{3+} concentration.*

The excitation and emission spectra of $YV_{0.5}P_{0.5}O_4$: *x* mol % Sm^{3+} are shown in figure 6.5(a) and (b) respectively. The excitation spectra were recorded when monitoring the emission wavelength at 604 nm. The spectrum of the un-doped sample shows a broad band extending from 200 to 230 nm. This band is attributed to the host absorption. On the other hand, the spectra for doped samples show a strong broad band in the UV region extending from 200 to 350 nm with maximum at 275 nm. This band is due to $Sm^{3+} \rightarrow O^{2-}$ charge transfer band. The emission spectra measured under the excitation wavelength of 275 nm show four bands centered at 444, 566, 604 and 649 nm respectively. The band located at 444 nm is due to the host while other three bands are due to ($^6G_{5/2} — {}^6H_{5/2}$), ($^6G_{5/2} — {}^6H_{7/2}$) and ($^6G_{5/2} — {}^6H_{9/2}$) transitions of Sm^{3+} respectively. The emission intensity was found to increase when the concentration of Sm^{3+} was increased from 1 to 2.5 mol% and then decreased when the concentration was 3 mol% and beyond, and this was probably due to concentration quenching effects. Concentration quenching is caused by an increase in the number of non-radiative transitions [27, 28]. The room temperature photoluminescence excitation spectra of $YV_{0.5}P_{0.5}O_4$: 3 mol % Sm^{3+}, *x* mol % Tm^{3+} and $YV_{0.5}P_{0.5}O_4$: 1 mol % Tm^{3+}, *x* mol % Sm^{3+} (*x* = 0.5, 1.0, 1.5, 2.0 and 2.5) phosphors are shown in figure 6.6(a) and (c). The spectra were recorded when monitoring the emission wavelength at 604 nm. A strong broad band ranging from 200 to 350 nm with a maximum at 275 nm was observed. This broad band is ascribed to charge transfer band from oxygen ligands to central vanadium in the $[VO_4]^{3-}$. The emission spectra, shown in figure 6.6(b) and (d), comprise of five bands. The broad band extending from 400 to 650 nm originates from the host while the sharp peak at the wavelength of 476 nm is due to ($^1G_4 — {}^3H_6$) transition of Tm^{3+} ions. The other three emission peaks observed at 566 nm ($^4G_{5/2} — {}^6H_{5/2}$), 604 nm ($^4G_{5/2} — {}^6H_{7/2}$) and 649 nm ($^4G_{5/2} — {}^6H_{9/2}$) are due to transitions of Sm^{3+} ions.

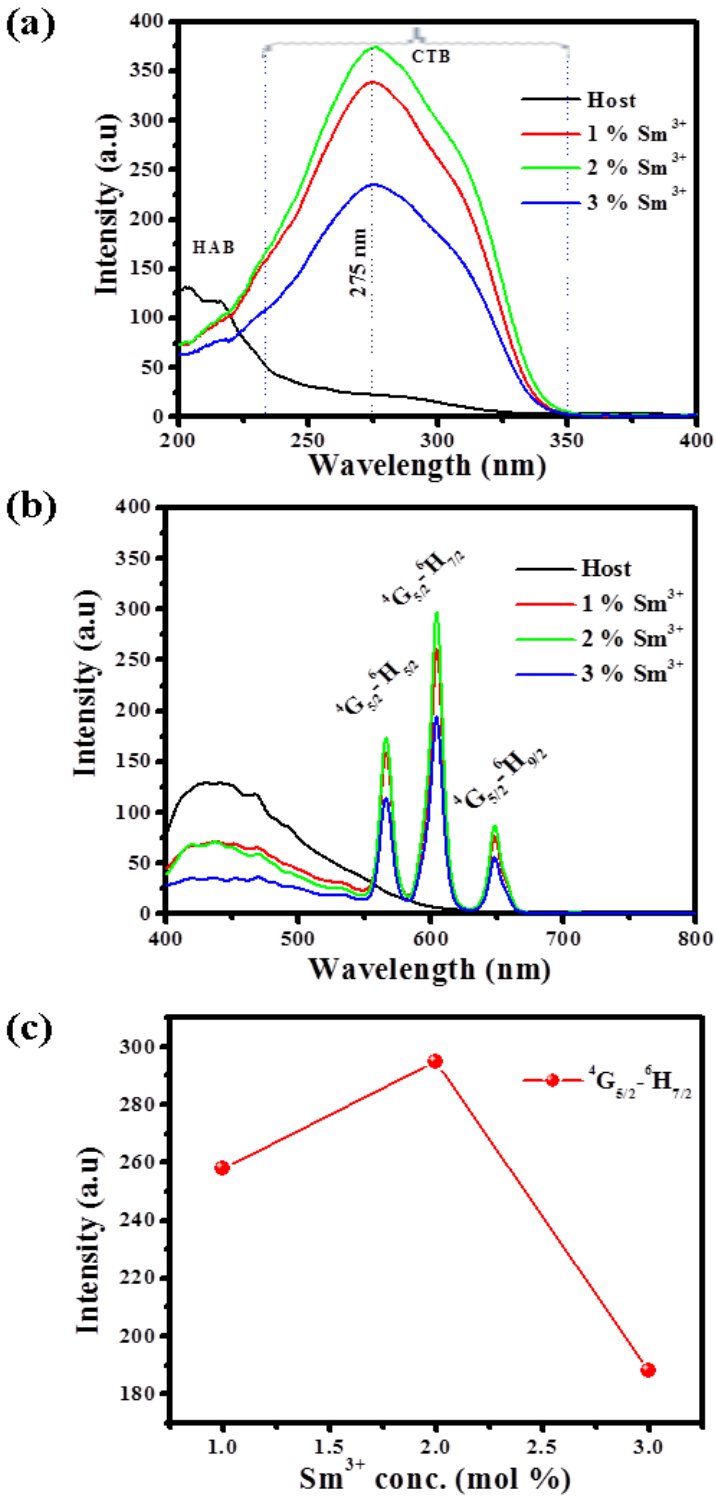

Figure 6.5. *(a) Excitation and (b) Emission spectra of $YV_{0.5}P_{0.5}O_4$: x mol % Sm^{3+} (c) a plot showing the intensity as a function Sm^{3+} concentration.*

Figure 6.6 (e) and (f) show the relative emission intensities of Tm^{3+} ($^1G_4$ — $^3H_6$) and Sm^{3+} ($^4G_{5/2}$ — $^6H_{7/2}$) as a function of molar concentration of Tm^{3+} and Sm^{3+} respectively. The increase in the molar concentration of Tm^{3+} did not make any noticeable change on the peak shape or position, but there was a significant change on the emission intensities. The emission intensity of Tm^{3+} was found to increase with an increase in the molar concentration of Tm^{3+}, while the emission intensity of Sm^{3+} was found to decrease. Similar behavior was observed with an increase in the molar concentration of Sm^{3+}. Further increase in the molar concentration of Tm^{3+} or Sm^{3+} resulted in the decrease in the intensity of both Tm^{3+} and Sm^{3+}. This phenomenon suggests that there is energy transfer from Sm^{3+} to Tm^{3+}. Co-doping, in this work, played a pivotal role in the enhancement of luminescence intensity. Compared with singly doped samples, doubly doped samples have the intensities that were almost three times higher. The simplified proposed mechanism of energy transfer from the host and Sm^{3+} to Tm^{3+} is shown in figure 6.6(g). The UV radiation is initially absorbed by the host to promote electrons from $^1A_1$, the ground state, to ^1T_j ($j = 2, 1$), the excited state of $[VO_4]^{3+}$. Some of these excited electrons undergo a non-radiative process to ^3T_j and eventually return to their ground state therefore emitting light, while other electrons from ^3T_j transfer their energy to the $^4G_{7/2}$ levels, the excited state of Sm^{3+}, which in turn relaxed non-radiatively to $^4F_{3/2}$ and $^4G_{5/2}$ with subsequent emissions of Sm^{3+}. On the other hand, other electrons from $^4G_{7/2}$ level of Sm^{3+} transfer some of their energy to $^1D_2$ level, the excited state of Tm^{3+}, followed by a non-radiative relaxation process to the $^1G_4$ sate and finally producing blue emission from Tm^{3+}.

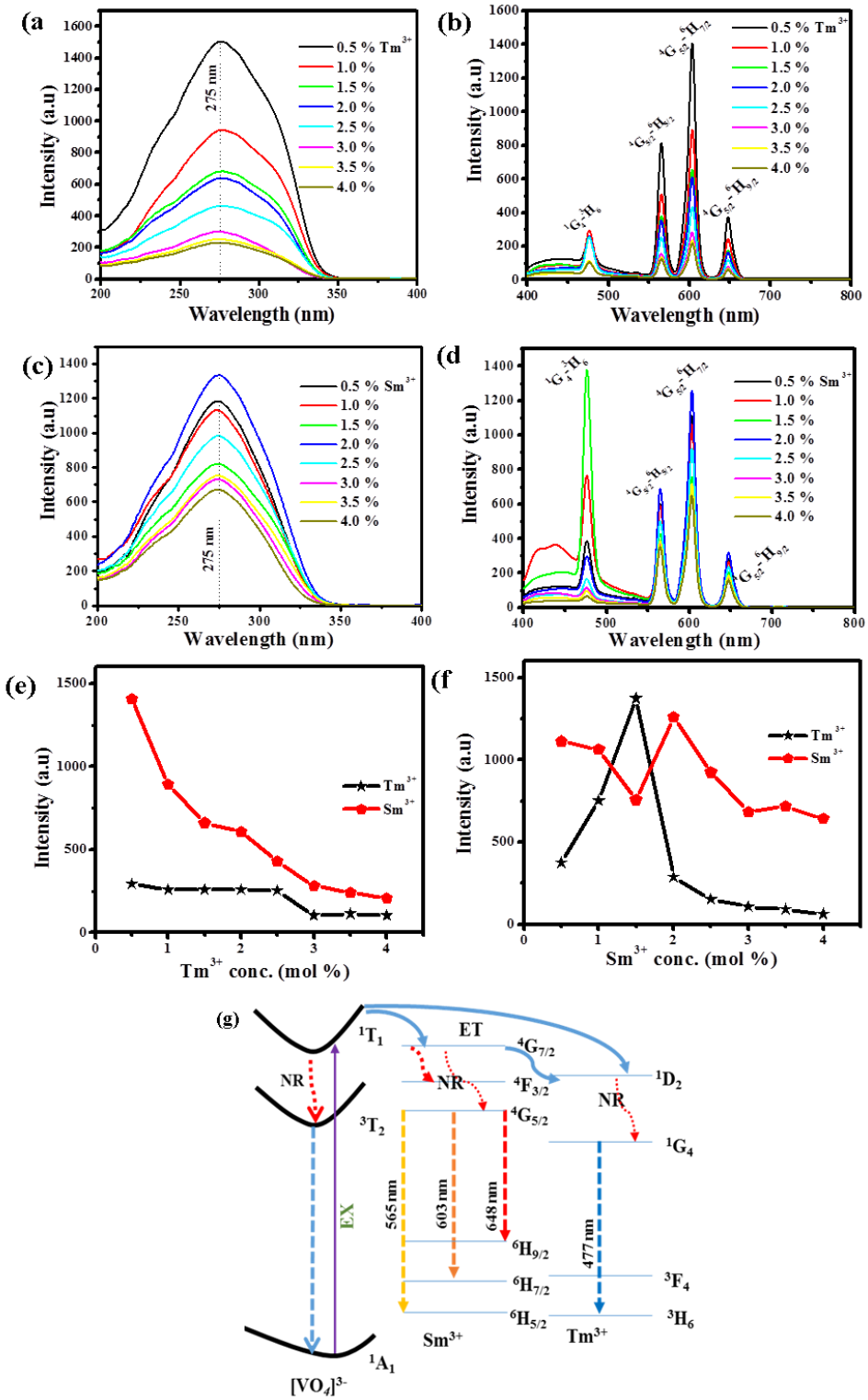

Figure 6.6. *(a) Excitation and (b) Emission spectra of $V_{0.5}P_{0.5}O_4$: 3 mol % Sm^{3+}, x mol % Tm^{3+} (c) Excitation and (d) Emission spectra of $YV_{0.5}P_{0.5}O_4$: 1 mol % Tm^{3+}, x mol % Sm^{3+} (e) a plot showing the intensity as a function Sm^{3+} and (f) Tm^{3+} concentration (g) Schematic representation energy level diagram and proposed mechanism.*

6.4 Conclusion

In conclusion, the multicomponent structures of samarium and thulium co-activated yttrium orthovanadatephosphate were successfully synthesized by solution combustion method using urea as fuel. The XRD results indicated that the prepared nanophosphors of both singly and doubly doped $YV_{0.5}P_{0.5}O_4$: Sm^{3+}, Tm^{3+} compounds have tetragonal structure with the peaks intermediate between that of pure YVO_4 and YPO_4. The SEM and TEM images showed that the samples consisted of different sizes and shapes that included spheres, ovals and cuboids. TEM data further showed well defined lattice fringes indicating that the samples were highly crystalline as confirmed by XRD results. The EDS analysis showed that all the elements forming $YV_{0.5}P_{0.5}O_4$: Sm^{3+}; Tm^{3+} were present in the compound. The UV-vis reflectance spectra had similar trend for all the samples with a broad absorption band towards ultraviolet region, except for Tm^{3+} doped samples that displayed a small absorption signature at the wavelength of ~ 692 nm corresponding to $^3H_6 — {}^3F_3$ transition of Tm^{3+}. The photoluminescence excitation spectra for singly doped Tm^{3+} and Sm^{3+} and co-doped Sm^{3+}; Tm^{3+} showed a strong broad band between 200 and 350 nm peaking at λ = 275 anm. Tm^{3+} and Sm^{3+} singly doped samples showed one emission peak at 476 nm ($^1G_4 — {}^3H_6$) and three other emission peaks at 566 ($^6G_{5/2} — {}^6H_{5/2}$), 604 ($^6G_{5/2} — {}^6H_{7/2}$) and 649 nm ($^6G_{5/2} — {}^6H_{9/2}$) corresponding to transitions of Tm^{3+} and Sm^{3+}. Both Tm^{3+} and Sm^{3+} emission peaks were observed from co-doped samples. The PL results for co-doped phosphors indicated that an increase in Tm^{3+} molar concentration resulted in the decrease in the emission intensity of Sm^{3+} suggesting that there was energy transfer from Sm^{3+} to Tm^{3+}. The UV-vis and photoluminescence results indicated that the prepared phosphor powder might be a suitable candidate for a possible application in solar cells.

6.5 References

1. Liang Y, Chui P, Sun X, Zhao Y, Cheng F, Sun K, *J. Alloys Compd. 552* (2013) 289
2. Cao Y, Liu Y, Feng H, Yang Y, *Ceram Int.* 40 (2014) 15319
3. Li P, Liu Y, Guo Y, Shi X, Zhu G, Zuo H, *Ceram Int.* 41 (2015) 6620
4. Li J, Liu J, Yu X, *J. Alloys Compd.* 509 (2011) 9897
5. He F, Yang P, Niu N, Wang W, Gai S, Wang D, Lin J, *J. Colloid Interface Sci.* 343 (2010) 71
6. Rivera SI, Carrillo FJ, Garcia A, Oliva, *J. Mater. Lett.* 187 (2017) 83
7. Wang H, Odawara, O, Wada H, *J. Alloys Compd.* 683 (2016) 1
8. Zuo Y, Ling W, Wang Y, *J. Lumin.* 132 (2012) 61
9. Yang Y, Ding M, Song G, Fan W, Feng H, *Chem. Phys. Lett.* 139 (2015) 67
10. Jo DS, Luo YY, Senthil K, Masaki T, Yoon DH, *Opt. Mater.* 33 (2011) 1190
11. Yu M, Lin J, Zhou YH, Pang ML, Han XM, Wang SB, *J. Thin. Sol. Film.* 444 (2003) 245
12. Sun J, Xian J, Xia Z, Du H, *J. lumin.* 130 (2010) 1818
13. Sue XQ, Yan B, *Mater. Chem. Phys.* 93 (2005) 552
14. Jin Y, Li C, Xu Z, Cheng Z, Wang W, Li G, Lin J, *Mater. Chem. Phys.* 129 (2011) 418
15. Na Li N, Sun X, Liu R, Xu L, Xu K, Song XM, *Sol. Energy Mat. & Sol. Cells* 157 (2016) 853
16. Zhao R, Huan L, Gu P, Guo R, Chen M, Diao G, *J. of Power Sources.* 331 (2016) 527
17. Florencio LA, Gomez-Malagon LA, Lima BC, Gomes ASL, Garcia JAM, Kassab LRP, *Sol. Energy Mat. & Sol. Cells.* 157 (2016) 468
18. Yao N, Huang J, Fu K, Deng X, Ding M, Shao M, Xu X, *Electrochim. Acta*. 154 (2015) 273

19. Wu J, Wang J, Lin J, Xiao Y, Yue G, Huang M, Lan Z, Huang Y, Fan L, Yin S, Sato T, *Scientific reports* 2013, 3 : 2058 DOI: 10.1038/srep02058

20. Liu Y, Xiong H, Zhang N, Leng Z, Li R, Gan S, *J. Alloys Compd.* 653 (2015) 126

21. Li L, Lui XG, Noh HM, Jeong JH, *J. Sol. State Chem.* 221 (2015) 95

22. Liu X, Li L, Noh HM, Jeong JH, Jang K, Shin DS, *J. Alloys Compds.* 618 (2015) 649

23. Navas J, Coronilla AS, Aguilar T, De los Santos DM, Hernandez NC, Alcantara R, Lorenzo CF, Calleja JM, *Nanoscale.* 6 (2014) 12740

24. Devi CV, Singh NR, *Spectrochim. Acta Part A: Mol. Biomol. Spectrosc.* 2015, *146*, 331

25. Barbosa GN, Graeff CFO, Oliveira HP, *Ecl. Quím., São Paulo,* 30 (2005) 7

26. Li J, Yan H, Yan F, *J. Mater. Sci. Eng. B*, 209 (2016) 56

27. Zhao L, Yongfeng W, Jing C, Yuanru J, Xicheng Z, Zhixing M, *J. Rare Earths,* 34 (2016) 143

28. Kuhn S, Herrmann A, Russel C, *J. Lumin.* 158 (2015) 333

Chapter 7 Synthesis and characterization of Ln^{3+} (Ln = Dy, Sm, Tb) activated lanthanum ortho-phosphovanadate

7.1 Introduction

To a large degree, the quality of human life depends on energy, and this is threatened unless renewable energy resources can be developed in the near future [1]. The concern about present energy policies is that it relies heavily on fossil fuels, which causes environmental problems. Thus, the development of renewable energy sources is at the center of interest for many researchers recently [2]. The conversion of solar energy directly into electricity is one of the most attractive renewable energy sources that could help replace fossil fuels and control global warming [3]. Solar cells absorb some photons from sunlight, which are converted into usable amounts of direct current electricity. The only setback with this renewable energy source is the low absorption efficiency in the visible region.

Another class of materials in place are dye sensitized solar cells (DSSCs) and are a promising method for the efficient and economical conversion of solar energy into electric power. Their advantages over conventional solar cells include aspects such as various colors, semi-transparency, low cost fabrication processes, environmentally friendly and relatively high conversion efficiency [4, 5]. Because of all these advantages, several studies have been carried out in recent years to improve the performance of DSSCs.

For the practical use of DSSCs, thermal and chemical stability is as important as its conversion efficiency [6]. Studies have shown that UV irradiation is the main parameter, which affects the thermal stability of DSSCs [7]. UV filters are commonly employed to absorb UV rays, but this method wastes some part of solar energy. The other strategy is to coat DSSCs with a material that will absorb UV photon energy and down convert it to the visible region, which is

reabsorbed by the dye [8]. The lanthanum orthovanadate ($LaVO_4$) rare earth doped luminescence nanocrystals (NCs) are among the most important functional materials, which can act as UV absorbers [6, 7]. Therefore, for the current work, the multi-component system $LaV_{1-x}P_xO_4$: Ln^{3+} (Ln = Dy, Sm and Tb) powder phosphors were synthesized by combustion method in order to optimize the vanadate to phosphate mol concentrations for application in DSSCs. The concentration of Ln was kept at 1 mol % throughout the experiment. The structural and optical properties of these phosphors are discussed.

7.2 Experiment

7.2.1 Synthesis

The multi-component system $LaV_{1-x}P_xO_4$: 1.0 mol% Ln^{3+} (Ln = Dy, Sm and Tb) with *x* ranging from 0.0 to 1.0 (*odd series*) was synthesized by solution combustion method. The starting materials included AR grade 99.99% lanthanum (III) nitrate hexahydrate ($La(NO_3)_3.6H_2O$), ammonium metavanadate (NH_4VO_3), ammonium phosphate ($NH_4H_2PO_4$), urea (CH_4N_2O), samarium nitrate hexahydrate ($Sm(NO_3)_3.6H_2O$), terbium nitrate hexahydrate ($Tb(NO_3)_3.6H_2O$) and dysprosium nitrate hydrate ($Dy(NO_3)_3.xH_2O$), which were dissolved in de-ionized water in appropriate weights to form the necessary precursor solutions. The solutions were kept on a magnetic stirrer until a homogeneous mixture was achieved. The resulting brownish solutions from the systems of x = 0.0, 0.25, 0.5, 0.75 and the white solution for only x=1.0 were obtained after a constant heating (±90^{o}C) while stirring took place. The solutions were then transferred into different crucibles and placed into a preheated furnace set at 600 ± 10 ^{o}C. The detailed exothermic reactions that took place have been explained in reference [9]. The resulting combustion ashes were cooled down in air to room temperature and were manually, but gently ground using pestle and mortar to obtain a fine powder to be ready for characterization.

7.2.2 Characterization

For the structure and phase identification, the phosphor powder samples prepared were characterized by X-ray diffraction (XRD) Siemens D5000 powder Diffractometer. The X-ray radiation used during the measurement was a CuKα source (λ= 1.5406 Å). The morphology, degree of crystallinity and elemental composition of the materials were obtained using high-resolution transmission electron microscopy (HR-TEM) and Jeol JSM-7800F field emission scanning electron microscope (FE-SEM) fitted with Oxford Aztec 350 X-Max80 energy-dispersive X-ray spectroscopy (EDS). Reflectance spectra were then obtained by using a UV-Vis spectrophotometer Lambda 950 (PerkinElmer). Photoluminescence data were recorded using a Hitachi F700 fluorescence spectrophotometer.

7.3 Results and discussion

7.3.1 X-ray Diffraction

The XRD spectra of $LaV_{1-x}P_xO_4$ (x = 0.0, 0.25, 0.5, 0.75, and 1.0) phosphor powder are shown in figure 7.1. For x = 0, the XRD pattern shows a perfect match with the diffraction patterns of the pure monoclinic structure of $LaVO_4$ referenced in JCPDS file No. 70-2392 [10] while for x = 1.0, the diffraction peaks match well with that of a hexagonal rhabdophane structure for $LaPO_4$ referenced in JCPDS file No. 46-4639 [11]. On the other hand, the XRD pattern for sample with x = 0.25 exhibits the trend of $LaVO_4$ and this is because the concentration of vanadium dominates that of phosphorus. Moreover, the XRD pattern for sample with x = 0.75 favors that of $LaPO_4$ and this is due to a higher concentration of phosphate in the sample. For the sample with x = 0.5, the XRD peaks are located in between those of $LaVO_4$ and $LaPO_4$. The XRD peaks are gradually shifting to the higher value of 2θ. This is due to the difference in the ionic radii of vanadium (0.059 nm) and phosphorus (0.038 nm). On the other hand, the XRD patterns of the singly doped $LaV_{1-x}P_xO_4$: Ln^{3+} (Ln = Dy, Sm, and Tb) showed a similar

trend obtained for un-doped samples. This implies that the dopants where successfully incorporated into the host matrix.

The lattice strain (η) and the average particle size (D) were estimated from equation 4.1. This equation since it represents a straight-line graph, then the slope of the graph can be used to determine the lattice strain η while the y-intercept can be used to calculate D, which mainly represents the particle size. The values of both lattice strain and the particle size are summarized and tabulated in table 7.1.

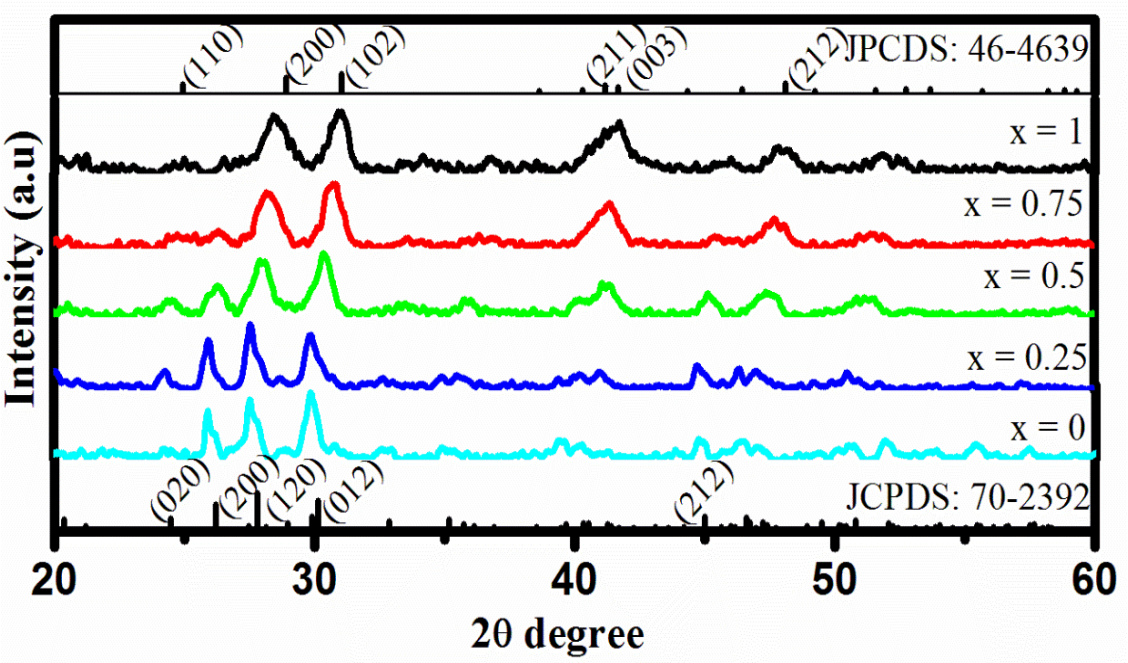

Figure 7.1. *XRD patterns of $LaV_{1-x}P_xO_4$ (x = 0.0, 0.25, 0.5, 0.75, and 1.0) phosphor powder.*

Table 7.1. *Lattice strain and the estimated crystallite size of nanophosphors powder $LaV_{1-x}P_xO_4$: 1.0 mol% Ln^{3+} (Ln = Dy, Sm, and Tb) where (x = 0.0, 0.25, 0.5, 0.75, and 1.0).*

Sample	L (nm)			η		
	Dy^{3+}	Sm^{3+}	Tb^{3+}	Dy^{3+}	Sm^{3+}	Tb^{3+}
$LaVO_4$	13.96	22.35	17.68	0.039	0.023	0.031
$LaV_{0.75}P_{0.25}O_4$	9.49	14.63	13.01	0.051	0.039	0.042
$LaV_{0.5}P_{0.5}O_4$	8.07	8.89	10.25	0.058	0.055	0.049
$LaV_{0.25}P_{0.75}O_4$	9.18	9.59	9.13	0.050	0.047	0.052
$LaPO_4$	9.90	10.85	11.33	0.046	0.043	0.042

7.3.2 Morphology

Scanning electron microscopy (SEM) was carried out to investigate the surface morphology of the prepared phosphor powders. The SEM images are shown in figures 7.2 (a) for $LaV_{0.5}P_{0.5}O_4$: 1 mol % Dy^{3+}, (b) $LaV_{0.5}P_{0.5}O_4$: 1 mol % Sm^{3+} and $LaV_{0.5}P_{0.5}O_4$: 1 mol % Tb^{3+}. In all cases, the SEM images reveal that the phosphor powder consists of agglomerated particles with various sizes, and different shapes including spheres and ovals. Generally, the particles are not evenly distributed due to the nature of the synthesis that is combustion.

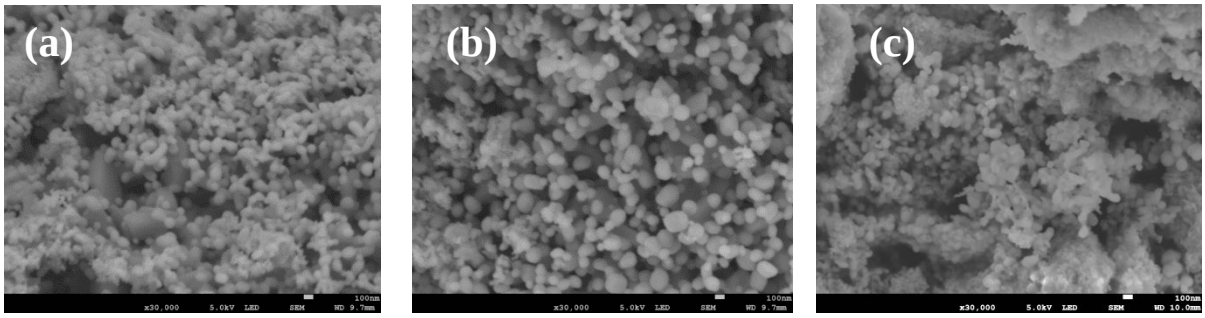

Figure 7.2. *SEM images of $LaV_{0.5}P_{0.5}O_4$ doped with (a) Dy^{3+}, (b) Sm^{3+} and (c) Tb^{3+} phosphor powder.*

To further understand the morphology of samples transmission electron microscopy (TEM) was used. Figure 7.3 shows TEM images of $LaV_{0.5}P_{0.5}O_4$ doped with (a) 1 mol % Dy^{3+}, (b) 1 mol % Tb^{3+} and (c) 1 mol % Sm^{3+}. From the images, it can be seen clearly that the synthesized phosphors have the spherical, oval and rod-like shaped structures with different sizes and lengths. Furthermore, the images show that lattice fringes (shown in red squares) are formed, which is an indication that the powder is well crystalline and this is in good agreement with XRD results.

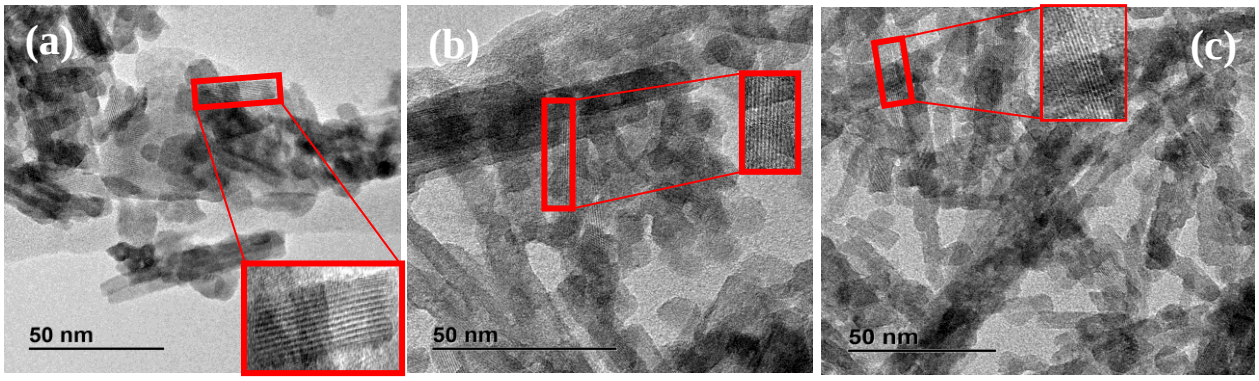

Figure 7.3. *TEM images of $LaV_{0.5}P_{0.5}O_4$ doped with (a) Dy^{3+}, (b) Sm^{3+} and (c) Tb^{3+} phosphor powder.*

7.3.3 UV-Vis spectroscopy

UV measurements were performed on the samples with the highest intensity for each series only. The reflectance spectra of $LaV_{0.5}P_{0.5}O_4$: 1 mol % Ln^{3+} (Ln = Dy, Sm, Tb) phosphor powders are shown in figure 7.3(a). The room temperature UV-Vis diffuse reflectance spectra show a broad absorption band with the maximum at ~ 310 nm. This band is ascribed to charge transfer from the O ligands to the central V/P atom inside V/PO_4^{3+} ions [6].

For further analysis, the Kebelka-Munk relation was used to convert the reflectance spectra into the values that are proportional to the absorbance. To evaluate the band gap energy, the transformed Kubelka-Munk reflectance figure 7.3(b) was used. The estimated band gap energies were found to be 4.06 eV for Dy^{3+}, 3.85 eV for Tb^{3+} and 4.01 eV for Sm^{3+} doped powder.

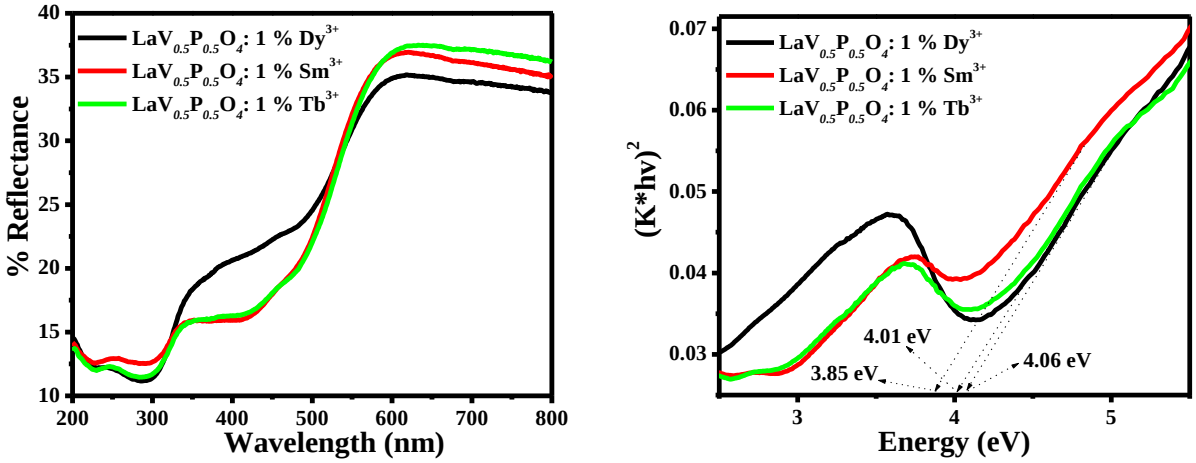

Figure 7.4. *(a) UV-vis reflectance spectra and (b) transformed Kubelka-Munk plot of $LaV_{0.5}P_{0.5}O_4$: 1 mol % Ln^{3+} (Ln = Dy, Sm, Tb).*

7.3.4 Photoluminescence

Figure 7.5(a) shows the excitation spectra in the range of 200-400 nm of $LaV_{1-x}P_xO_4$: 1.0 mol % Dy^{3+} (x = 0, 0.25, 0.5, 0.75, 1.0) phosphor powder samples obtained by monitoring the emission wavelength at 575 nm. All the samples exhibit the same features, with the exception of the $LaPO_4$: 1 mol % Dy^{3+} (x = 1.0). The excitation spectra have a broad band ranging from 200 to 350 nm with the maximum approximately around ± 270 nm.

The sample with x = 1.0, has a broad band ranging from 225 to 300 nm and with the maximum centered at about 270 nm too. Other peaks observed are at the longer wavelengths of 324, 354 and 389 nm, and these can be attributed to Dy^{3+} characteristic transitions, that is, $^6H_{15/2}$—$^4M_{11/2}$, $^6H_{15/2}$—$^6P_{5/2}$ and $^6H_{15/2}$—$^6I_{13/2}$, respectively [12].

The emission spectra of the as-prepared phosphor powders are shown in figure 7.5(b). All the spectra consist of the most two peaks at the wavelengths of 482 and 575 nm. These transitions are attributed to the well-known characteristic emissions associated with the $^4F_{9/2}$ — $^6H_{15/2}$ (blue) and $^4F_{9/2}$ — $^6H_{13/2}$ (yellow) transitions of Dy^{3+} respectively. Figure 7.5(c) shows a plot of the relative intensity as a function of x values. As shown in the graph, the intensity increases with an increase in the value of x. The maximum is mainly reached when x = 0.5. Further increase in the value of x resulted in the decrease in the intensity, as a result this act as a luminescence quencher.

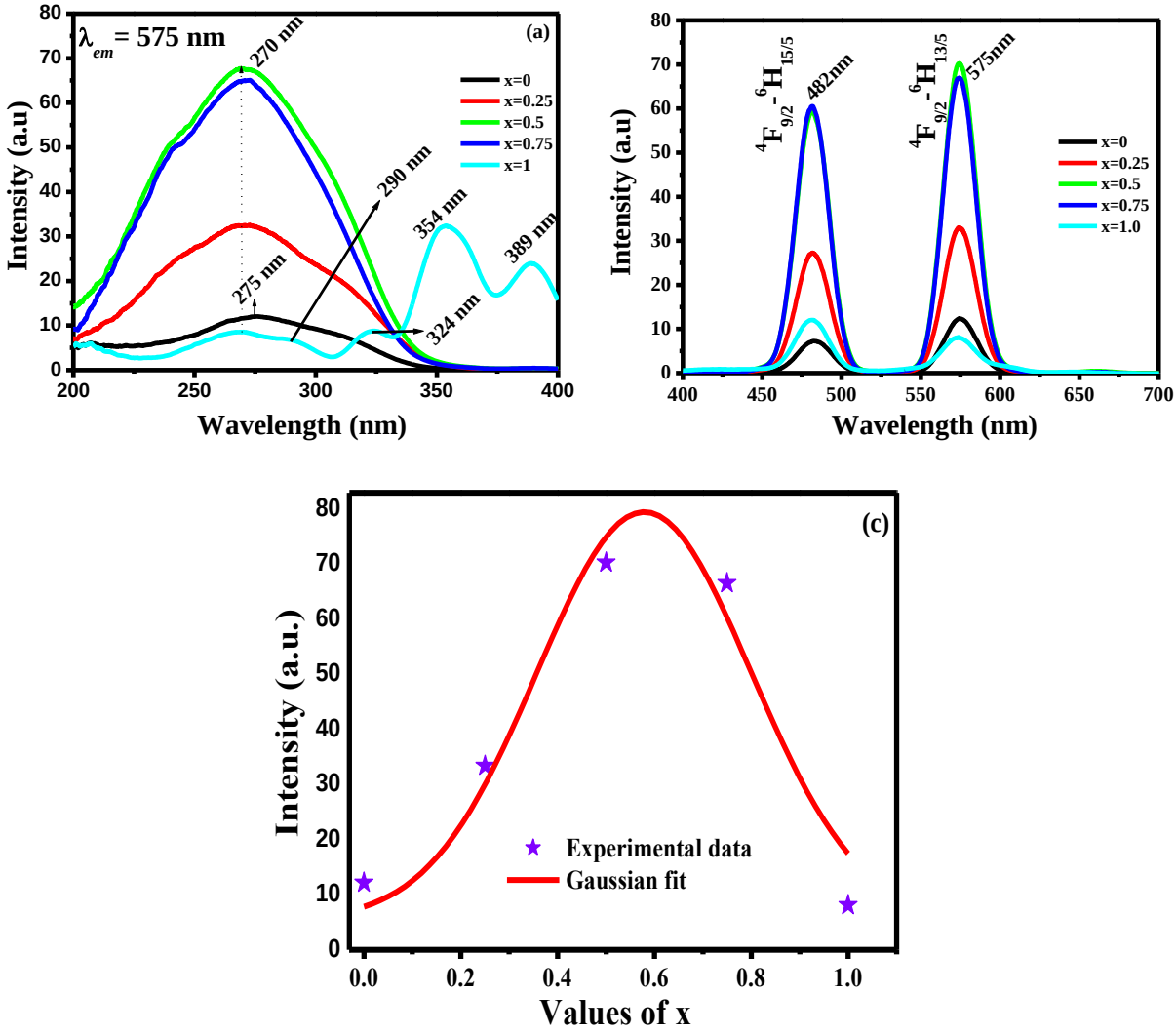

Figure 7.5. *(a) Excitation and (b) Emission spectra of $LaV_{1-x}P_xO_4$: Dy^{3+} (c) A plot showing the intensity as a function of x values.*

The excitation spectra of $LaV_{1-x}P_xO_4$: 1 mol % Sm^{3+} measured at the emission wavelength of 601 nm is shown in figure 7.6(a). The spectra exhibit the strong broad band positioned in the wavelength region between 200 and 350 nm with the maximum at ~ 270 nm. The emission spectra (figure 7.6(b)) were measured at an excitation wavelength of 270 nm. It is clear from the spectra that all the samples, except for x = 1.0, follow similar trend. These spectra consist of three emission peaks at 560, 601 and 650 nm. The dominant peak at 601 nm (red) can be attributed to $^6G_{5/2}$ — $^6H_{7/2}$ transition of Sm^{3+}. The other two peaks at 560 nm (yellow) and 650 nm (red) correspond to $^6G_{5/2}$ — $^6H_{5/2}$ and $^6G_{5/2}$ — $^6H_{9/2}$ of Sm^{3+} transitions respectively. All

these transitions are in the visible range of the spectrum. Because there exist interesting combination of colors, the prepared phosphor powders give a tunable emission from orange to red light.

Figure 7.6(c) gives the relative emission intensity as a function of *x* values. It can be observed from the graph that, the intensity increases with an increase in the value of *x* with the highest intensity at *x* = 0.25. When the value of *x* was further increased, the intensity decreases and this clearly indicate that further addition of P content result in a luminescent quenching.

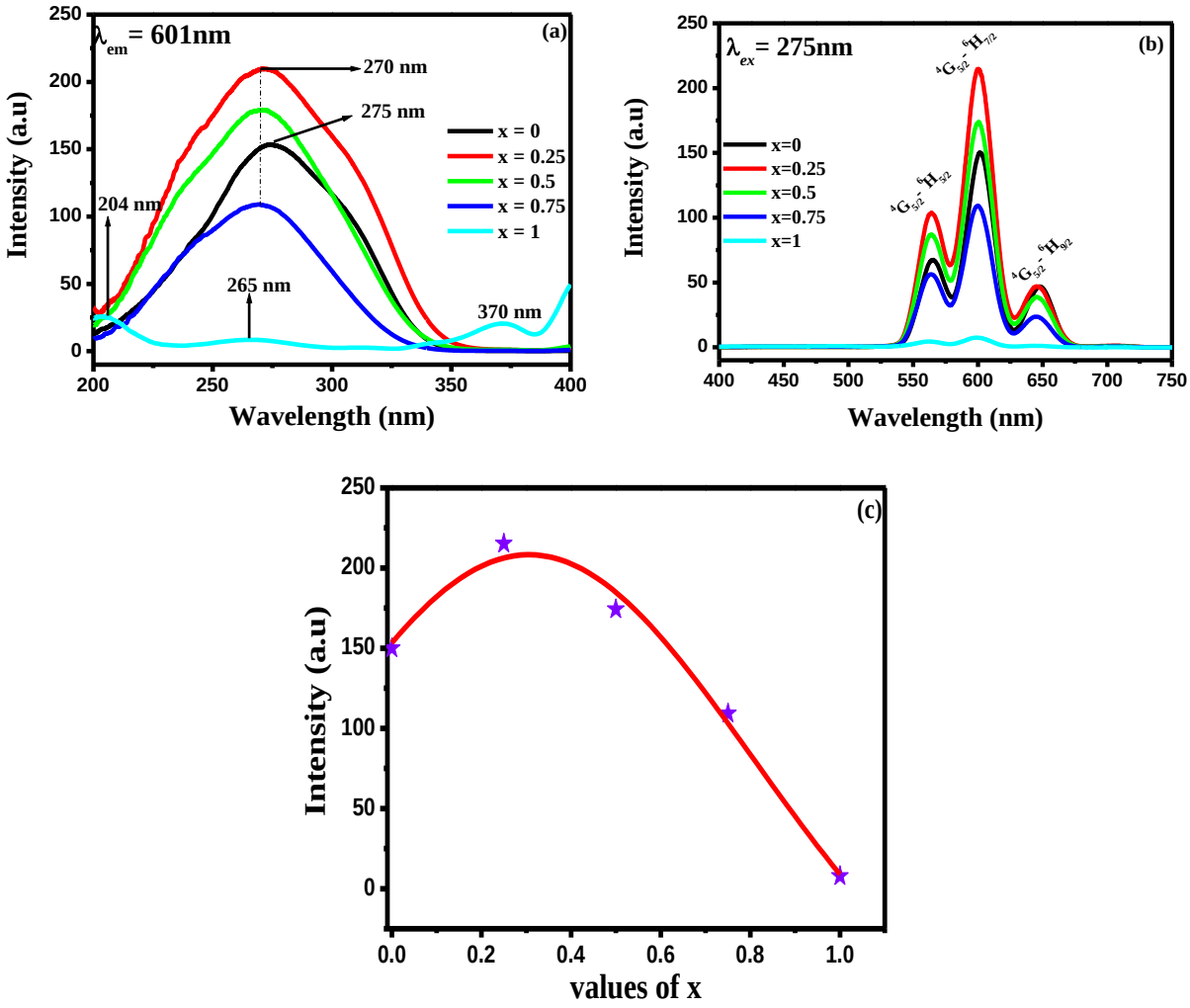

Figure 7.6. *(a) Excitation and (b) Emission spectra of* $LaV_{1-x}P_xO_4:Sm^{3+}$ *(c) A plot showing the intensity as a function of x values.*

The emission spectra (Figure 7.7(b)) exhibit four emission peaks at 490 nm ($^5D_4$—$^7F_6$), 540 nm ($^5D_4$—$^7F_5$), 580 nm ($^5D_4$—$^7F_4$) and 625 nm ($^5D_4$—$^7F_3$) due transitions of Tb^{3+} ions. It can clearly be observed that the most intense peak is from the green emission wavelength ($^5D_4$ — $^7F_5$). There is no noticeable change in the emission spectra when the value of *x* is increased except for intensities which appear to be slight different. Figure 7.7(c) presents the relative emission intensity as a function of *x* values. As shown in the figure, as the value of *x* increases, the intensity also increases whereby the optimum is mainly reached when *x* = 0.75. If the value of *x* is further increased the intensity starts to decrease. Thus, addition of P content results in a luminescence quenching.

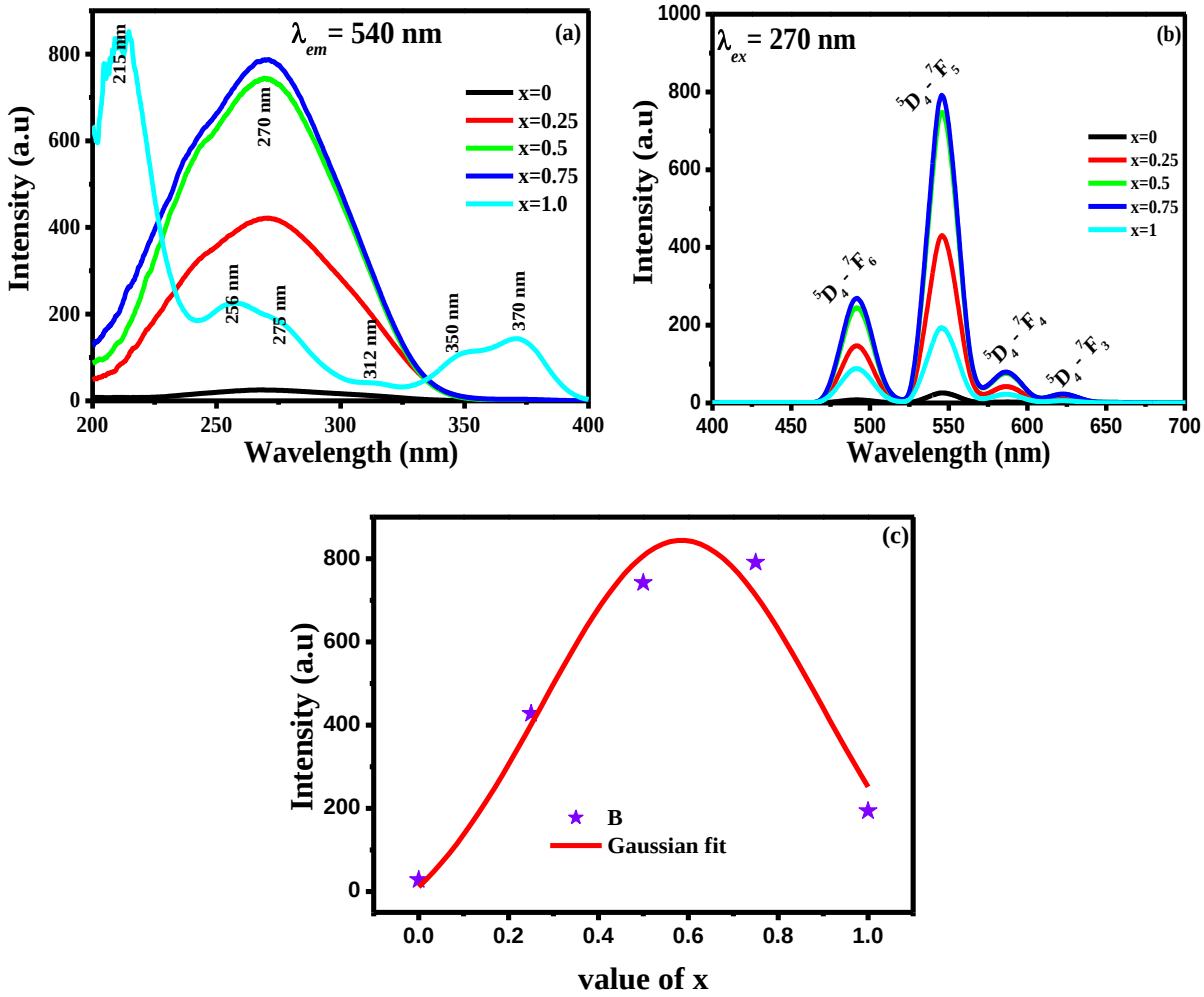

Figure 7.7. *(a) Excitation and (b) Emission spectra of $LaV_{1-x}P_xO_4$: Tb^{3+} (c) A plot showing the intensity as a function of x values.*

7.5 Conclusions

In summary, the $LaV_{1-x}P_xO_4$: Ln^{3+} (Ln = Dy, Sm, and Tb) phosphor powders were successfully prepared by the solution combustion method. The XRD and TEM results show that the prepared phosphor powder has small crystallite size and it is well crystalline. Furthermore, the results for sample with $x = 0.5$, the XRD peaks were found to be intermediate between $LaVO_4$ and $LaPO_4$. The SEM and TEM results show that the prepared phosphor powder is less agglomerated and consisted of various shapes and sizes. The UV-vis room temperature diffuse reflectance show that the powder absorbs in the uv range. The photoluminescence results show the characteristic peaks of Dy, Sm and Tb. The emission intensity is greatly dependent on the value of *x*.

7.6 References

1. Grätzel M, *Accounts of Chemical Research* 42 (2009) 1788−1798
2. Chou CS, Huang YH, Wu P, Kuo YT, *Applied Energy* 118 (2014) 12–21
3. Tigreros A, Dhas V, Ortiz A, Insuasty B, Martín N, Echegoyen L, *Solar Energy Materials and Solar Cells* 121 (2014) 61–68
4. Balasingam SK, Lee M, Kang MG, Jun Y, *Chem. Commun.*, 49 (2013) 1471−1487
5. Kuo HP, Wu CT, *Solar Energy Materials and Solar Cells* 120 (2014) 81–86
6. Zahedifar M, Chamanzadeh Z, Mashkani SMH, *J. lumen.* **135** (2013) 66−73
7. Chamanzader Z, Zahedifar M, Hosseinpoor SM, *Proceding of the 4th international conference on nanostructures (ICNS4)* (2012), Kish Island, I.R Iran
8. Dandan WU, Yongqing MA, Xian Z, Shibing Q, Ganhong Z, Mingzai WU, Guang LI, Zhaoqi S, *J. Rare Earths*, 30 (4) (2012) 325 − 329
9. Motloung SJ, Shaat SKK, Tshabalala KG, Ntwaeaborwa OM, *J. Biol. Chem. Lumin.* 31 (2016) 1069 – 1076
10. Wang X, Wang X, Liu W, Liu C, Zhang Z, *Opt. Mater.* 36 (2014) 1506 −1510
11. Park SW, Yang HK, Chung JW, Chen Y, Moon BK, Choi BC, Jeong JH, Kim JH, *Phys. B. 405 (2010) 4040 − 4044*
12. Su LM, Fan X, Cai G. M, Jin ZP, *RSC Adv.* 7 (2017) 22156 − 22169

Chapter 8 Effect of annealing temperature on the structure and optical properties of lanthanum rare earth doped phosphovanadate

8.1 Introduction

Orthovanadates are technologically important materials with variety applications in existing and future technologies. Recently they have attracted considerable attention due to potential applications in renewable energy and alternative green technology [1]. Lanthanide orthovanadates ($LnVO_4$) specifically, have been under vigorous investigation due to their wide range of applications [2]. $LaVO_4$ as a member of this family crystallizes in two polymorphs, namely, monoclinic (*m*-) monazite type and tetragonal (*t*-) zircon type [3, 4]. On the other hand, lanthanide phosphates ($LnPO_4$) have also attracted much attention due to their novel promising applications in several fields of science and technology [5]. Among the many $LnPO_4$ phases, $LaPO_4$ stands out for its broader range of applications in different areas of technological interest [6] and it is a useful host for doping rare earth ions with high quantum efficiencies [7]. Moreover, it presents many outstanding properties, including high insolubility, reliable stability against high temperatures and energy excitations, low toxicity and high quantum yield [8].

Unlike $LaVO_4$, lanthanide orthophosphate ($LaPO_4$), one member of rare earth orthophosphate family, exhibit five kinds of polymorphs: monazite (monoclinic, naturally abundant), xenotime (tetragonal, naturally abundant), rhabdophane (hexagonal), weinschenkite (monoclinic), and orthorhombic [9]. Systems of orthovanadate and orthophosphate are very important hosts for the luminescence of lanthanide ions [10]. A mixture of orthovanadate and orthophosphate form a multicomponent system called phosphovanadate.

The applicability of luminescent devices depends on the luminescence intensity [11]. Therefore, the improvement of the emission intensity of luminescence materials is an important aspect that greatly affects the performance of light absorbance on different display and solar cell materials. For sufficient brightness in display devices and energy conversion in solar cells these devices require phosphor materials with high emission intensities [12]. Structural characteristics, such as particle morphology, structure, and surface chemical composition of samples, have significant effects on physicochemical properties, which can be tuned in a controllable manner to tailor their mechanical, thermal, photoluminescence (PL), and electrical properties [13]. Thus, there is an urgent demand of improving luminescent efficiency of nanomaterials, which may be affected by two fundamental factors: crystallinity and surface effect [14]. Insufficient crystallinity means unordered structure and more defects which act as quenching centres consuming excited photoelectrons without any radiation being observed.

Lastly, the large specific surface area of nanomaterials, unsaturated bonds on the surface and high surface energy will result in surface quenching and greatly decrease the lifetime and luminescent efficiency of nanomaterials [14]. Nevertheless, one method of improving the effect on crystallinity, and therefore luminescence, is to follow a high temperature annealing process. Thus, it is important to know how thermal treatment influence the luminescence properties of a specific material for specific purpose. In this chapter, the influence of annealing temperature on the structure and luminescent properties of Ln^{3+} (Ln = Dy, Sm, Tb) activated lanthanum phosphovanadate synthesized by solution combustion method is investigated. The results obtained suggest that these materials can be used as down converters in dye sensitized solar cells.

8.2 Experimental details

The multi-component systems of $LaV_{0.25}P_{0.75}O_4$: 1 mol % Dy^{3+}, $LaV_{0.25}P_{0.75}O_4$: 1 mol % Tb^{3+} and $LaV_{0.75}P_{0.25}O_4$: 1 mol % Sm^{3+} were synthesized by solution combustion method. The starting materials included AR grade 99.99% lanthanum (III) nitrate hexahydrate ($La(NO_3)_3.6H_2O$), ammonium metavanadate (NH_4VO_3), ammonium phosphate ($NH_4H_2PO_4$), urea (CH_4N_2O), samarium nitrate hexahydrate ($Sm(NO_3)_3.6H_2O$), terbium nitrate hexahydrate ($Tb(NO_3)_3.6H_2O$) and dysprosium nitrate hydrate ($Dy(NO_3)_3.\ xH_2O$), which were dissolved in de-ionized water in appropriate weights to form the necessary precursor solutions. The solutions were kept on a magnetic stirrer until a homogeneous mixture was achieved. The resulting brownish solutions were then transferred into different crucibles and placed one-by-one into a preheated furnace set at 600 ± 10 ^oC. As a result of exothermic reactions that took place, the final products were fluffy ashes. The resulting combustion ashes were annealed at different temperatures, for two hours, and also were manually ground using pestle and mortar to obtain a very fine powder ready for characterization.

On the structure and phase identification, the phosphor powder samples prepared were characterized by X-ray diffraction (XRD) Siemens D5000 powder Diffractometer. The X-ray radiation used during the measurement was a CuKα source (λ= 1.5406 Å). Photoluminescence data were recorded using a Hitachi F7000 fluorescence spectrophotometer. The morphology and elemental composition of the materials were obtained using Jeol JSM-7800F field emission scanning electron microscope (FE-SEM) fitted with Oxford Aztec 350 X-Max80 energy-dispersive X-ray spectroscopy (EDS).

8.3 Results and discussion

8.3.1 X-ray diffraction (XRD)

The phase structure, purity and crystallinity of the prepared powder phosphors were investigated by XRD. Figure 8.1 (a) shows the XRD pattern of $LaV_{0.25}P_{0.75}O_4$: 1 mol % Tb^{3+} powder phosphors annealed at the temperature of 1000°C for 2 hours. The XRD spectrum for the sample prepared at 600°C shows that all the peaks can be easily indexed to that of $LaPO_4$ (JCPSD file no. 75 − 1881) and this suggests that $LaV_{0.25}P_{0.75}O_4$ is a single phase and crystallizes in a hexagonal structure. The diffraction peaks for this host seem to be slightly shifted towards higher angles, and this might be due to different ionic radii of vanadium (0.059 nm) [15] and phosphorus (0.034 nm) [15]. Moreover, the results indicate that the powder phosphors are highly crystalline and the diffraction peaks are broadened which is an indication that the prepared samples have small crystallite size. The results further indicate that the structure of the prepared powder changes from hexagonal to monoclinic structure (JCPDS file no. 35 − 0731) with increasing annealing temperature (figure 8.1 (b)). Lastly, the crystallite sizes were then estimated from Scherrer's equation 8.1:

$$D = \frac{k\lambda}{\beta \cos\theta} \qquad 8.1$$

where D is the crystallite size, λ is the wavelength of the x-ray radiation (1.5418Å), β is the full width at half maximum intensity and θ is the diffraction angle at the peak position. The estimated crystallite sizes of $LaV_{0.25}P_{0.75}O_4$: 1 mol % Dy^{3+}, $LaV_{0.25}P_{0.75}O_4$: 1 mol % Tb^{3+} and $LaV_{0.75}P_{0.25}O_4$: 1 mol % Sm^{3+} respectively, are tabulated in table 8.1. The results indicated that the size increases with an increase in annealing temperature except for the sample, $LaV_{0.25}P_{0.75}O_4$: 1 mol % Dy^{3+}, annealed at 1000°C, which shows a decrease in crystallite size.

This is consistent with the results reported by [16, 17, 18]. The XRD patterns for Dy^{3+} and Sm^{3+} doped samples show similar features to Tb^{3+} doped sample and therefore they are not included here.

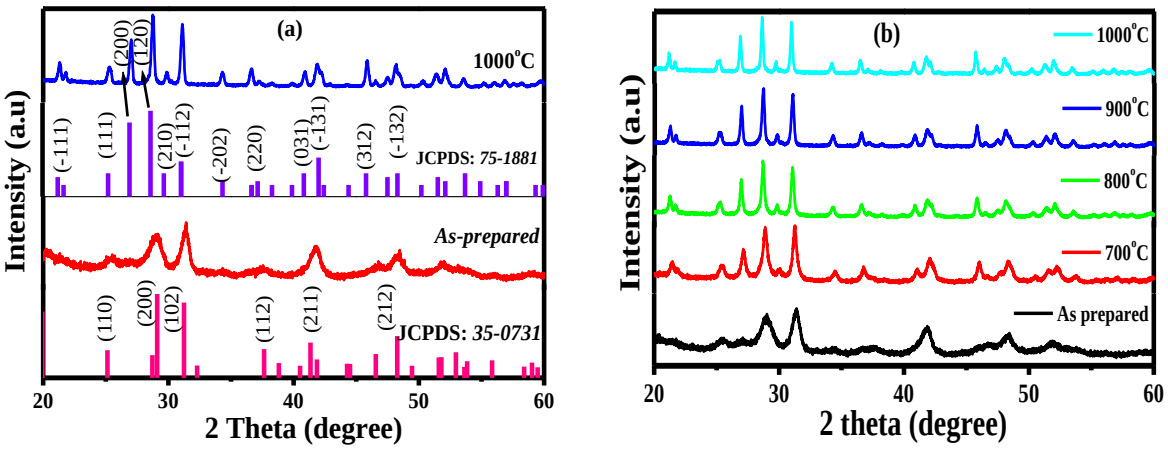

Figure 8.1. *XRD patterns of $LaV_{0.25}P_{0.75}O_4$: 1 mol % Tb^{3+} and JCPDS's of phosphor powder annealed at different temperatures.*

Table 8.1. *A table showing annealing temperature as a function of crystallite size.*

Temperature	**$LaV_{0.25}P_{0.75}O_4$: Dy^{3+}**	**$LaV_{0.75}P_{0.25}O_4$: Tb^{3+}**	**$LaV_{0.25}P_{0.75}O_4$: Sm^{3+}**
(^oC)	**D (*nm*)**		
600	11.36	11.28	19.82
700	18.46	21.07	18.92
800	38.05	24.23	36.49
900	42.27	30.31	39.19
1000	37.12	43.75	48.09

8.3.2 Scanning electron microscopy

The surface morphology and the elemental analysis of the prepared powder samples were investigated using SEM and EDS. Figure 8.2 shows SEM images of (a) $LaV_{0.25}P_{0.75}O_4$: 1 mol % Dy^{3+}, (c) $LaV_{0.25}P_{0.75}O_4$: 1 mol % Tb^{3+} and (e) $LaV_{0.75}P_{0.25}O_4$: 1 mol % Sm^{3+}. The micrographs

from Dy^{3+} and Tb^{3+} activated powder samples (Fig. 8.2 *a* and *c*) revealed that, although the powder is not evenly distributed, but it is less agglomerated and composed of various shapes, mostly spheres, and random sizes. However, the micrographs for Sm^{3+} activated powder sample (Fig. 8.2 *e*) indicated that the sample consisted of 3 dimensional hexagonal and spherical shaped structures of different lengths and sizes. Figure 8.2 show the EDS spectra of (b) $LaV_{0.25}P_{0.75}O_4$: 1 mol % Dy^{3+}, (d) $LaV_{0.25}P_{0.75}O_4$: 1 mol % Tb^{3+} and (f) $LaV_{0.75}P_{0.25}O_4$: 1 mol % Sm^{3+}. In each case, the elements forming the compound are all observed. The spectra for Tb^{3+} and Sm^{3+} doped samples (Fig 8.2 *d* and *f*), a trace of carbon element is observed. This is believed to have come from the carbon tape used to mount the powder.

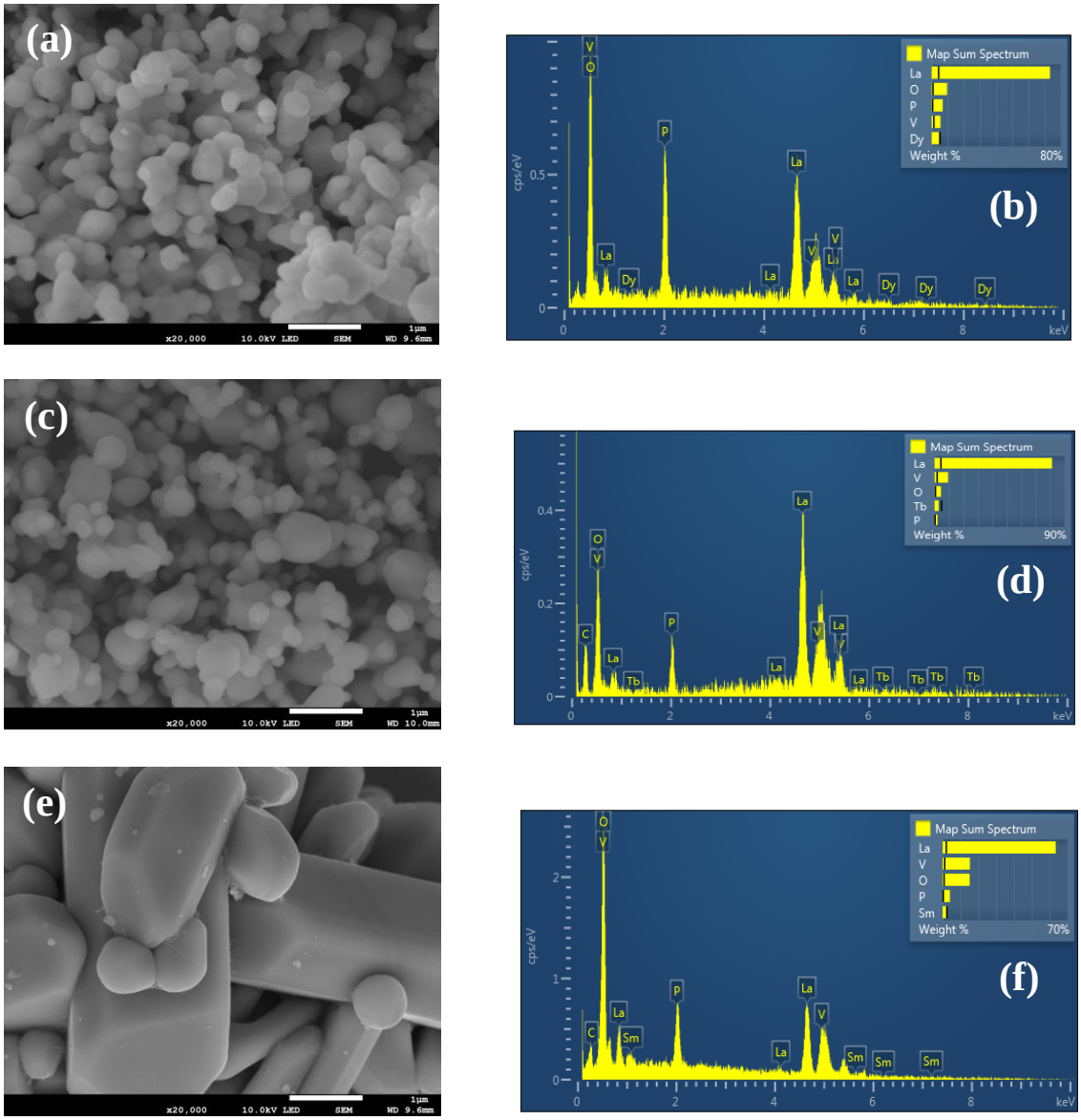

Figure 8.2. *SEM images and EDS spectra of (a) $LaV_{0.25}P_{0.75}O_4$: 1 mol % Dy^{3+}, (b) $LaV_{0.25}P_{0.75}O_4$: 1 mol % Tb^{3+} and (c) $LaV_{0.75}P_{0.25}O_4$: 1 mol % Sm^{3+}.*

8.3.3 FTIR analysis

FTIR spectroscopic measurements were performed in order to determine the different functional groups in the prepared powder samples. The FTIR spectra of La system is presented in figure 8.3. It can be clearly observed that all the samples exhibit the same trend with characteristic peaks at wavelengths 789 nm (V–O stretching vibrations), 988 nm (V–O stretching vibrations), 1420 nm (O–H bending vibrations), 1629 nm and 3446 nm (H–O–H)

respectively [19, 20]. The FTIR results further revealed that the samples annealed at 1000ºC indicate that the O–H and/or H–O–H bending vibrations observed in the as prepared samples has disappeared completely.

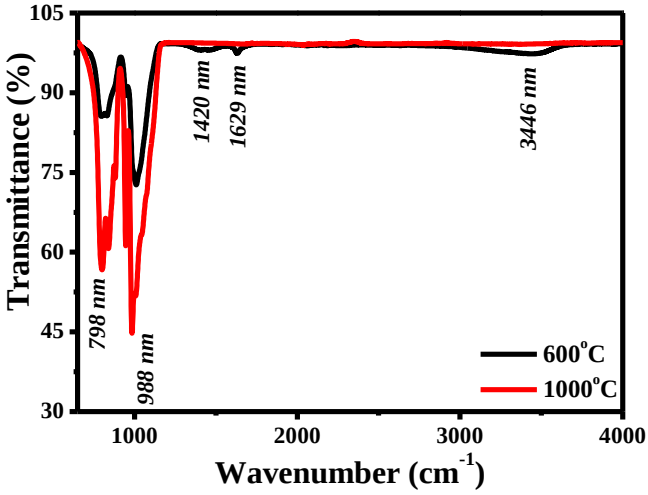

Figure 8.3. *FTIR spectrum of $LaV_{0.25}P_{0.75}O_4$: 1 mol % Tb^{3+} phosphor powder*.

8.3.4 Photoluminescence

Figures 8.4(a), 8.5(a) and 8.6(a) exhibit the excitation spectra of $LaV_{0.25}P_{0.75}O_4$: 1 mol % Dy^{3+}, $LaV_{0.25}P_{0.75}O_4$: 1 mol % Tb^{3+} and $LaV_{0.75}P_{0.25}O_4$: 1 mol % Sm^{3+} powder samples obtained by monitoring the emission wavelengths at 573, 546 and 601 nm respectively. All these three spectra exhibit the same trend showing a strong broad band between 200 and 350 nm with maximum at ~ 270 nm. Thus, the maximum band is attributed to charge transfer from oxygen ligands to the central vanadium, phosphorus atom(s) inside $[VO_4]^{3-}$ ion(s) [21].

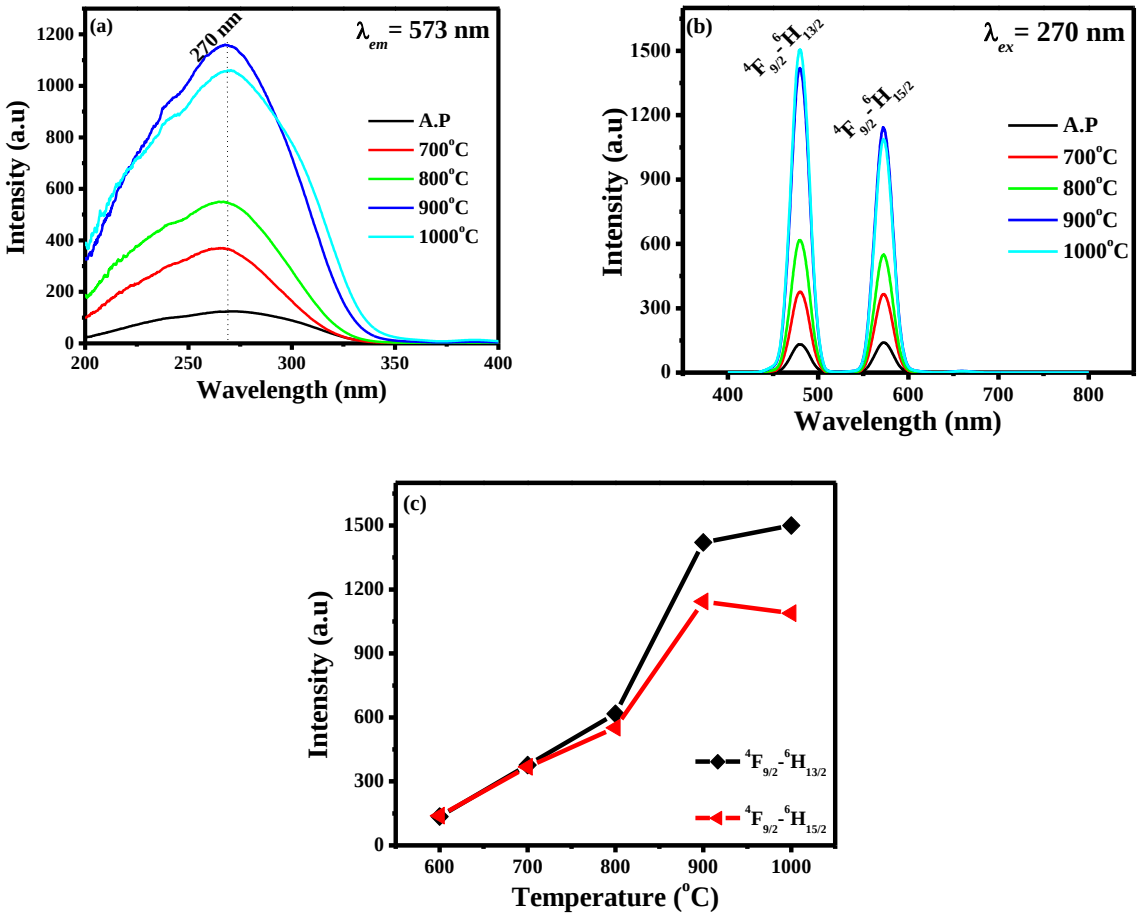

Figure 8.4. *(a) Excitation and (b) Emission spectra of $LaV_{0.25}P_{0.75}O_4$: 1 mol % Dy^{3+} (c) A plot showing the relative emission intensity as a function of annealing temperature.*

The emission spectra of $LaV_{0.25}P_{0.75}O_4$: 1 mol % Dy^{3+}, $LaV_{0.25}P_{0.75}O_4$: 1 mol % Tb^{3+} and $LaV_{0.75}P_{0.25}O_4$: 1 mol % Sm^{3+} powder samples obtained by monitoring the excitation wavelength at 270 nm are shown in figures 8.4(b), 8.5(b) and 8.6(b). Two relatively strong emission peaks at the wavelengths of 479 and 573 nm are observed for Dy activated sample. These peaks are attributed to the emissions associated with the ($^4F_{9/2}$ — $^6H_{15/2}$) and ($^4F_{9/2}$ — $^6H_{13/2}$) transitions of Dy^{3+} respectively. The emission intensities ($^4F_{9/2}$ — $^6H_{15/2}$ and $^4F_{9/2}$ — $^6H_{13/2}$) were found to increase with an increase in annealing temperature as shown in figure 4(c). Further increase in annealing temperature to 1000°C, led to the decrease in the emission intensity of $^4F_{9/2}$ — $^6H_{13/2}$. The spectra for singly doped Tb activated powder samples show four emission peaks at 490, 546, 585 and 622 nm,

and they are assigned to $^5D_4 \rightarrow {}^7F_j$ (*j = 6, 5, 4 and 3*) transitions of Tb^{3+} ion. Figure 8.5(c) shows a plot of a relative emission intensity of the prominent peak $^5D_4 \rightarrow {}^7F_5$ as a function of annealing temperature.

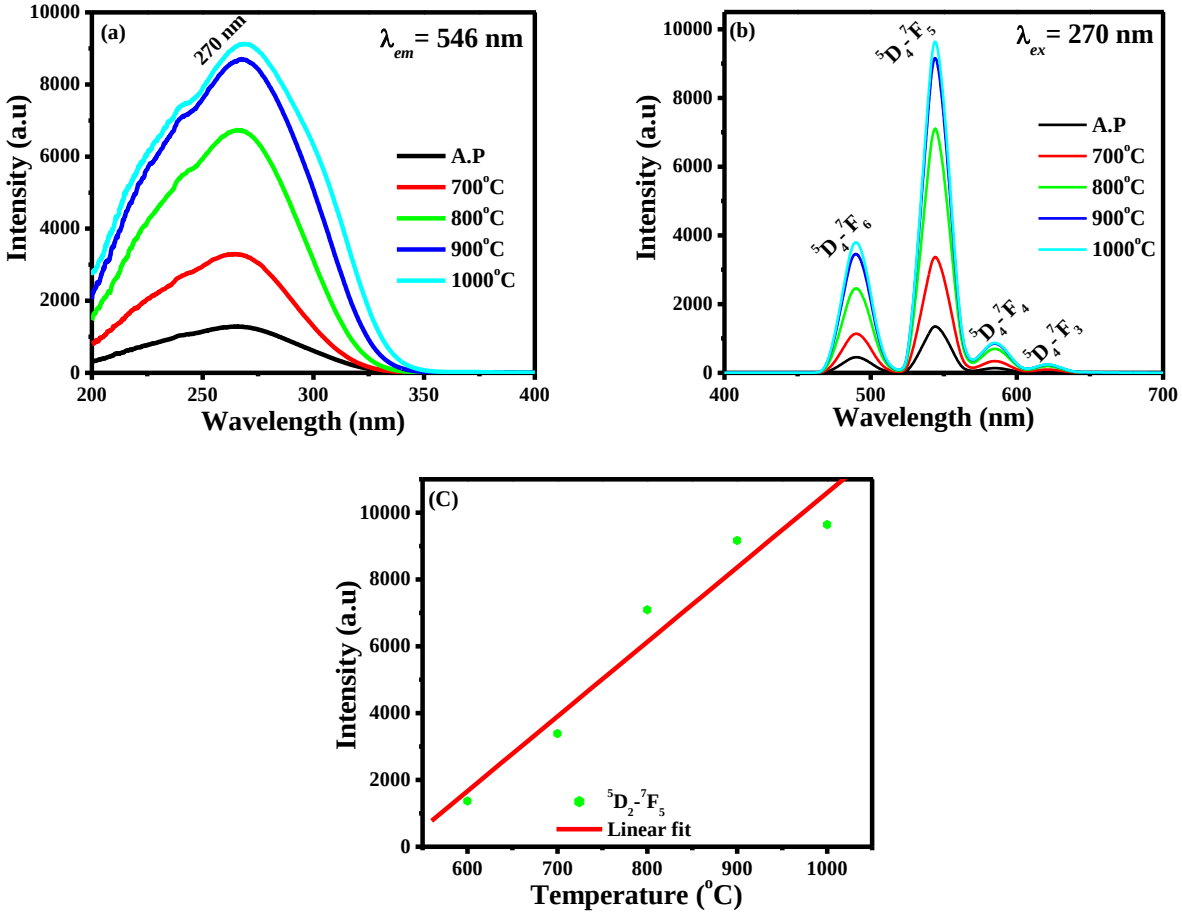

Figure 8.5. *(a) Excitation and (b) Emission spectra of $LaV_{0.25}P_{0.75}O_4$: 1 mol % Tb^{3+} (c) A plot showing the relative emission intensity as a function of annealing temperature.*

Evidently, from the graph, the intensity increases with an increase in annealing temperature. The emission spectra of Sm activated samples show three bands at 562, 601 and 645 nm respectively. These bands are assigned to ($^6G_{5/2}$ — $^6H_{5/2}$), ($^6G_{5/2}$ — $^6H_{7/2}$) and ($^6G_{5/2}$ — $^6H_{9/2}$) transitions of Sm^{3+} respectively. Figure 8.6(c) shows the plot of a relative emission intensity versus annealing temperature. The intensity of the emission band was found to increase with an increase in annealing temperature until 700°C, such that with any further increase in annealing temperature resulted in the decrease in the emission intensity like in case of Dy activated sample.

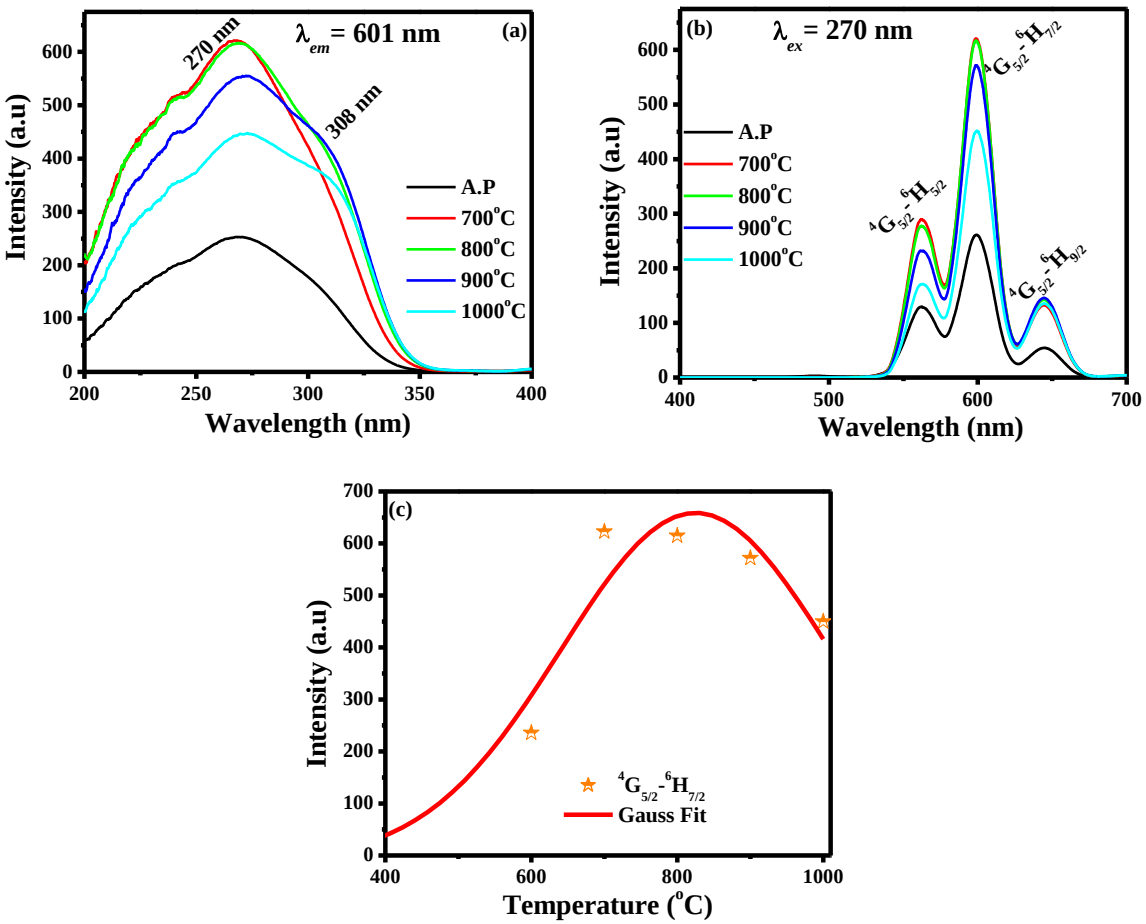

Figure 8.6. *(a) Excitation and (b) Emission spectra of* $LaV_{0.75}P_{0.25}O_4$*: 1 mol %* Sm^{3+} *(c) A plot showing the relative emission intensity as a function of annealing temperature.*

8.4 Conclusions

Ln^{3+} (Dy, Sm, Tb) doped lanthanum ortho-phosphovanadate phosphor powders were successfully synthesized by solution combustion method. XRD confirmed the formation of $LaV_{0.25}P_{0.75}O_4$: 1 mol % Dy^{3+}, $LaV_{0.25}P_{0.75}O_4$: 1 mol % Tb^{3+} and $LaV_{0.75}P_{0.25}O_4$: 1 mol % Sm^{3+} compounds. The results further indicated that the structure changed with annealing temperature from monoclinic to tetragonal. SEM images revealed that the powder consisted of different shapes and non-uniform sizes. The excitation spectra showed that all the systems can be excited with UV radiation. Furthermore, it is observed that under ultraviolet excitation, the prepared phosphor powders displayed characteristic emissions of Dy, Sm and Tb. The annealing temperature was found to increase the luminescence intensity.

8.5 References

1. Errandonea D. Popescu C. Achary SN, Tyagi AK, Bettinelli M, *Mater. Res. Bull.* 50 (2014) 279–284
2. Wang LP, Chen LM, *Mater. Charac.* 69 (2012) 108 – 114
3. Salavati-Niasari M, Saleh L, Mohandes F, Ghaemi A, *Ultrason Sonochem.* 21 (2014) 653–662
4. Park SW, Yang HK, Chung JW, Chen Y, Moona BK, Choi BC, Jeong JH, Kim JH, *Physica B* 405 (2010) 4040–4044
5. Nunez NO, LivianoSR, Ocana M, *J. Coll. and Inter. Scie.* 349 (2010) 484–491
6. Colomer MT, Mosa J, *Ceram. Inter*. 41 (2015) 8080 – 8092
7. Hou D, Guo X, Liu C, Sham TK, Liang H, Gao J, Sun X, Zhang B, Zhan F, Huan Y, Tao Y, *J. Lumin*. 165 (2015) 23–29
8. Wang X, Wang X, Zheng X, Zhang L, *J. Alloys Compd.* 632 (2015) 269–273
9. Huang X, *Opt. Mater.* 50 (2015) 81–86
10. Yu M, Lin J, Zhou YH, Pang ML, Han XM, Wang SB, *Thin Solid Films* 444 (2003) 245–253
11. Yang Y, Ding M, Song G, Fan W, Feng H, *Chem. Phys. Lett.* 639 (2015) 67–70
12. Jafer RM, Swart HC, Yousif A, Kumar V, Coetsee E, *J. Lumin.* 180 (2016) 198–203
13. Zhou R, Meng L, Li X, *Opt. Mater*. 51 (2016) 89 – 93
14. Xie D, Peng H, Huang S, You F, Zhang X, Wang G, *Mater. Lett.* 157 (2015) 307–310
15. Sun J, Xian J, Xia Z, Du H, *J. Lumin*. 130 (2010) 1818–1824
16. Rath H, Anand S, Mohapatra M, Dash P, Som T, Signh UP, Mishra NC, *Indian J. Phys.* 83 (4) (2009) 559 - 565
17. Malevu TD, O Ocaya R, *Int. J. Electrochem. Sci.,* 10 (2015) 1752 −1761

18. Basar K, Siagian S, Ohara K, Sakuma TI, Takahashi H, Abe O, Igawa NI, Ishii Y, *Indonesian J. Phys.* 20 (2009) 9 − 12
19. Niu N, Yang P, Wang Y, Wang W, He F, Gai S, Wang D, *J. Alloys compd*. 509 (2011) 3096 – 3102
20. Mei Y, You H, Liang Y, Xu J, Lu F, Dai L, Lui Y, *J. Alloys compd*. 582 (2014) 603 – 608.
21. Motloung SJ, Shaat SKK., Tshabalala KG, Ntwaeaborwa OM, *J. Biol. Chem. Lumin.* 31 (2016) 1069 – 1076

Chapter 9 Combustion synthesis and characterization of $MV_{0.5}P_{0.5}O_4$: Sm^{3+}, Tm^{3+} (M = Gd, La, Y)

Physica B, 2017 (*accepted*)

9.1 Introduction

Rare earth orthovanadates with general formula MVO_4 have been extensively studied for a long time. Gadolinium (Gd^{3+}), lanthanum (La^{3+}) and yttrium (Y^{3+}) orthovanadates are very interesting material in scientific world. This is due to their diverse range of applications. Gadolinium orthovanadate ($GdVO_4$) is considered as an excellent host lattice for lasers due to its outstanding chemical stability, higher thermal conductivity, larger emission cross-section, and larger absorption cross-section [1, 2]. Lanthanum orthovanadate ($LaVO_4$), on the other hand, is significant for its wide potential applications as anode material in lithium ion batteries, ferroelectrics, a host lattice for lasers, and a host lattice for light emitting materials (phosphors) [3]. Yttrium orthovanadate (YVO_4) is an important oxide in material science and technology and has been extensively used as a source of light in applications such as field emission displays (FEDs), cathode ray tubes (CRTs), and plasma display panels (PDPs) [4].

Lately, rare earth orthophosphates have generated interest due to their potential applications in various areas [5]. Recent investigations proved that $LnPO_4$ phosphors are promising candidates for backlit liquid crystal displays (LCDs), plasma display panels (PDPS), field emission displays (FEDs), and new generation fluorescent lamps [6] among other things. Lanthanum orthophosphate $LaPO_4$, in particular, is a potential host lattice for phosphor materials that can efficiently absorb the energy in the vacuum ultraviolet (VUV) region and can be applied in the mercury-free fluorescent lamps and plasma display panels [7]. Gadolinium orthophosphates ($GdPO_4$) co-doped with different types of luminescing ions have potential use as red, orange or green phosphors for ultra-violet light emitting diodes because of their intense excitation spectra in the ultraviolet region, solar spectrum conversion, IR sensor etc. [8]. Also, recent

investigations have proved that yttrium orthophosphate YPO_4 is one of promising candidates for PDP applications because of its high absorption and luminescence efficiencies in the vacuum ultra-violet (VUV) region [9].

The ultimate goal of this work was to prepare and characterize rare earth activated lanthanide phosphovanadate. This system (phosphovanadate), as it is mentioned in chapter 4, is a combination of two systems, namely, orthophosphate ($LnPO_4$) and orthovanadate ($LnVO_4$) that are mixed together [10]. Several synthesis methods including solid-state method [11], hydrothermal synthesis [12] and co-precipitation [13], among others, have been used to prepare these systems.

In this study, a solution combustion method was used to prepare the $GdV_{0.5}P_{0.5}O_4$: Sm^{3+}, Tm^{3+}, $LaV_{0.5}P_{0.5}O_4$: Sm^{3+}, Tm^{3+} and $YV_{0.5}P_{0.5}O_4$: Sm^{3+}, Tm^{3+} powder phosphors. This method was chosen because of its cost effectiveness, time saving and straightforwardness. The structure, surface morphology and optical properties were investigated. The ultimate goal of this work is to prepare phosphor materials that can be used as down converters in dye sensitized solar cells (DSSCs). Ultraviolet light usually degrades the organic dyes in DSSCs, furthermore, the quantum efficiency of DSSCs in the ultraviolet wavelength range is relatively lower than in the visible light wavelength range [14]. Therefore, it is of great importance to coat DSSCs with materials that will harvest ultraviolet light and re-emit visible light. We will not report on the application of these materials in DSSCs.

9.2 Experiment

9.2.1 Materials

The following starting materials: Gadolinium nitrate hexahydrate ($Gd(NO_3)_3.6H_2O$), Lanthanum nitrate hexahydrate ($La(NO_3)_3.6H_2O$), Yttrium nitrate hexahydrate ($Y(NO_3)_3.6H_2O$), ammonium metavanadate (NH_4VO_3), ammonium phosphate ($NH_4H_2PO_4$), Samarium nitrate hexahydrate ($Sm(NO_3)_3.6H_2O$), thulium nitrate hexahydrate ($Tm(NO_3)_3.6H_2O$) and urea (CH_4N_2O) were used as starting materials. All chemicals were of analytical grade and were used without further purification.

9.2.2 Synthesis

Samarium and thulium co-activated $GdV_{0.5}P_{0.5}O_4$ phosphors were synthesized by solution combustion method using urea as a fuel. In a typical preparation, stoichiometric amounts of $Gd(NO_3)_3.6H_2O$, NH_4VO_3, $NH_4H_2PO_4$, $Sm(NO_3)_3.6H_2O$, $Tm(NO_3)_3.6H_2O$ and urea were dissolved in deionized water. The molar concentrations of Sm^{3+} and Tm^{3+} were kept at 1 and 1.5 mol % respectively, for all the samples. After vigorous stirring, a pale yellow homogeneous solution was obtained. The solution was then transferred into a muffle furnace where the preparation temperature was set at 600 ± 10 ^oC. Due to this high temperature, the water evaporated and the reagents decomposed and released large amount of gases. The resulting combustion ashes were allowed to cool down in air to room temperature and were ground gently using pestle and mortar. Finally, the synthesized powders were annealed at 900 ^oC for 2 hours in air, and they were ready for characterization. The same procedure was used for the preparation of Samarium and thulium co-activated $LaV_{0.5}P_{0.5}O_4$ and $YV_{0.5}P_{0.5}O_4$ respectively.

9.2.3 Characterization

For the structure and phase identification, the powder samples prepared were characterized by XRD (Bruker D8 Advanced Powder Diffractometer). The X-ray radiation used during the measurement was a CuKα source (λ= 1.5406 Å). The morphology and elemental composition of the materials were obtained using Jeol JSM-7800F field emission scanning electron microscope (FE-SEM) fitted with Oxford Aztec 350 X-Max80 energy-dispersive X-ray spectroscopy (EDS). Reflectance spectra were measured using UV-Vis spectrophotometer Lambda 950 (PerkinElmer). The photoluminescence data were recorded using a Hitachi F700 fluorescence spectrophotometer.

9.3 Results and discussion

9.3.1 X-ray diffraction

The phase structure, purity and crystallinity of the prepared powder phosphors were investigated by XRD. The XRD pattern of $GdV_{0.5}P_{0.5}O_4$: Sm^{3+}, Tm^{3+} powder phosphor annealed at 900 ^oC for 2 hours is presented in figure 9.1(a) and the peaks are in good agreement with those of tetragonal structure of gadolinium orthovanadate referenced in JCPDS file no. 72-0277. It can also be observed from the figure that all the peaks are slightly shifted towards the higher angles. The shift is possibly due to strains caused by the difference in ionic radii of vanadium (~ 0.54 Å) and phosphorus (~ 0.35 Å) [15]. Figure 9.1(b) shows the XRD pattern of $LaV_{0.5}P_{0.5}O_4$: Sm^{3+}, Tm^{3+} powder phosphor annealed at 900 ^oC for 2 hours. The pattern is indexed to a monoclinic structure referenced in JCPDS file no. 23-0324. The XRD results further reveal that all the peaks have shifted to lower values of 2θ due to stress induced by difference in ionic radii of vanadium and phosphorus. Figure 9.1 (c) gives the XRD pattern of $YV_{0.5}P_{0.5}O_4$: Sm^{3+}, Tm^{3+}. Compared with bulk YVO_4 (JCPDS file no. 17-0341) and YPO_4 (JCPDS file no. 11-0254), the XRD peaks are located in between and this suggest that the

prepared powder phosphor is an admixture of both compounds. It is clear from figure 9.1 (a − c) that the peaks are sharp and slightly broadened, and this is the indication that the prepared powder phosphors are well crystalline and have small crystallite size [16]. The lattice strain and the crystallite sizes were estimated from equation 4.1 and they are tabulated in table 9.1. A plot of $\beta \cos\theta$ as a function of $\sin\theta$ for $GdV_{0.5}P_{0.5}O_4$: Sm^{3+}, Tm^{3+} is presented in figure 9.1(d). The same procedure was used for $LaV_{0.5}P_{0.5}O_4$: Sm^{3+}, Tm^{3+} and $YV_{0.5}P_{0.5}O_4$: Sm^{3+}, Tm^{3+}.

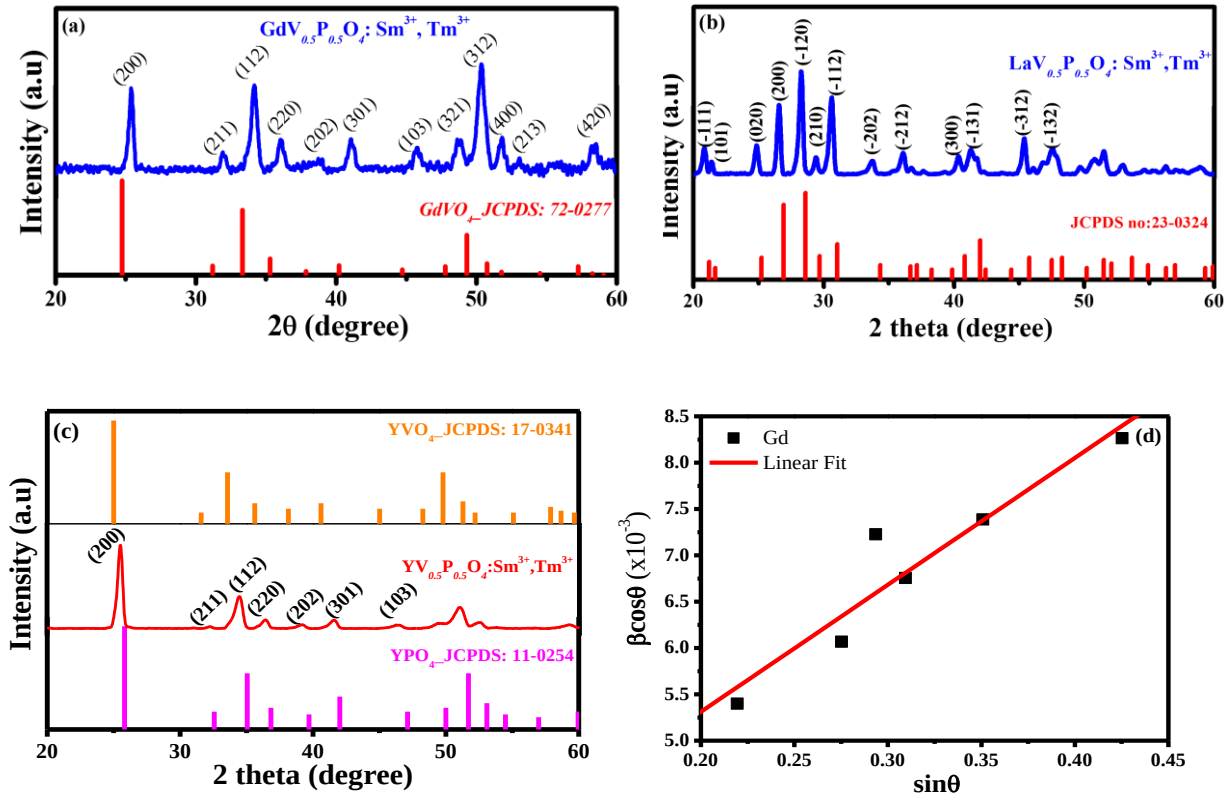

Figure 9.1. *XRD pattern of (a) $GdV_{0.5}P_{0.5}O_4$: Sm^{3+}, Tm^{3+} JCPDS file of $GdVO_4$, (b) $LaV_{0.5}P_{0.5}O_4$: Sm^{3+}, Tm^{3+} and JCPDS file $LaVO_4$ (c) $YV_{0.5}P_{0.5}O_4$: Sm^{3+}, Tm^{3+} powder and JCPDS file. (d) a plot of $\beta \cos\theta$ against $\sin\theta$ of $GdV_{0.5}P_{0.5}O_4$: Sm^{3+}, Tm^{3+}*

Table 9.1: *Lattice strains and average crystallite sizes*

	lattice strain	**Crystallite Size (*nm*)**
$GdV_{0.5}P_{0.5}O_4$: Sm^{3+}, Tm^{3+}	0.014	54.09
$LaV_{0.5}P_{0.5}O_4$: Sm^{3+}, Tm^{3+}	0.001	28.23
$YV_{0.5}P_{0.5}O_4$: Sm^{3+}, Tm^{3+}	0.021	61.23

9.3.2 Scanning electron microscopy

Surface morphologies of the prepared powder samples were investigated using SEM. Figure 9.2 illustrate SEM images of (a) $GdV_{0.5}P_{0.5}O_4$: Sm^{3+}, Tm^{3+} (c) $LaV_{0.5}P_{0.5}O_4$: Sm^{3+}, Tm^{3+} (e) $YV_{0.5}P_{0.5}O_4$: Sm^{3+}, Tm^{3+}. In general, the particles are not evenly dispersed, but they are less agglomerated and composed of mixed shapes, varying from spheres to three dimensional structures of different lengths and sizes. Figure 9.2 shows, also, the size distribution histogram of (b) $GdV_{0.5}P_{0.5}O_4$: Sm^{3+}, Tm^{3+} (d) $LaV_{0.5}P_{0.5}O_4$: Sm^{3+}, Tm^{3+} (f) $YV_{0.5}P_{0.5}O_4$: Sm^{3+}, Tm^{3+}. The IMAGE-J software was used to produce particle size distribution from 166 *(b),* 419 *(d)* and 97 *(f)* particles in each sample respectively. The average particle sizes were found to be ~ 53.8, ~ 205 and ~ 230 nm for $GdV_{0.5}P_{0.5}O_4$: Sm^{3+}, Tm^{3+} $LaV_{0.5}P_{0.5}O_4$: Sm^{3+}, Tm^{3+} and $YV_{0.5}P_{0.5}O_4$: Sm^{3+}, Tm^{3+} respectively.

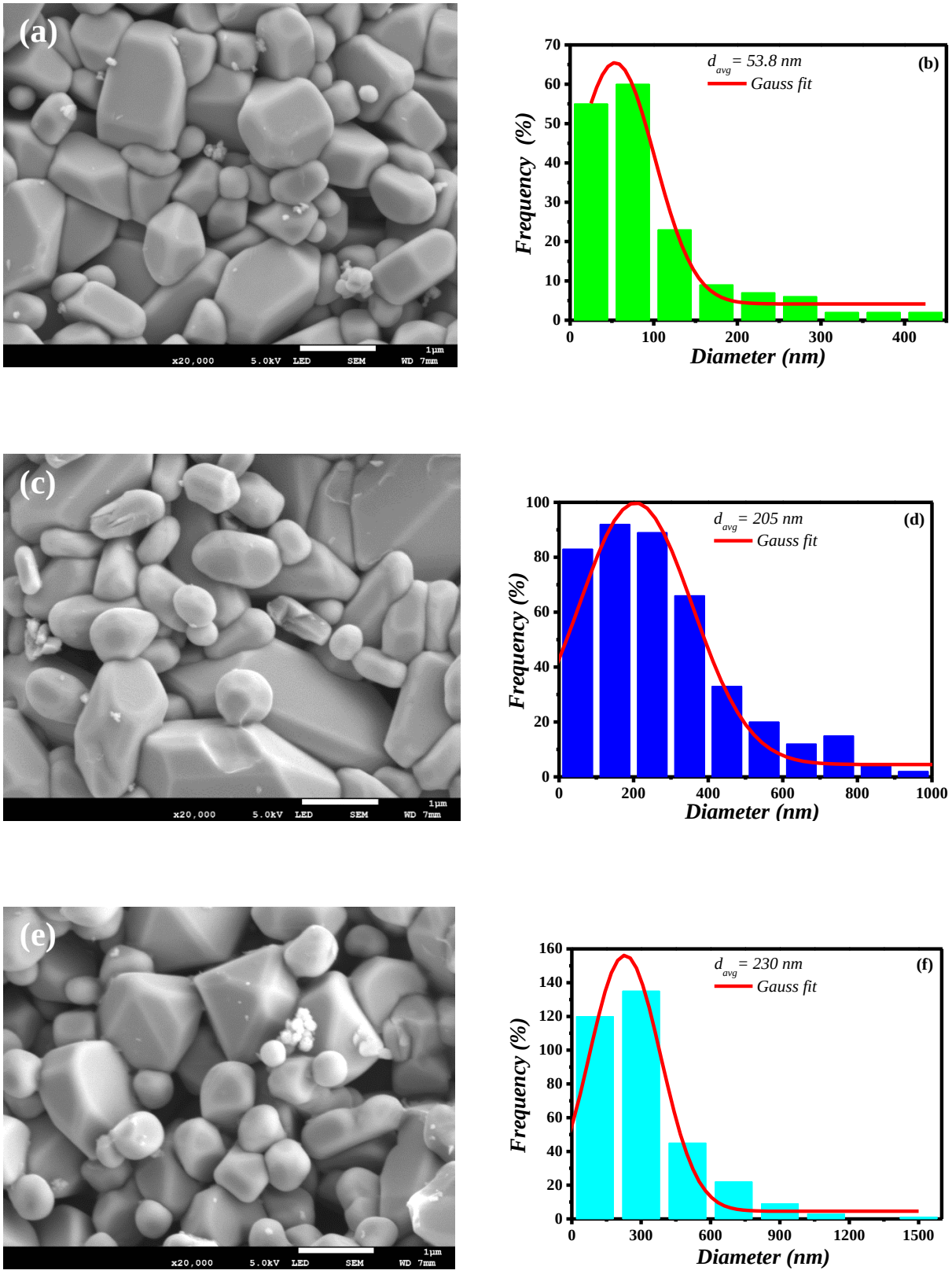

Figure 9.2. *SEM micrographs and size distribution histograms of (a and b) $GdV_{0.5}P_{0.5}O_4$: Sm^{3+}; Tm^{3+}, (c and d) $LaV_{0.5}P_{0.5}O_4$: Sm^{3+}; Tm^{3+} and (e and f) $YV_{0.5}P_{0.5}O_4$: Sm^{3+}; Tm^{3+}.*

9.3.3 UV-Vis spectroscopy

Figure 9.3 shows the room temperature reflectance spectra of $MV_{0.5}P_{0.5}O_4$: Sm^{3+}, Tm^{3+} (M=Gd, La and Y). The spectra display similar trend with a broad absorption band ranging from 200–550 nm and a small band at wavelength ~ 700 nm corresponding to $^3H_6$—$^3F_3$ Tm^{3+} transition. This broad absorption band is attributed to the O → V charge transfer transitions of $[VO_4]^{3-}$ [16]. In order to approximate the band gap energies of the prepared powder samples, transformed Kubelka-Munk reflectance was used. The band gap energies, as shown in figure 9.3 (b), were estimated to be 2.4 eV, 2.3 eV and 2.2 eV for $GdV_{0.5}P_{0.5}O_4$: Sm^{3+}, Tm^{3+}, $LaV_{0.5}P_{0.5}O_4$: Sm^{3+}, Tm^{3+} and $YV_{0.5}P_{0.5}O_4$: Sm^{3+}, Tm^{3+} respectively.

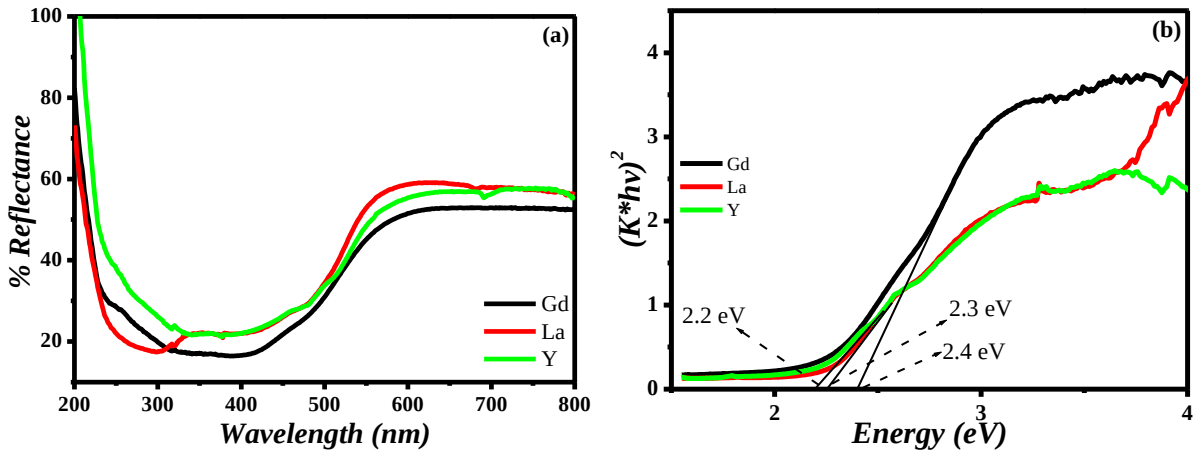

Figure 9.3. *UV-vis reflectance spectra of* ***(a)*** *and* ***(b)*** *Transformed Kubelka-Munk reflectance* $YV_{0.5}P_{0.5}O_4$: Sm^{3+}, Tm^{3+}

9.3.4 Photoluminescence spectroscopy

Figure 9.5(a) exhibits the excitation spectra of $GdV_{0.5}P_{0.5}O_4$: Sm^{3+}, Tm^{3+}, $LaV_{0.5}P_{0.5}O_4$: Sm^{3+}, Tm^{3+} and $YV_{0.5}P_{0.5}O_4$: Sm^{3+}, Tm^{3+} phosphor powders. The spectra were recorded when monitoring the emission wavelength at 602 nm. These samples show a strong broad band between 200 and 350 nm with a maximum at 270 nm. This strong band is ascribed to ligand to metal charge transfer (LMCT) from oxygen ligands to the central vanadium, phosphorus atom(s) inside $[(V,P)O_4]^{3-}$ ion(s) [17]. The emission spectra of $GdV_{0.5}P_{0.5}O_4$: Sm^{3+}, Tm^{3+},

$LaV_{0.5}P_{0.5}O_4$: Sm^{3+}, Tm^{3+} and $YV_{0.5}P_{0.5}O_4$: Sm^{3+}, Tm^{3+} obtained by monitoring the excitation wavelength at 270 nm are shown in figure 9.4(b). These emission spectra further exhibit four other emission peaks at 477, 565, 602 and 648 nm. The peak at 477 nm, which protrude from a strong broad emission band extending from 400 nm to 550 nm, is attributed to $^1G_4 \rightarrow {}^3H_6$ transition of Tm^{3+} while the strong broad band originates from the host. The other three emission peaks are ascribed to $^6G_{5/2} \rightarrow {}^6H_{5/2}$ (565 nm), $^6G_{5/2} \rightarrow {}^6H_{7/2}$ (602 nm) and $^6G_{5/2} \rightarrow {}^6H_{9/2}$ (648 nm) transitions of Sm^{3+}. The photoluminescence excitation spectra show a broad band in the ultraviolet range, whereas the photoluminescence emission spectra show line emissions and this suggests that there is energy transfer from the hosts to the activators. For this study, the photoluminescence intensity was found to be the highest when Gd was incorporated.

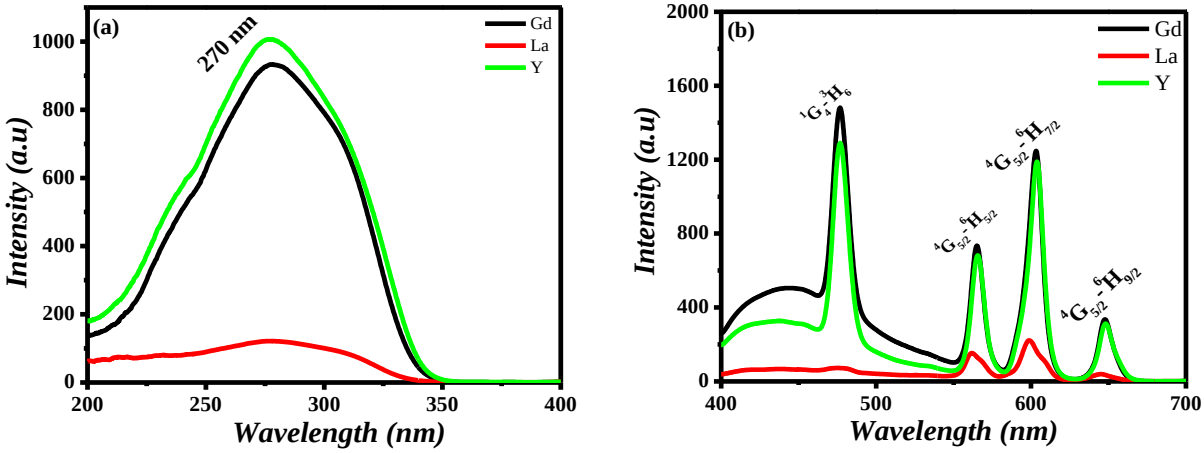

Figure 9.4. *(a) Excitation and (b) Emission spectra of $MV_{0.5}P_{0.5}O_4$: Sm^{3+}, Tm^{3+} (M = Gd, La, Y)*

9.4 Conclusion

In summary, we have successfully synthesized $GdV_{0.5}P_{0.5}O_4:Sm^{3+}$, Tm^{3+}, $LaV_{0.5}P_{0.5}O_4:Sm^{3+}$, Tm^{3+} and $YV_{0.5}P_{0.5}O_4:Sm^{3+}$, Tm^{3+} phosphor via solution combustion method using urea as a fuel. The XRD results confirmed that the prepared phosphor powders are single phase crystals. These results further confirm that Gd and Y systems have tetragonal phase while La system showed monoclinic structure. UV-Vis reflectance spectra of the three systems showed a broad absorption band towards ultraviolet region and the band gap energies were calculated using transformed reflectance Kubelka-Munk plot. The SEM images showed that the prepared phosphor powders have different morphologies and non-uniform sizes. The photoluminescence excitation and emission results indicated that these materials absorb UV radiation and re-emit in the visible region. Thus, the prepared materials have potential application as down conversion material for enhancing the dye sensitized solar cell efficiency.

9.5 References

1. D.J. Jovanovic, Z. Antic, R.M. Krsmanovic, M. Mitric, V. Dordevic, B. Bartova, M.D. Dramicanin, *Opt. Mater*. 35 (2013) 1797–1804
2. Y. Yan, J. Wang, M. Hojamberdiev, Z. Lu, B. Ren, Y. Xu, *J. Alloys Comp*. 597 (2014) 282–290
3. G. Liu, X. Duan, H. Li, H. Dong, L. Zhu, *J. Cryst. Growth* 310 (2008) 4689–4696
4. G. Jia, Y. Song, M. Yang, Y. Huang, L. Zhang, H. You, *Opt. Mater*. 31 (2009) 1032–1037
5. D.T. Lien, D.T.M. Huong, L. Van Vu, N.N. Long, *J. lumen*, 161 (2015) 389–394
6. Y. Yang, *Mater. Sci. Eng*. B178 (2013) 807– 810
7. D. Wang, Q. Shun, Y. Wang, Z. Zhang, *Mater. Chem. Phys.*147 (2014) 831-835
8. V. Kumar, S. Singh, R.K. Kotnala, S. Chawla, *J. Lumin*, 146 (2014) 486–491
9. Y. Cao, Y. Liu, H. Feng, Y. Yang, *Ceram. Int.* 40(2014)15319–15323
10. S.J. Motloung, S.K.K. Shaat, K.G. Tshabalala, O.M. Ntwaeaborwa, *J. Biol. Chem. Lumen.* 31 (2016) 1069–1076
11. F. Angiuli, F. Mezzadri, E. Cavalli, *J. Solid State Chem.* 184 (2011) 1843–1849
12. Y. Jin, C. Li, Z. Xu, Z. Cheng, W. Wang, G. Li, J. Lin, *Mater. Chem. Phys.* 129 (2011) 418– 423
13. B. Yan, X.Q Su, *J. Alloys Compd.* 431 (2007) 342–347
14. H. Lai, Y. Wang, G. Du, W. Li, W. Han, *Ceram. Int.* 40 (2014) 6103-6108
15. RJ Khalid, A. Munir, A Salamat, ZB Muhammad, N Muhammad, RB Alvina, N Muhammad, S Abubakar, *Medicine*, 94 (2015) 1−6
16. Y. Liu, H. Xiong, N. Zhang, Z. Leng, R. Li, S. Gan, *J. Alloys Compd.* 653 (2015) 126-134
17. L. Wang, L Chen, *Mater. Charact.* 69 (2012) 108-114

Chapter 10 Summary, conclusion and future work

10.1 Summary

The crystal structure, surface morphology and photoluminescent properties of rare earth (Dy^{3+}, Sm^{3+}, Tb^{3+}, Tm^{3+}) activated lanthanide phosphovanadate, $MV_{0.5}P_{0.5}O_4$ (M = Gd, La, Y), phosphor powders were investigated. These phosphors were prepared by solution combustion method. The preparation temperature was maintained at 600 ± 10^oC and urea was used as a fuel throughout the study.

The XRD results revealed that $MV_{0.5}P_{0.5}O_4$: RE is a single-phase crystal with $GdV_{0.5}P_{0.5}O_4$: RE and $YV_{0.5}P_{0.5}O_4$: RE crystallizing in a tetragonal structure and $LaV_{0.5}P_{0.5}O_4$: RE crystallizes in a monoclinic structure. These results further indicate that the prepared phosphors are well crystalline. The crystallinity was further confirmed by HRTEM. The crystallite sizes of $MV_{0.5}P_{0.5}O_4$: RE phosphors were estimated from the Williamson–Hall equation, and they are ranging between 10 and 90 nm.

The surface morphology as observed from FESEM images of $MV_{0.5}P_{0.5}O_4$: RE phosphors show that the phosphor powder is less agglomerated and it is consisted of particles that are not evenly dispersed with mixed shapes including three dimensional structures of different lengths and sizes. The incorporation of rare earth ions did not cause any noticeable change on the morphology of the prepared phosphor. The presence of these ions and the main elements forming $MV_{0.5}P_{0.5}O_4$ compound were confirmed by EDS.

The UV-Vis results of $MV_{0.5}P_{0.5}O_4$: RE phosphors showed a broad absorption band towards ultraviolet region with a maximum absorption at ~270nm wavelength. This strong band is attributed to charge transfer from oxygen ligands to the central vanadium atom(s) inside

$(VO_4)^{3-}$ ion(s). The estimated band gap energies derived from the transformed Kubelka–Munk reflectance were ranging between 3 and 5 eV.

The photoluminescence results of $MV_{0.5}P_{0.5}O_4$: RE phosphors showed a strong broad excitation band between 200 and 350 nm, although in some cases, f→f transitions beyond 350 nm were observed. The broad band was attributed to charge transfer from oxygen to vanadium within the host while f→f transitions were due to the presence of activators within the host matrix. On the other hand, the PL emission spectra displayed emission line resulting from different activators. In most cases this emission lines were protruding from a broad emission band between 400 to 650 nm wavelength, which was due to the host. The fact that the broad excitation band resulted in line emissions suggest that there was energy transfer from the host to the activators. It is therefore, clear from the UV–Vis and PL data that the wavelength range at which the strong broad band extends, suggests that the prepared phosphors may be a good candidate for the absorption of UV radiation and subsequent emission of visible photons.

In conclusion, this study demonstrated that lanthanide phosphovanadate is a single phase crystal. Depending on the type of lanthanide used, lanthanide phosphovanadate crystallizes in a monoclinic or tetragonal structure. These materials were found to be excellent for absorption of UV radiation due to orthovanadate group within the host. Rare earth dopants thus received efficient energy transfer from the orthovanadate group and displayed corresponding characteristic emissions of distinct rare earth ions.

10.2 Future Work

The $MV_{0.5}P_{0.5}O_4$ (M = Gd, La, Y): Ln^{3+} (Ln = Dy, Sm, Tb, Tm) phosphor materials presented in this thesis are mainly powders. However, down conversion (DC) phosphor materials for solar cells applications are usually applied as thin layers (*thin films*) on the outer surface of the solar cell. These DC materials are mainly used to harvest UV radiation from the sun and down convert it to visible light. Furthermore, they are used to protect the electrolyte within the dye sensitized solar cell from UV radiation. It is therefore, important to prepare these phosphors in the form of thin films and investigate their luminescent and photovoltaic properties.

The SEM results reported in this thesis indicated that the prepared nanophosphors are slightly agglomerated and they are consisted of non-uniform sizes and shapes. Although the latter is appropriate for the scattering process, but it will be also vital, to improve the synthesis method or alternatively find another synthesis method where one will be able to control the particle size and morphology.

Thus, it is suggested that:

1. $MV_{0.5}P_{0.5}O_4$ (M = Gd, La, Y) thin films are prepared by
   - pulsed laser deposition (PLD),
   - spin coating and/or
   - chemical bath deposition (CBD)

   Thermal and physical stability and luminescent properties of these thin films will be investigated.
2. To control the morphology and size, the following synthesis techniques will be used to synthesize these nanophosphors.
   - Sol-gel and chemical bath deposition

10.3 Publications

- **SJ Motloung,** KG Tshabalala and OM Ntwaeaborwa. Dual emission from Sm^{3+} and Tm^{3+} activated gadolinium phosphovanadate. *ICCBN2015 Proceedings, 617—633.*
- **SJ Motloung,** KG Tshabalala, SKK Shaat and OM Ntwaeaborwa. Structural and photoluminescent properties of green-emitting terbium doped $GdV_{1-x}P_xO4$ phosphor prepared by solution combustion method. 2016, *The Journal of Biological and Chemical Luminescence,* **31** (2016) 1069–1076
- **SJ Motloung,** KG Tshabalala and OM Ntwaeaborwa. Combustion synthesis and characterization of Sm^{3+} and Tm^{3+} co-activated yttrium orthovanadate phosphate, *Advanced Materials Letters*, **8**(6) (2017) 735-740
- **SJ Motloung,** MA Lephoto, KG Tshabalala and OM Ntwaeaborwa. Combustion synthesis and characterization of $MV_{0.5}P_{0.5}O_4$: Sm^{3+}, Tm^{3+} (M = Gd, La, Y), *Physica B*, 2017 (*accepted*)
- MA Lephoto, KG Tshabalala, **SJ Motloung**, OM Ntwaeaborwa. Tunable emission from $LiBaBO_3$:Eu^{3+}; Bi^{3+} phosphor for solid state lighting, *The Journal of Biological and Chemical Luminescence,* (DOI:10.1002/bio.3295) 2017
- MA Lephoto, KG Tshabalala, **SJ Motloung**, I Ahemen, OM Ntwaeaborwa. Study on photoluminescence and energy transfer of Eu^{3+}/Sm^{3+} single-doped and co-doped BaB_8O_{13} phosphors, *Physica B*, 2017 (*accepted*)
- SV Motloung, **SJ Motloung**, HC Swart, and TT Hlatshwayo, The effect of annealing time on the structural and optical properties of $ZnAl_2O_4$:0.01% Cr^{3+} nanophosphor prepared via the sol–gel method, *Journal of electronic materials*, (DOI: 10.1007/s11664-017-5800-6), 2017

- **SJ Motloung,** KG Tshabalala and OM Ntwaeaborwa. The effect of temperature on the structure, optical and photoluminescence properties of $LaV_{1-x}P_xO_4$: Ln^{3+} (Ln = Dy, Sm and Tb), (*In preparation*)

10.4 National Conferences

- *62nd Annual Conference of the South African Institute of Physics, University of Stellenbosch, 3 July-7 July 2017*

  Lanthanum phosphovanadate phosphors: Effect of terbium concentration

  Moloi MJ, **SJ Motloung**, MA Lephoto, KG Tshabalala, OM Ntwaeaborwa

- *62nd Annual Conference of the South African Institute of Physics, University of Stellenbosch, 3 July-7 July 2017*

  Luminescent, structural and morphological studies of a green-emitting BaB_8O_{13}:Ce^{3+} phosphors

  MA Lephoto, KG Tshabalala, SJ Motloung, OM Ntwaeaborwa

- *7th South African Conference on Photonic Materials, Amanzi, 27 March-31 March 2017*

  Study on photoluminescence and energy transfer of Eu^{3+}/Sm^{3+} single-doped and co-doped BaB_8O_{13} phosphors

  MA Lephoto, KG Tshabalala, SJ Motloung, OM Ntwaeaborwa

- *7th South African Conference on Photonic Materials, Amanzi, 27 March-31 March 2017*

  Combustion synthesis and characterization of $MV_{0.5}P_{0.5}O_4$: Sm^{3+}, Tm^{3+} (M = Gd, La, Y)

  SJ Motloung**,** MA Lephoto, **KG Tshabalala**, SKK Shaat and OM Ntwaeaborwa.

- *61st Annual Conference of the South African Institute of Physics, University of Cape Town, 4 July-8 July 2016*

  Effect of annealing temperature on the structure, morphology and optical properties of Sm3+ doped lanthanum phosphovanadate

  SJ Motloung, KG Tshabalala, SKK Shaat and OM Ntwaeaborwa

- *60th Annual Conference of the South African Institute of Physics,* ***Boadwalk Convention Center, Port Elizabeth 29 June - 3 July 2015.***

  Structural and photoluminescence properties of $LaV_{1-x}P_xO_4$:1 mol % Dy^{3+} phosphor powder prepared by solution combustion method.

  SJ Motloung, KG Tshabalala, SKK Shaat and OM Ntwaeaborwa

- *53rd Annual Conference on Microscopy Society of Southern Africa, St George's Hotel, Pretoria, 29 November – 04 December 2015.*

  Preparation of Sm^{3+} and Tm^{3+} activated yttrium phosphovanadate.

  SJ Motloung, KG Tshabalala and OM Ntwaeaborwa.

- *53rd Annual Conference of the South African Institute of Physics (SAIP), University of Limpopo, Mankweng, South Africa. 9-11 July 2008.*

  Preparation and characterization of silver nanoparticles by ascorbic acid.

  SJ Motloung, BF Dejene, HC Swart,

- *52nd Annual Conference of the South African Institute of Physics (SAIP), Johannesburg, South Africa. 3-6 July,* 2007

  Synthesis and characterization of silver nanoparticles.

  SJ Motloung, BF Dejene, HC Swart

10.5 International Conference

- *2nd International conference on Composites, Biocomposites and Nanotechnology, Durban, 28 - 30 October 2015.*

  Dual emission from Sm^{3+} and Tm^{3+} activated gadolinium phosphovanadate.

  SJ Motloung, KG Tshabalala and OM Ntwaeaborwa.

- *BIT's 5th Annual Conference of AnalytiX-2017, Fukuoka, Japan, 22–24 March 2017*

  Structure and photoluminescent properties of gadolinium phosphovanadate

  SJ Motloung, KG Tshabalala, OM Ntwaeaborwa

- *Advanced Materials World Congress 2018, Singapore* (*Abstract accepted*)

  CBD synthesis of rare earth activated lanthanide phosphovanadate

  SJ Motloung, KG Tshabalala, OM Ntwaeaborwa